ACOUSTIC NOISE AND VIBRATIONS IN SWITCHED RELUCTANCE MOTORS: ENHANCED MODELING

ACOUSTIC NOISE AND VIBRATIONS IN SWITCHED RELUCTANCE MOTORS: ENHANCED MODELING

By

Jianbin Liang, M.A.Sc., B.Sc.

A Dissertation
Submitted to the School of Graduate Studies
in Partial Fulfillment of the Requirements
for the Degree
Doctor of Philosophy

DOCTOR OF PHILOSOPHY (2019) McMaster University
(Mechanical Engineering) Hamilton, Ontario, Canada

TITLE: Acoustic Noise and Vibrations in Switched Reluctance Motors: Enhanced Modeling

AUTHOR: Jianbin Liang
M.A.Sc.
School of Automotive Engineering
(Chongqing University, China)

SUPERVISOR: Ali Emadi, Professor
Ph. D. (Texas A&M University)
IEEE Fellow
Canada Excellence Research Chair in Hybrid Powertrain Program

NUMBER OF PAGES: XXII, 197

谨以此献给我的母亲父亲

To My Parents

Abstract

Acoustic noise is an urgent issue in switched reluctance machines for noise-sensitive applications. This thesis presents a comprehensive study on the modeling, analysis, and simulation of vibration and acoustic noise in switched reluctance machines.

After presenting the fundamentals of the vibration and acoustic noise, and the conventional analytical method for the simulation of the acoustic noise in SRMs, the numerical modeling approach is presented to analyze the acoustic noise. The relationship of the acoustic noise with the circumferential orders of the vibration modes and the stator radial force density harmonics is investigated in interior-rotor (IR) SRMs, where the radial vibration of the stator back iron is known as the main source of the acoustic noise in IR SRMs.

The source of the acoustic noise in external rotor (ER) SRMs is not clear in the literature. Two numerical models are built to study the acoustic noise caused by the rotor radial vibration and the tangential vibration of the stator poles, respectively. The effect of the motor dimensions on the natural frequencies of the bending vibration modes of the back iron and the tangential vibration modes of the poles in IR and ER SRMs are also studied.

The effect of the high-axial-order vibration modes on the acoustic noise of SRMs is studied by using a novel analytical method, which can simulate the acoustic noise in the three-dimensional (3D) domain. The analytical results, which are validated by the numerical simulation and the experimental results, show that the effect of the axial orders of the vibration modes on the acoustic noise depends on the boundary conditions of the SRM.

The pattern of the radial force density harmonics in IR SRM stators and ER SRM rotors is studied and summarized in an analytical expression, which can be used to quickly calculate the temporal and circumferential orders of SRMs without running the electromagnetic FEA simulation.

Based on the analyses and the main contributions of this thesis on the vibration and acoustic noise behavior in the IR and ER SRMs, the characteristics of the vibration modes, and the harmonics of the radial force density, an enhanced numerical modeling approach is presented to quickly simulate the acoustic noise without sacrificing the accuracy.

The modeling, analyses and the simulation results presented in this thesis are experimentally validated by the hammer test results of a 60 kW three-phase 24/16 internal-rotor traction SRM, the acoustic noise test results of a three-phase 12/16 external-rotor SRM, and the hammer test and acoustic noise test results of a four-phase 8/6 internal-rotor SRM.

Acknowledgments

First of all, I would like to sincerely thank my supervisor Dr. Emadi for providing this great opportunity to be part of the team at Canada Excellence Research Chair (CERC) in Hybrid Powertrain. This Ph.D. dissertation would not have been completed without his support and trust over the past three years.

I would like to thank Dr. Berker Bilgin for his mentoring and guidance in all my publications and this dissertation. His insightful advice and encouragement have made a significantly positive impact on my research. I am grateful for the excellent example he has provided as a successful researcher and project manager.

I also would like to thank my committee members, Dr. Mehdi Narimani and Dr. Fengjun Yan for their insightful comments in my supervisory committee meetings.

Special thanks to James Weisheng Jiang. We worked closely in the acoustic noise modeling, four book chapters of the SRM text book (titled “Switched Reluctance Motor Drives: Fundamentals to Applications”), and the design of the 24/16 traction SRM in the first two years of my Ph.D study. The interesting discussions and the advice that he has provided about my research is priceless.

I would like to thank my former supervisor, Dr. Datong Qin, when I was a Master's student at Chongqing University. His wisdom and broad vision have enlightened not only my research but also my life.

Words cannot express how grateful I am to my parents for all the encouragement, sacrifices, and unwavering support. They always encourage me to pursue a higher level of studies and more success in my career.

Finally, I am grateful to all my colleagues and friends during my Ph.D. study in MARC.

This research was undertaken, in part, thanks to funding from the Canada Excellence Research Chairs (CERC) Program, and the Natural Sciences and Engineering Research Council of Canada (NSERC). I gratefully acknowledges Free Field Technologies (FFT), Powersys Solutions, CMC Microsystems, and ANSYS for their support with ACTRAN software, JMAG software, Solidworks and ANSYS Workbench used in this research, respectively.

Contents

List of Figures

List of Tables

List of Symbols

$K\ (circ)$	Lumped stiffness of the circumferential mode *circ*
k_z	Axial component of acoustic wave number
f_{mech}	Mechanical frequency
N_r	Number of rotor poles
N_s	Number of stator poles
N_{ph}	Number of phases
SPL	Sound pressure level
Π	Sound power level
L_f	Frame length
u	Temporal order
v	Circumferential order
ω_n	Angular natural frequency
ω_f	Angular forcing frequency
ζ	Damping ratio
ρ	Mass density
σ	Radiation ratio
Π_{ref}	Reference of sound power

Chapter 1: Introduction

1.1 Motivation

Switched reluctance machines (SRMs) have been considered as a potential candidate for industrial applications in recent years because of the simple structure, robust design, high-temperature tolerance, and lack of rare earth material. However, vibration and acoustic noise remain a problem for SRMs. Compared to induction machines and permanent magnet synchronous machines, acoustic noise radiated from SRMs can be more considerable. This demerit has prohibited the application of SRMs in noise-sensitive applications, such as home appliances, and electric and hybrid electric vehicles. Acoustic noise reduction is an important issue for SRMs and it is related to both motor design or motor control. However, a comprehensive analysis and study on the mechanisms of the vibration and acoustic noise behavior, the electromagnetic forces, and the vibration modes, as well as their relationships, is essential before any technique is applied to reduce the acoustic noise.

1.2 Contributions

The author contributes to several original developments, which are presented in the dissertation and briefly summarized as follows:

(1) A numerical modeling approach is presented to simulate the acoustic noise and study its relationship with the radial force density harmonics and the circumferential orders of the vibration modes.

(2) The source of the acoustic noise in external-rotor SRMs is comprehensively studied by comparing the rotor radial force density and the stator tangential force density, as well as the acoustic noise caused by the radial vibration of the rotor back iron and the tangential vibration of the stator poles.

(3) A novel analytical method, which considers the excitation of the high-axial-order vibration modes, is presented to simulate the acoustic noise in the three-dimensional (3D) domain. Results show that the effect of different axial orders of the vibration modes on the acoustic noise depends on the boundary condition of the SRM.

(4) The pattern of the stator radial force density harmonics in IR SRMs and the rotor tangential force density harmonics in ER SRMs are studied and summarized in an analytical equation. It can be used to quickly calculate the locations of the temporal and circumferential orders of the force density harmonics without running an electromagnetic FEA simulation.

(5) An enhanced numerical modeling approach is presented to quickly run the simulation of acoustic noise in SRMs without sacrificing the accuracy.

1.3 Outline of the Dissertation

The dissertation is organized as follows:

Chapter 2 presents the fundamentals of the waves and mechanical vibration in SRMs. After the discussion of the waves, the spring-mass models are presented to introduce the concepts of the natural frequency, damping ratio, forcing frequency, and resonance. The interaction between forcing harmonics at different circumferential orders and mode shapes of the vibration modes will also be investigated.

Chapter 3 presents the fundamentals of the acoustic noise in SRMs. This chapter will first investigate the calculation of natural frequencies for SRMs. Then, the features of radial force density will be discussed. The calculation of the vibration and acoustic noise by using the conventional analytical method is presented.

Chapter 4 presents the modeling, simulation, and analysis of the acoustic noise in internal-rotor SRM. A 60 kW 24/16 traction IR SRM is used to present the details of the numerical modeling approach. The presented approach includes the simulation of electromagnetic forces in JMAG, the calculation of natural frequencies, and the simulation of vibration and acoustic noise in ACTRAN. Considerations in the modeling of geometries, meshing, and contacts of the SRM are discussed to ensure the accuracy of the numerical simulation. 2D fast Fourier transform (FFT) is applied to the radial nodal force at the stator pole tip to analyze the harmonics of the radial force density. FFT is also applied to the simulated surface displacement of the housing and the sound pressure to analyze their dominant frequency components. The proposed numerical modeling approach can also be used to confirm the dominant vibration modes and the radial force density harmonic components.

Chapter 5 presents the modeling and analysis consideration of acoustic noise in external-rotor SRMs. Two numerical models are built to compare the acoustic noise caused by the radial vibration of the rotor back iron and the tangential vibration of the stator poles, respectively. The harmonic components in the rotor radial force density and the stator tangential force density are obtained and studied. Besides, how the tangential force density harmonics excite the tangential vibration modes is also investigated.

Chapter 6 presents a novel analytical method to study the excitation of the axial orders of the vibration modes and their effects on the acoustic noise in the three-dimensional domain.

In Chapter 7, the pattern of the radial force density harmonics in SRMs are presented in an analytical equation to quickly calculate the temporal and circumferential orders. For the validation, the radial force density harmonics in the stator of the 6/4, 24/16, 6/14 internal-rotor SRMs, and the rotor of the 12/16 and 18/24 external-rotor SRMs are analyzed.

In Chapter 8, an enhanced numerical modeling approach is presented, which builds up on the analyses and the modeling considerations presented in the previous chapters. The proposed method simulates the acoustic noise in SRMs quickly without sacrificing the accuracy. The methods for calculating and determining the dominant vibration modes, the dominant radial force density harmonics, the dominant frequency points to be analyzed in the acoustic noise simulation, and the required thickness and the element size in the meshing of the acoustic field, which help reduce the computation cost without sacrificing the accuracy, are presented.

Finally, the conclusions of the thesis and the potential future study are presented in Chapter 9.

Chapter 2: Fundamentals of Mechanical Vibrations in Switched Reluctance Machines

2.1 Introduction

Before acoustic noise is radiated, mechanical vibration is generated in SRMs due to the electromagnetic forces and the excitation of the vibration modes. This chapter presents the fundamentals of the mechanical vibrations in SRMs, which is the basis for the modeling, simulation, and analysis of the vibration and acoustic noise in this thesis. After presenting the fundamentals of the waves and vibrations in mechanical systems, the excitation of the vibration modes and the calculation of vibration (or displacement) in SRMs will be discussed. The relationship between the mechanical vibrations, and the temporal and spatial (or circumferential) orders of the electromagnetic force density harmonics will also be briefly introduced.

2.2 Fundamentals of Waves

In SRMs, electromagnetic force density, which changes with time and spatial position, causes vibrations and acoustic noise. Electromagnetic force density can be seen as a time- and space-varying surface wave that is applied to the SRM. It should be noted that the spatial position mentioned in this chapter and Chapter 3 only represents the circumferential position. The discussion of the axial vibration behavior and its effect on acoustic noise will be presented in Chapter 6.

2.2.1 Analytical Expression of a Surface Wave

For a time- and space- varying surface wave, time order *u* and spatial order *v* can be used in describing the expression of a surface wave:

$$\begin{aligned} d(t,\alpha) &= A\cos(\omega_u t + v\alpha + \theta) \\ &= A\cos(u\omega_{mech} t + v\alpha + \theta) \\ &= A\cos(2\pi u f_{mech} t + v\alpha + \theta) \end{aligned} \tag{2.1}$$

where *A* is the magnitude of the surface wave, ω_u is the angular frequency, *t* is the time, α is the spatial position, θ is the phase angle, ω_{mech} is the angular mechanical frequency, and f_{mech} is the mechanical frequency. An example of the 3D figure and 2D contour map of a surface wave is shown in Fig. 2-1.

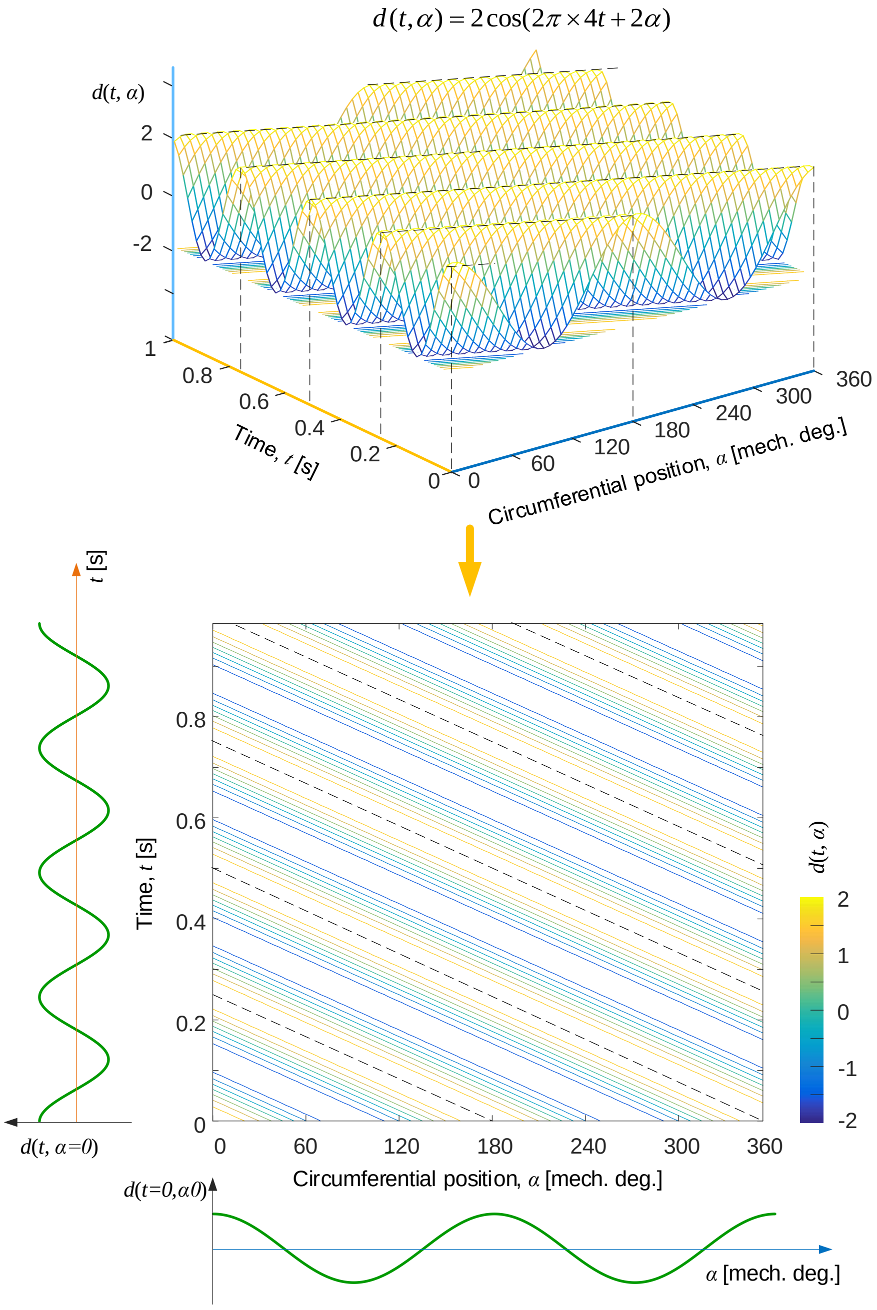

Fig. 2-1. Illustration of a surface wave, u = 4, v = 2 [1].

2.2.2 Rotational Direction of the Surface Wave

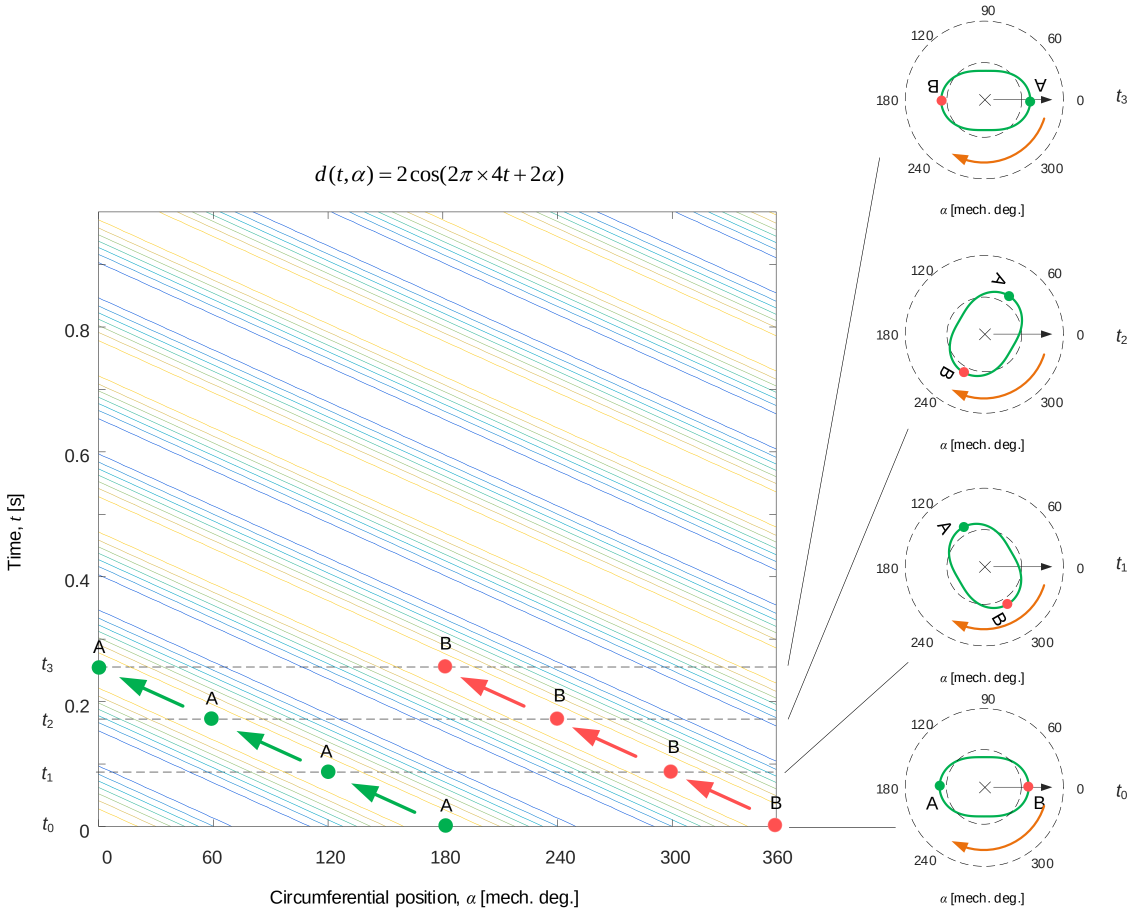

Fig. 2-2. Rotational direction for a surface wave [1].

The surface waveform of the electromagnetic force density harmonic is rotating when it is applied to the SRM. The rotational direction is related to the temporal order *u* and the spatial order *v*. The surface waveform with temporal order four and the spatial order two, which is shown in Fig. 2-2, will be used to illustrate the rotational direction of the surface wave. At each time step, the circumferential wave can be plotted in a polar coordinate system. As the time increases from t_0 to t_3, the oval shape rotates in the clockwise direction (or in the negative rotational direction). The rotational direction of the surface waveform is determined by the multiple of sgn(u) and sgn(v). If sgn(u) × sgn(v) is positive, the rotational direction is negative (CW). If sgn(u) × sgn(v) is negative, the rotational direction is positive (CCW). Fig. 2-3 shows the rotational directions for different surface waveforms with orders in the four quadrants of u-v coordinate system.

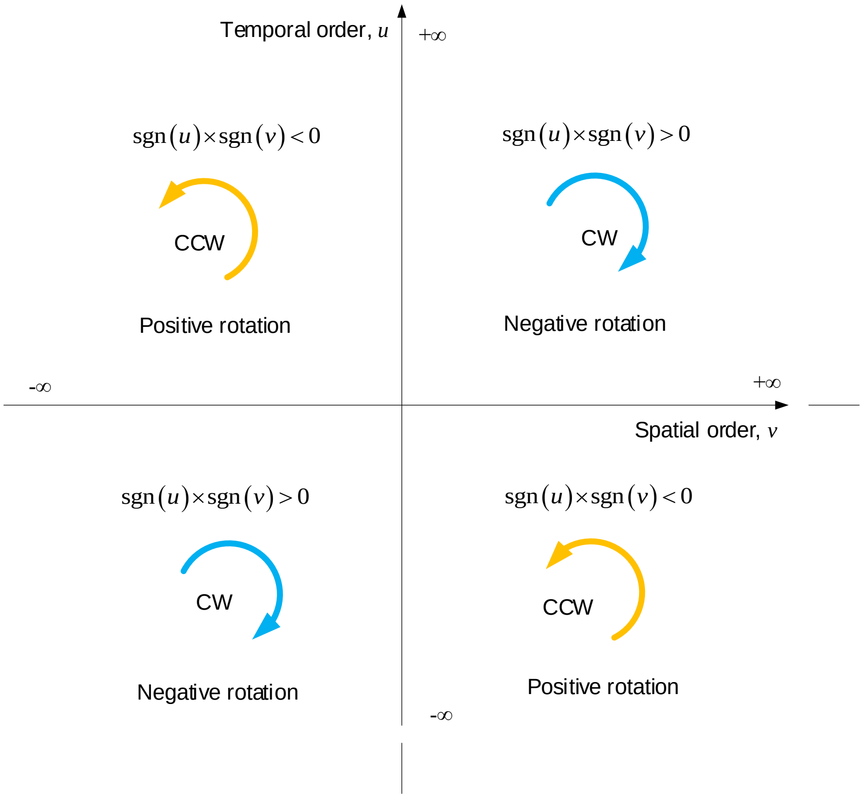

Fig. 2-3. The rotational directions of the surface waves in four quadrants [1].

2.3 Vibrations in Mechanical Systems

In the modeling of vibrations in SRMs, the motor structure can be simplified as a forced damped spring-mass system (see Fig. 2-4). The harmonic of the electromagnetic force density can be seen as a periodic force applied to the structure:

$$F(t) = F_0 \sin(\omega_f t) \tag{2.2}$$

where F_0 is the force amplitude and ω_f is the angular forcing frequency.

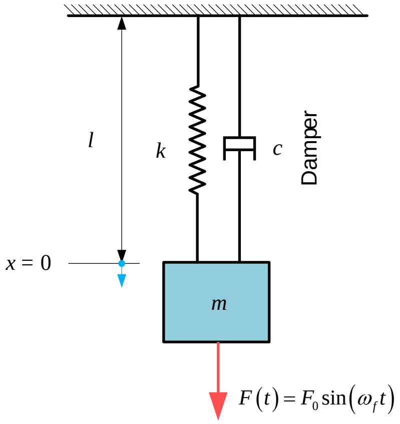

Fig. 2-4. Forced damped spring-mass system [1].

The motion of the forced damped spring-mass mechanical system can be described by:

$$\ddot{x}(t) + 2\varsigma\omega_n\dot{x}(t) + \omega_n^2 x(t) = \frac{F_0}{m} sin(\omega_f t) \tag{2.3}$$

where $x(t)$ is the displacement of the mass, ω_n is the natural frequency of the mechanical system, ω_f is the forcing frequency of the harmonic. ξ is the damping ratio. The solution of (2.3) consists of the transient response and the steady-state response:

$$x(t) = Xe^{-\varsigma\omega_n t}\sin\left(\omega_d t+\phi\right)+\frac{F_0}{k}\frac{\sin\left(\omega_f t-\phi_s\right)}{\sqrt{\left[1-\left(\frac{\omega_f}{\omega_n}\right)^2\right]^2+\left(2\varsigma\frac{\omega_f}{\omega_n}\right)^2}} \tag{2.4}$$

where ϕ_s is the phase angle at the steady response. The maximum displacement at the steady-state response can be expressed as:

$$D=\frac{F_0/m}{\sqrt{\left(\omega_n^2-\omega_f^2\right)^2+4\varsigma^2\omega_n^2\omega_f^2}} \tag{2.5}$$

Equation (2.5) will be used for the calculation of vibration in SRM.

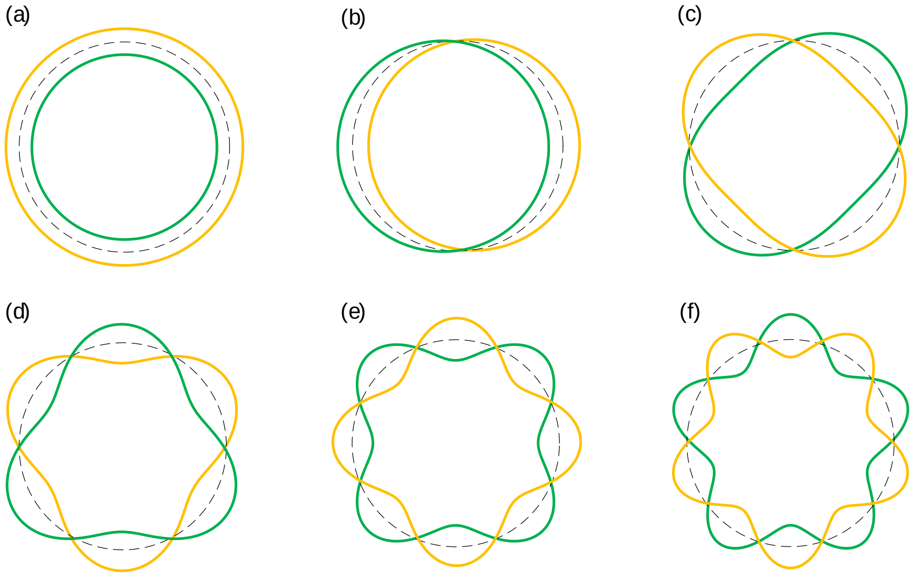

Fig. 2-5 Circumferential mode shapes for a cylindrical shell: (a) *circ* = 0, (b) *circ* = 1, (c) *circ* = 2, (d) *circ* = 3, (e) *circ* = 4, and (f) *circ* = 5 [1].

2.4 Mode Shapes

An SRM often has complicated structures of housing, stator, winding, and endcaps. Therefore, there are many vibration modes, which freely deform in the circumferential, axial, and twisting directions. However, most of the vibration modes cannot be excited due to the characteristics of the electromagnetic force density. Since the structure of an SRM can be treated as cylindrical shells, the vibration modes with different circumferential orders can be illustrated as in Fig. 2-5. For internal-rotor SRMs, these vibration modes with different circumferential orders can possibly be excited based on the pole configuration.

The free deformation in a vibration mode can appear simultaneously in the circumferential and axial directions. Axial order, *ax*, can be used to describe the axial deformation of the vibration modes. Fig. 2-6 shows examples of different vibration modes with different circumferential and axial orders. The mode shapes and their natural frequencies are simulated numerically using ACTRAN software. The cylindrical shell has an outer diameter of 300 mm, a thickness of 10 mm, and an axial length of 600 mm. The cylindrical shell is constrained on its two ends.

More comprehensive analysis of the vibration modes and their effects on the acoustic noise in SRMs (including internal-rotor and external-rotor SRMs) will be presented in Chapter 4 and Chapter 5. The effect of the axial vibration modes on the acoustic noise will also be investigated in Chapter 6.

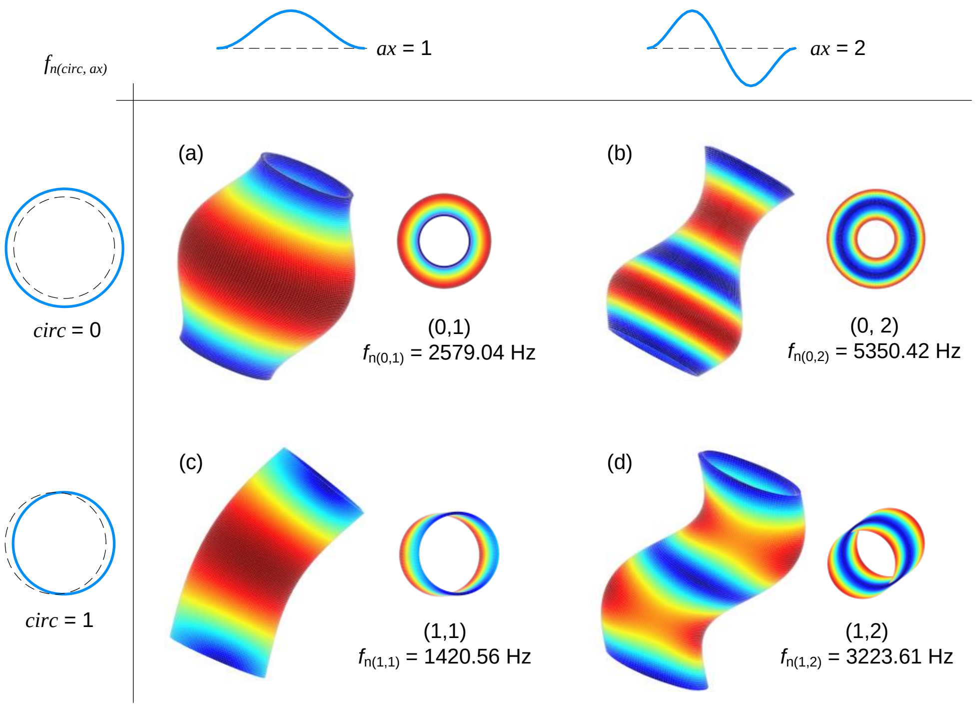

Fig. 2-6. Mode shapes of a cylindrical shell: (a) (0, 1), (b) (0, 2), (c) (1, 1), and (d) (1, 2), where the fist digit represents the circumferential order and the second digit represents the axial order [1].

2.5 Excitation of Vibration Modes

After the 2D FFT analysis of the electromagnetic force density, the temporal and circumferential orders can be obtained. In this section, the temporal and circumferential orders, as well as their relationships with the mechanical vibration will be presented.

2.5.1 Temporal Order

The temporal order is related to the frequency of a certain harmonic. The forcing frequency can be calculated as:

$$f_{f(u)} = |u| \times f_{mech} \tag{2.6}$$

where f_{mech} is the mechanical frequency. After the FFT analysis, temporal orders can be positive and negative. This is the reason why the absolute value of the temporal order is used in (2.6). The relationship between f_{mech} and the rotor speed, *rpm* is:

$$f_{mech} = \frac{rpm}{60} \ \text{[Hz]} \tag{2.7}$$

Thus the forcing frequency can be rewritten as:

$$f_{f(u)} = |u| \times f_{mech} = |u| \times \frac{rpm}{60} \tag{2.8}$$

The term q is used to represent the absolute value of temporal order. The equation of the forcing frequency can be rewritten as:

$$f_{f(q)} = q \times f_{mech} = q \times \frac{rpm}{60} \tag{2.9}$$

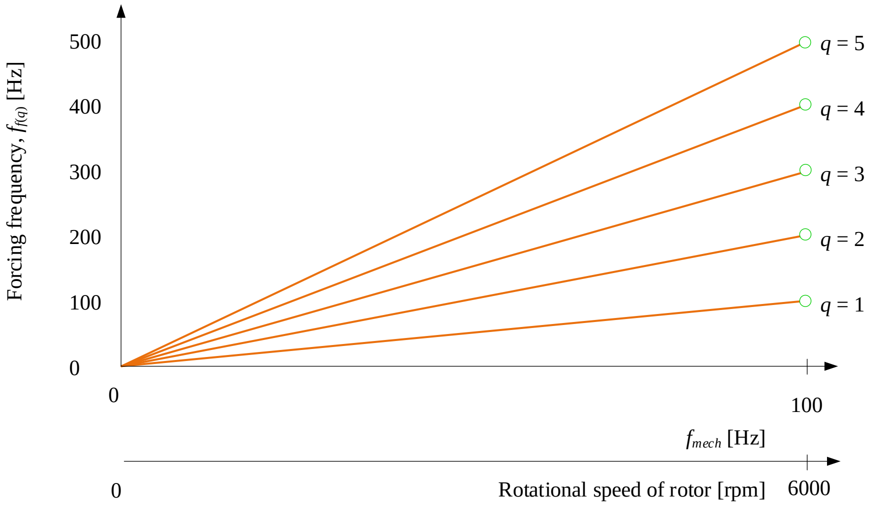

Fig. 2-7. Relationship between f_{mech}, q and forcing frequency [1].

As can be seen in (2.9) and Fig. 2-7, the forcing frequency increases linearly with motor speed and *q*.

2.5.2 Circumferential Order

The circumferential order, *v* is related to the shape of the harmonic, as shown in Fig. 2-8. When $v = 0$, the shape is a concentric circle with regard to the reference circle. When $v = \pm 1$, the shape is an eccentric circle with regards to the reference circle. When $v = \pm 2$, it has an oval shape. When $v = \pm 3$, it has a triangular shape. It can be seen that as the absolute value of *v* increases, the number of the bulges in the shapes increases [1].

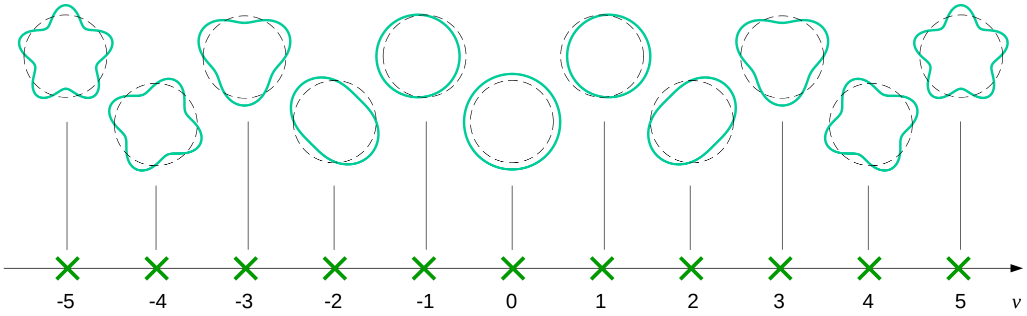

Fig. 2-8. Relationship between circumferential order v and the shape [1].

As discussed in Section 2.2.2, sgn(*u*) × sgn(*v*) determines the rotational direction of the harmonic. The positive or negative sign of *u* or *v* does not solely determine the rotational direction of the harmonic. Therefore, *circ* is used to represent the absolute value of *v*, which determines the shape of the order.

2.5.3 Harmonics in Four Quadrants

Fig. 2-9 shows the shapes for the forcing harmonic components with different temporal and circumferential orders in all four quadrants of the *u*-*v* coordinate system. The shapes in the first and the third quadrants rotate clockwise, or in the negative rotational direction. The shapes in the second and the fourth quadrants rotate counter-clockwise, or in the positive rotational direction. When *v*=0, the circumferential orders sit on the *u* axis and the forcing harmonic components all have an oval shape. When the temporal and circumferential order of the forcing harmonic component is at the origin (*u* = 0, and *v* = 0), the harmonic is the DC component. For SRMs, the DC component serves as circumferentially-uniform radial force density acting on the air gap, and this force density does not rotate or change in time. For different forcing waves, when the absolute value of the spatial or circumferential order of the forcing harmonic component, *v* is the same as the circumferential order of a certain mode, *circ*, they have the same shape. When the absolute value of *u*, or *q*, of the forcing harmonics are the same, these harmonics have the same forcing frequency.

It can be seen in Fig. 2-9 that, the forcing harmonics in the first quadrant is identical to the ones in the third quadrant, when the absolute values of their corresponding temporal order and spatial order are the same. For example, the harmonic (*u*=2, *v*=4) in the first quadrant has the same shape as (*u*=-2, *v*=-4) in the third quadrant. They also have the same rotational directions. Similarly, the forcing harmonics in the second quadrant are identical to the ones in the fourth quadrant when the absolute values of their corresponding temporal order and spatial order are the same.

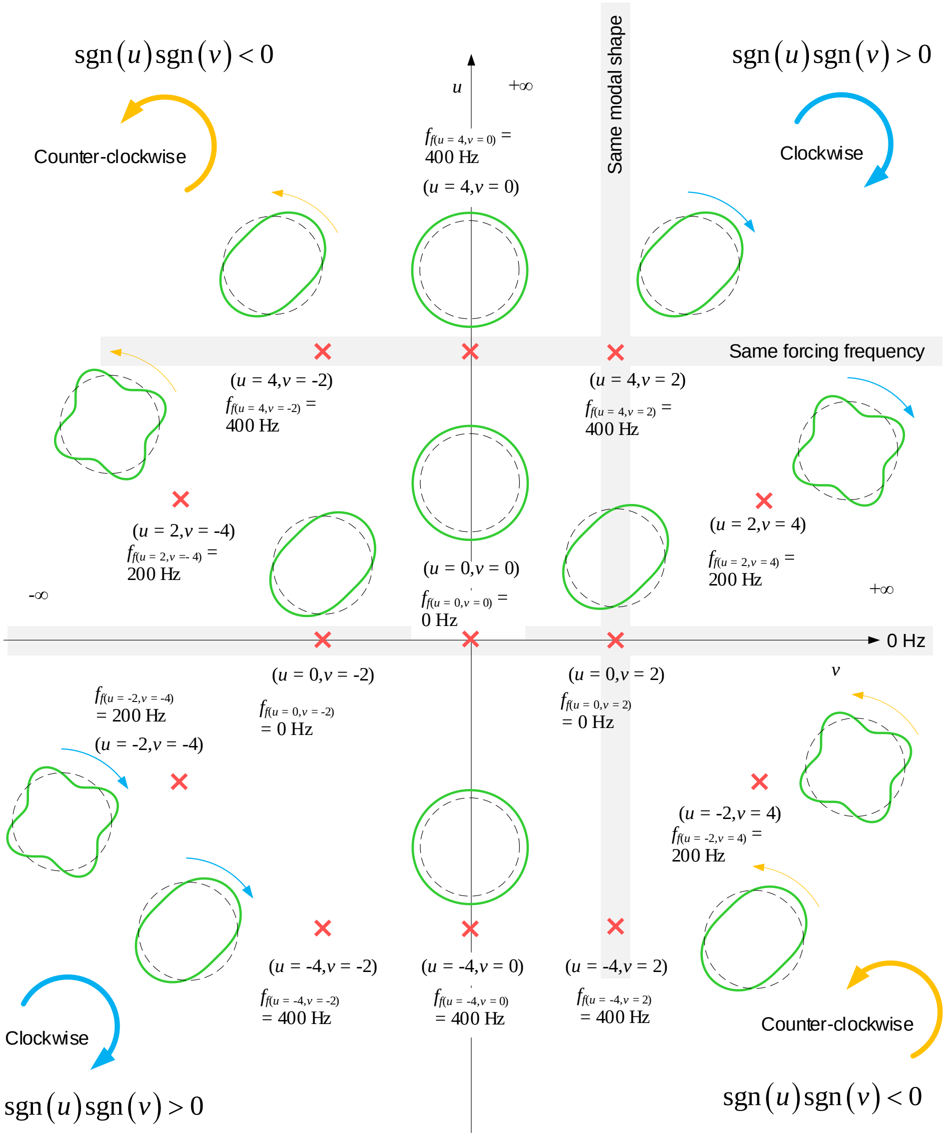

Fig. 2-9. Surface waves for selected orders in four quadrants of the *u*-*v* coordinate system [1].

2.5.4 Calculation of Displacement

The vibration in an SRM appears in both the circumferential and axial directions. Therefore, circumferential order, *circ*, and axial order, *ax*, are both used when expressing all the inputs for the calculation of the displacement. Before that, the angular frequencies for the natural frequency and forcing frequency can be found as:

$$\begin{cases} \omega_{n(q,circ,ax=1)} = 2\pi f_{n(q,circ,ax=1)} = 2\pi f_{n(circ,ax=1)} \\ \omega_{f(q,circ,ax=1)} = 2\pi f_{f(q,circ,ax=1)} = 2\pi q f_{mech} \end{cases} \tag{2.10}$$

As can be seen from (2.10), q is removed from $f_{n(q,circ,ax)}$, yielding $f_{n(circ,ax)}$. This is because for a cylindrical shell, its natural frequencies are solely determined by its *circ* and *ax*. Again, adding another index, *q*, to the analytical expression is to facilitate the matrix calculation.

When the circumferential order, *circ*, and the axial order, *ax*, of a certain forcing harmonics are the same as the circumferential order, *circ*, and the axial order, *ax*, of a vibration mode shape, displacement is generated. The displacement $D_{(q,\,circ,\,ax)}$ caused by the harmonic (*circ*, *ax*) can be calculated as [1]:

$$D_{(q,circ)} = \frac{F_{r(q,circ,ax)} / M}{\sqrt{(\omega^2_{n(q,circ,ax)} - \omega^2_{f(q,circ,ax)})^2 + 4\zeta^2_{(q,circ,ax)}\omega^2_{f(q,circ,ax)}\omega^2_{n(q,circ,ax)}}} \tag{2.11}$$

where M is the mass, $\zeta_{(q,circ,ax)}$ is the modal damping ratio of the mode (*circ*, *ax*). The calculation of the modal damping ratio for SRMs will be discussed in Chapter 3. $F_{r(q,\,circ,\,ax)}$ is the magnitude of the radial force density harmonic with temporal order, *q*, circumferential order, *circ*, and axial order, *ax*. It should be noted that only the first axial order is considered in the conventional analytical method for the calculation of the vibration and acoustic noise. An enhanced modeling approach for the analytical calculation of the acoustic noise in the three-dimensional domain, which considers the excitation of the high-axial-order vibration modes, will be presented in Chapter 6.

2.6 Conclusions

This chapter briefly presents the mechanical vibrations in SRMs. Since a harmonic of the electromagnetic force density can be seen as a surface wave applied to the motor structure, the fundamentals of the surface waves were presented. After the discussion of the vibration in a mechanical system, the mode shapes in SRMs and their excitations are briefly introduced. The fundamentals of the mechanical vibrations in SRMs presented in this chapter will be the basis for the modeling and analysis of acoustic noise in this thesis.

References

[1] J. Jiang and J. Liang, “Chapter 12: Fundamentals of waves and vibrations”, *Switched Reluctance Motor Drives: Fundamentals to Applications*, Boca Raton, FL, USA: CRC Press, ISBN: 9781138304598, Nov. 2018.

Chapter 3: Fundamentals of Acoustic Noise in Switched Reluctance Machines

3.1 Introduction

In Chapter 2, the fundamentals of the mechanical vibrations in SRMs were discussed. This chapter will first discuss the analytical method for the calculation of natural frequencies when SRM is simplified as a cylindrical shell. After presenting the damping losses in SRMs and the effect of different modal damping ratios on the acoustic noise, the calculation of the modal damping ratio is briefly discussed. The features of the radial and tangential force density are also presented. Towards the end of this chapter, the analytical method for the calculation of radiation ratio and the acoustic noise will be discussed. Chapter 2 and this chapter build the basis for the enhanced acoustic noise modeling techniques for SRMs, which will be investigated from Chapter 4 to Chapter 8.

3.2 Source of Acoustic Noise and Vibrations

As shown in Fig. 3-1, the sources of the acoustic noise radiated from an SRM can be divided into four categories: electromagnetic noise, combined electrical and mechanical noise, mechanical noise, and aerodynamic noise. Compared with the other types of electric machines, the electromagnetic noise of

SRMs can be more considerable due to the numerous harmonic components in the electromagnetic force density. Hence, the modeling and analysis of the electromagnetic noise of SRMs is the focus of this thesis. And the other sources of acoustic noise, including the mechanical noise and aerodynamic noise, are not considered in the acoustic noise modeling and analysis in this thesis.

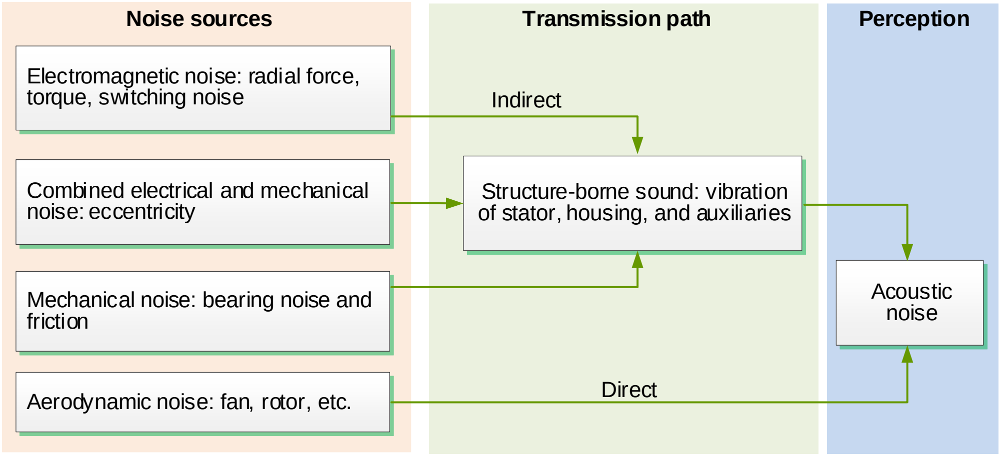

Fig. 3-1. Sources of noise and vibration for motors [1].

For an internal-rotor SRM (Fig. 3-2 (a)), the excitations of the vibration modes by the radial force density harmonics cause the deformation in the stator and the housing (see Fig. 3-2 (b)). This is the major source of acoustic noise. Resonance appears when the forcing frequency of the harmonics approaches the natural frequency of the corresponding vibration mode. Resonance can lead to a significant increase in the vibration magnitude and, thus, the acoustic noise level.

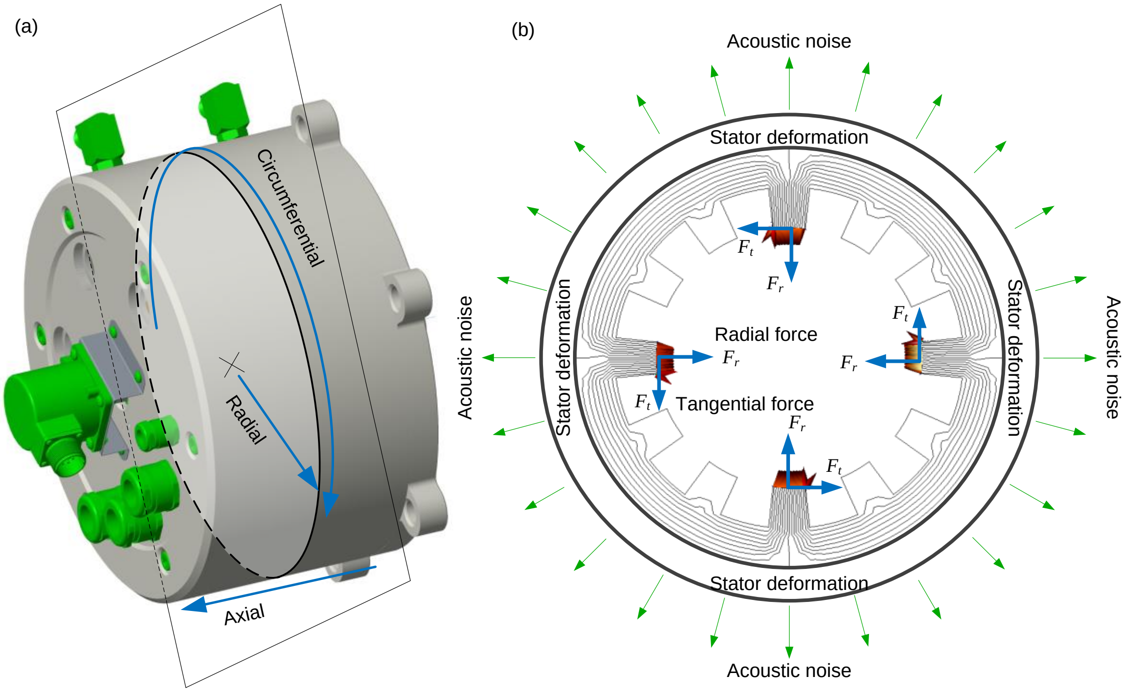

Fig. 3-2. Generation of vibration and noise in internal-rotor SRMs: (a) definition of directions, (b) radial forces and radial deformation [1].

3.3 Analytical Calculation of Natural Frequency

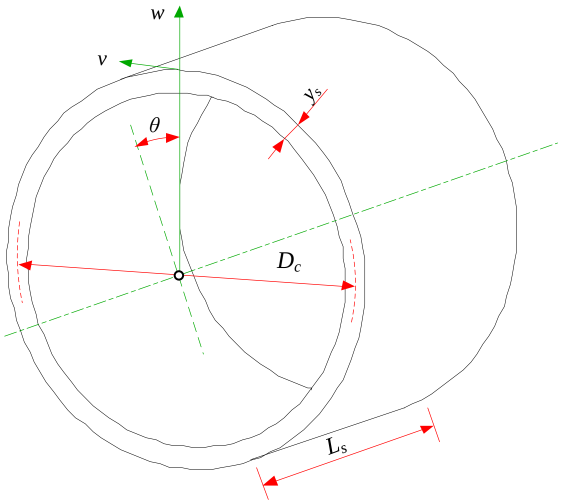

Fig. 3-3. Circular cylindrical shell and its coordinate system [1].

This section briefly introduces the analytical calculation of the natural frequencies of SRMs when the SRM stator yoke is simplified as a cylindrical shell, and the effects of the winding and stator poles are neglected. Fig. 3-3 shows an example of a circular cylindrical shell and its main dimensions. If only circumferential mode (*circ*) is considered in the calculation, the natural frequency of the stator yoke, $f_{\mathrm{n}(circ)}$, for circumferential mode *circ* is expressed as [1]:

$$f_{n(circ)} = \frac{1}{2\pi}\sqrt{\frac{K_{yoke(circ)}}{M_{yoke}}} \tag{3.1}$$

where $K_{(circ)}$ (N/m) is the lumped stiffness of the circumferential mode *circ*, M is the lumped mass of the cylindrical shell. As the main stiffness and mass source for the stator, the stator yoke makes the most contribution to the natural frequencies. Since the stator yoke is treated as a cylindrical shell, the lumped mass of the stator yoke in Fig. 3-3 can be estimated by:

$$M_{yoke} = \pi \rho_s D_c L_s y_s \tag{3.2}$$

where ρ_s is the density of the stator, D_c is the mean diameter of the stator yoke, as shown in Fig. 3-3, L_s is the axial length of the stator core, and y_s is the stator yoke thickness. If the stator yoke is regarded as an infinitely long cylindrical shell, according to the Donnel-Mushari theory [1], the lumped stiffness is solved as:

$$K_{yoke(circ)} = \frac{4\Omega_{(circ)}^2}{D_c}\frac{\pi L_s y_s E_s}{1-{v_s}^2} \tag{3.3}$$

where E_s and v_s are the elastic (or Young's) modulus and Poisson's ratio of the stator material; $\Omega_{(circ)}$ is the root of the characteristic equation of motion of the cylindrical shells:

$$\begin{cases} {\Omega_{(0)}}^2 = 1, \quad \text{for } circ = 0 \\ {\Omega_{(1)}}^2 = \frac{1}{2}\left[1 + circ^2 + \kappa \cdot circ^4\right] + \\ \qquad \frac{1}{2}\sqrt{\left[1 + circ^2 + \kappa \cdot circ^4\right]^2 - 4\kappa \cdot circ^6} \quad \text{for } circ = 1 \\ {\Omega_{(circ)}}^2 = \frac{1}{2}\left[1 + circ^2 + \kappa \cdot circ^4\right] - \\ \qquad \frac{1}{2}\sqrt{\left[1 + circ^2 + \kappa \cdot circ^4\right]^2 - 4\kappa \cdot circ^6} \quad \text{for } circ > 1 \end{cases} \tag{3.4}$$

where κ is a non-dimensional parameter and defined as

$$\kappa = \frac{y_s}{\sqrt{3}D_c} \tag{3.5}$$

The analytical method is helpful to understand how the major dimensions of the motor can affect the natural frequencies. It can also be improved by considering the effect of the stator poles and the windings. However, the analytical method for the simulation of natural frequencies is generally less accurate than the numerical method. Besides, the numerical method often requires a small computation cost. Therefore, the natural frequencies obtained from the numerical modal simulation is preferred and used in the acoustic noise modeling and analysis presented in Chapter 4 to Chapter 8. More details about the numerical modeling of natural frequencies and the comprehensive analysis of the vibration modes will be presented in Chapter 4 to Chapter 6.

3.4 Modal Damping Ratio

As discussed in Chapter 2, an SRM structure can be treated as a forced damped spring-mass mechanical system. When vibration occurs in an SRM, part of the mechanical energy is dissipated by the damping in the SRM structure. This part of mechanical energy is called as damping loss. As shown in Fig. 3-4, there are three kinds of damping losses in an SRM: structural damping loss, acoustic damping loss, and joint damping loss. The structural damping loss in SRMs is a kind of hysteresis damping while the acoustic radiation damping is a kind of radiation loss from the SRM surface to the surrounding air. The joint damping loss is generated in the joints or interfaces between different components. When different components are rigidly connected together, the joint damping loss can be neglected. Fig. 3-4 (a) shows an example of the internal-rotor SRM structure in the NVH modeling, which consists of the stator, housing, winding, and endcaps. This is because the vibration of the stator and housing is the main source of acoustic noise in internal-rotor SRMs [1]. Fig. 3-4 (b) shows the lumped damping loss model. When the electromagnetic force is applied to the stator, the stator and the housing vibrate in the radial direction. Hence, structural damping losses in the stator, windings and housing are generated.

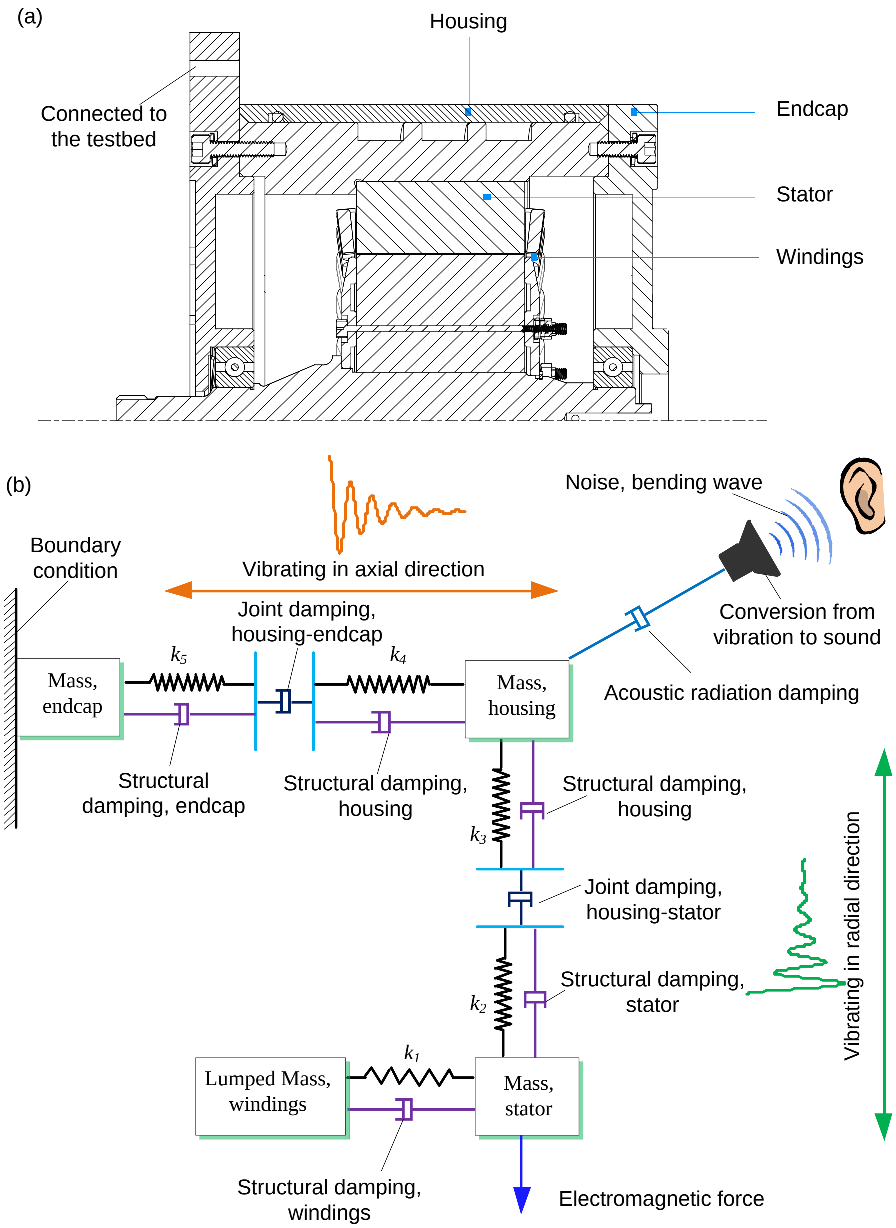

Fig. 3-4. Damping losses in an SRM: (a) cross-section view of an SRM, (b) lumped damping loss model [1].

Fig. 3-5 shows the effect of the damping ratio on the surface displacement and sound pressure of a 24/16 SRM at 2000 rpm. The simulations were conducted in ACTRAN. All the mode shapes are assumed to have the same damping ratio. Considerable differences in the surface displacement and the sound pressure can be observed in the two cases with different damping ratios.

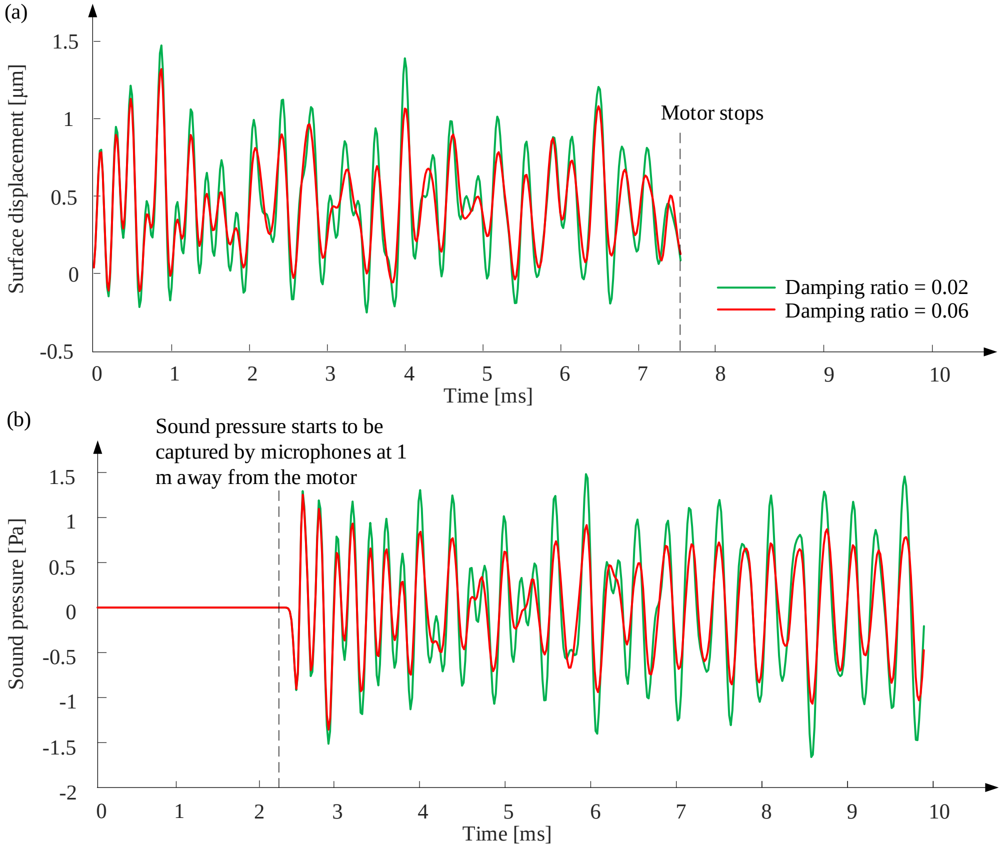

Fig. 3-5. Effect of damping ratio on a 24/16 SRM at 2000 rpm (a) surface displacement, (b) sound pressure [1].

The modal damping ratio $\xi_{\text{circ},}$ for vibration mode, *circ*, can be estimated by:

$$\zeta_{circ} = \frac{1}{2\pi}\left(2.76\times10^{-5} f_{circ} + 0.062\right) \quad (3.6)$$

where f_{circ} is the natural frequency of the circumferential order, *circ*. A more accurate estimation of the modal damping ratio can be obtained by conducting hammer tests.

3.5 Electromagnetic Forces

When the magnetic flux passes through the air gap, electromagnetic force density is generated and applied to the stator and the rotor. Based on the directions, the electromagnetic force density can be divided into two orthogonal components, including the radial force density and tangential force density. The radial and tangential force density can be calculated by using either the virtual work method or the Maxwell stress tensor method. The radial force density, $p_r(t, \gamma)$ and the tangential force density, $p_t(t, \gamma)$, at time t and in the circumferential position of α, can be calculated by using Maxwell stress tensor:

$$p_r(t,\alpha) = \frac{1}{2\mu_0}\left[B_r^2(t,\alpha) - B_t^2(t,\alpha)\right] \tag{3.7}$$

$$p_t(t,\alpha) = \frac{B_r(t,\alpha) \times B_t(t,\alpha)}{\mu_0} \tag{3.8}$$

where B_r and B_t are the radial and tangential components of the magnetic flux density, respectively. As examples, the radial force density waveform and the tangential force density waveform for a 6/4 SRM over the circumferential position and time are shown in Fig. 3-6 and Fig. 3-7, respectively. For internal-rotor SRMs, the radial vibration of the stator and the housing, which is caused by the radial force density, is the main source of acoustic noise. For external-rotor SRMs, due to the thin rotor back iron and the long stator pole height, both the radial and the tangential force density can contribute to the acoustic noise. The comprehensive analysis on how the radial force density and tangential force density cause acoustic noise in internal-rotor and external-rotor SRMs will be presented in Chapter 4 and Chapter 5. In Chapter 7, a comprehensive analysis on the pattern of the radial force density harmonics will be conducted and an analytical equation will be presented to quickly calculate the temporal and circumferential orders of the radial force harmonics in external-rotor and internal-rotor SRMs without running electromagnetic FEA simulation.

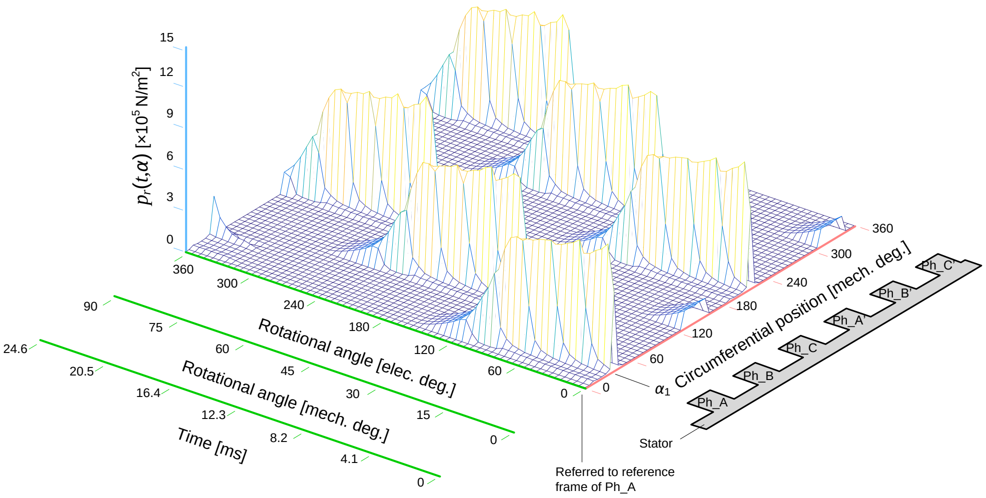

Fig. 3-6 Radial force density of a 6/4 SRM in one electrical cycle [1].

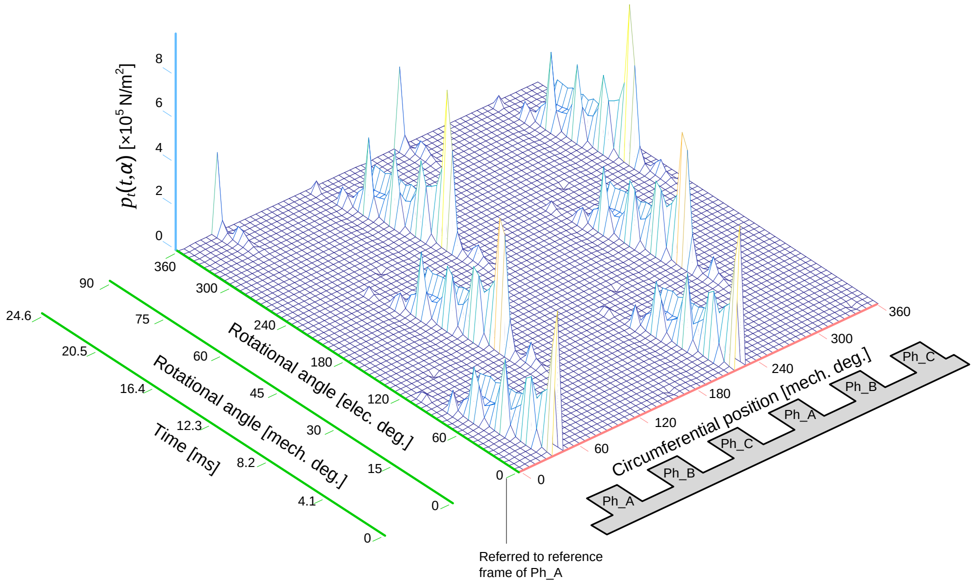

Fig. 3-7 Tangential force density of a 6/4 SRM in one electrical cycle [1].

3.6 Analytical Calculation of Acoustic Noise

When electromagnetic forces are applied on the SRM motor structure, vibration is generated, and acoustic noise is radiated. The radiation property is often characterized as the radiation ratio. The analytical calculation of the displacement has been presented in Section 2.5.4 in Chapter 2. In this section, the analytical calculation of the radiation ratio and the acoustic noise will be presented.

3.6.1 Radiation Ratio

After vibration is generated in the SRM structure, the mechanical power is converted into sound power. Radiation ratio is used to describe the relationship between the radiated sound power Π and the vibrations [1]:

$$\sigma = \frac{\Pi}{\rho_0 c_0 A_s \left\langle \overline{v^2} \right\rangle} \tag{3.9}$$

where ρ_0 and c_0 are the mass density of the air and the speed of sound in the air, respectively. A_s is the area of the sound radiation surface, and $\left\langle \overline{v^2} \right\rangle$ is the spatial averaged mean square vibration velocity on the motor surface.

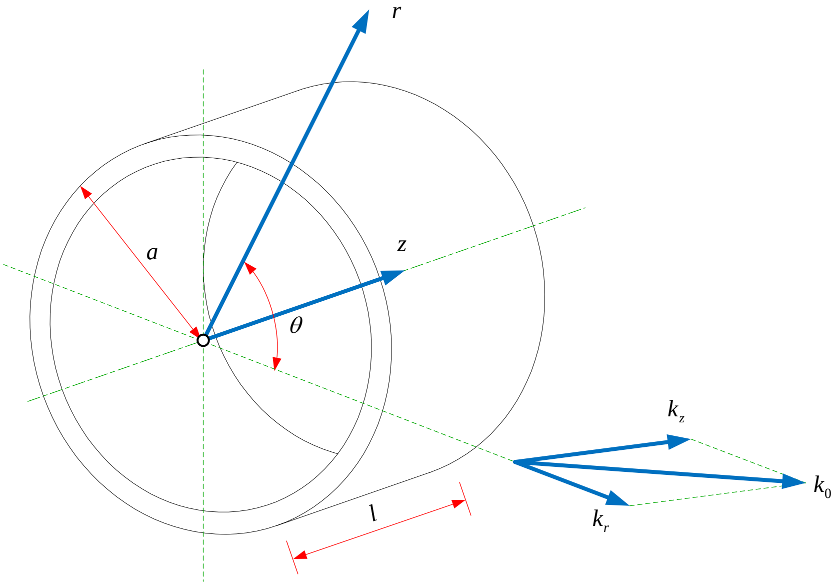

Fig. 3-8. Cylindrical shell model for radiation ratio analysis [1].

The modal sound radiation ratio depends on the shape of surfaces and the vibration frequency. For its estimation, the stator can be simplified as a cylindrical shell, as shown in Fig. 3-8. In Fig. 3-8, a and l are the radius and the length of the shell, respectively. k_0 is the acoustic waveform number, which is related to the forcing angular frequency of the vibration ω_f as given in (3.10) [1].

$$k_0 = \frac{\omega_{f(q,circ,ax)}}{c_0} = \frac{2\pi f_{f(q,circ,ax)}}{c_0} = \frac{2\pi q f_{mech}}{c_0} \tag{3.10}$$

where ω_f is the angular forcing frequency, f_f is the forcing frequency, f_{mech} is the mechanical frequency.

It can be seen from (3.10) that k_0 is proportional to the forcing frequency. k_0 is also a function of temporal order, q. k_r and k_z are the radial and axial components of the acoustic wave number respectively, and will be used in the calculation of the radiation ratio:

$$k_0 = \sqrt{k_z^2 + k_r^2} \tag{3.11}$$

Assuming that the motor has a supported-supported boundary condition at its two ends, the analytical expression for the modal radiation ratio of the finite length cylindrical shell was derived with respect to vibration frequency ω [1]:

$$\sigma_{(circ,ax)} = \int_{-k_0}^{k_0} \frac{2k_0 l}{\pi^2 a k_r^2 \left| \frac{\mathrm{d}H_{circ}{}^{(2)}(k_r a)}{\mathrm{d}(k_r a)} \right|^2} \left[\frac{ax \cdot \pi / l}{k_z + ax \cdot \pi / l} \right]^2 \frac{\sin^2[(k_z - ax \cdot \pi / l) l / 2]}{[(k_z - ax \cdot \pi / l) l / 2]^2} \mathrm{d}k_z \tag{3.12}$$

where a is the radius of the shell, l is the length of the shell, *circ* and *ax* are the circumferential mode and the axial mode, respectively. Since k_0 is a function of the temporal order, q, $\sigma_{(circ,ax)}$ also depends on q. Thus, hereafter, $\sigma_{(circ,ax,q)}$ is used to replace $\sigma_{(circ,ax)}$ to facilitate matrix computation. $H_{circ}^{(2)}(x)$, is Hankel functions of the second kind. The derivative of $H_{circ}^{(2)}(x)$ is given by:

$$\frac{\mathrm{d}H_{circ}^{(2)}(x)}{\mathrm{d}x}=\frac{H_{circ-1}^{(2)}(x)-H_{circ+1}^{(2)}(x)}{2} \tag{3.13}$$

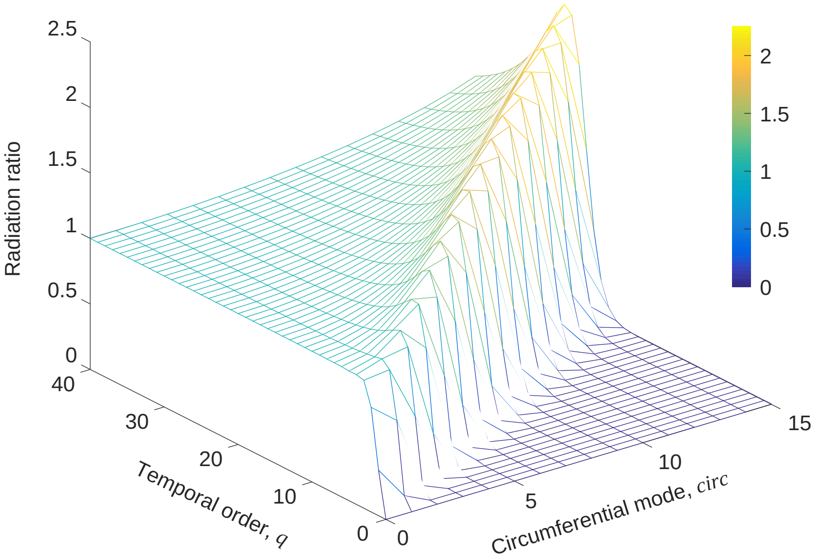

Fig. 3-9. Radiation ratio versus temporal order and circumferential mode, *ax* = 1, motor speed = 6000 rpm (f_{mech} = 100 Hz) [1].

Fig. 3-9 shows the radiation ratio versus temporal order (*q*) and circumferential mode (*circ*) when the motor speed is 6000 rpm and for the first axial mode, *ax* = 1 only. Since the motor speed is fixed, the mechanical frequency, f_{mech} is fixed. As the circumferential mode, *circ* increases, in order to reach the radiation ratio of 1, temporal order *q* should increase as well. This means that as *circ* increases, it requires higher *q* and, thus, higher forcing frequency (f_{mech} fixed) to reach the radiation ratio of 1. This trend implies that the vibration caused by a circumferential mode with higher *circ* is more difficult to be radiated from the object. A higher *circ* needs a higher *q*, thus a higher forcing frequency at a fixed motor speed, to accomplish a higher radiation ratio.

It should be noted that the calculation of the radiation ratio presented in this chapter assumes that the motor has a supported-supported boundary condition. In order to calculate the acoustic noise in the 3D domain, an improved method for the calculation of the radiation ratio, which considers different boundary conditions of the motor, will be presented in Chapter 6.

3.6.2 Acoustic Noise

Once the modal radiation ratio is calculated, the sound power for mode *circ* with forcing angular frequency ω can be calculated by using [1]:

$$\Pi_{(q,circ,ax)} = \rho_0 c_0 \left(\frac{\omega D_{(q,circ,ax)}}{\sqrt{2}} \right)^2 \sigma_{(q,circ,ax)} A_s \quad [\mathrm{W}] \tag{3.14}$$

where A_s is the area of the sound radiation surface. If axial mode is not considered, (3.14) can be expressed as:

$$\Pi_{(q,circ)} = \rho_0 c_0 \left(\frac{\omega D_{(q,circ)}}{\sqrt{2}} \right)^2 \sigma_{(q,circ)} A_s \quad [\mathrm{W}] \tag{3.15}$$

The sound power level resulting from different modes with the same forcing frequency can be superimposed together [1]. The sound power is a function of *q*, which can be calculated using:

$$\hat{\Pi}_{(q)} = \sum_{ax=1}^{ax\_\max} \sum_{circ=0}^{circ\_\max} \Pi_{(q,circ,ax)} \quad [\mathrm{W}] \tag{3.16}$$

Since the forcing frequency is related to f_{mech}, $\hat{\Pi}_{(q)}$ is a function of mechanical frequency and, hence, motor speed. When used in the units of Watts, the value of $\hat{\Pi}_{(q)}$ can vary greatly. Thus, it is more practical to use sound power level in the unit of dB. Then the sound power level is obtained by logarithmic scaling of the superimposed sound power:

$$\mathrm{SWL}_{(q)} = 10\lg\frac{\hat{\Pi}_{(q)}}{\Pi_{ref}} \quad [\mathrm{dB}] \tag{3.17}$$

where Π_{ref} is 10^{-12} W. The sound pressure is dependent on the spatial location where the sound was emitted and its average value can be calculated from the sound power result according to the NEMAMG 1-2009 standard [1]:

$$\mathrm{SPL}_{(q)} = \mathrm{SWL}_{(q)} - 10\log_{10}\left\{2\pi\left[1+\frac{\max\left(l_{shell}, 2r_{shell}\right)}{2}\right]^2\right\} \quad [\mathrm{dB}] \tag{3.18}$$

where SPL is the average sound pressure level in a free-field over a reflective plane on a hemispherical surface at 1-meter distance from the motor, plus half of the maximum linear dimension of the machine (in an electric motor, linear dimensions are l_{shell} and $2r_{shell}$, which are the axial length of the shell and the diameter of the shell, respectively) in meters. Since $f_{(q)} = qf_{mech}$, $\mathrm{SPL}_{(q)}$ is a function of frequency $f_{(q)}$:

$$\mathrm{SPL}\left(f_{(q)}\right) = \mathrm{SPL}_{(q)} \tag{3.19}$$

In this section, the analytical method for the calculation of acoustic noise is presented. Although the analytical method is generally less accurate than the numerical method, the analytical calculation process is still helpful for the enhanced NVH modeling and analysis presented in Chapter 4 to Chapter 8.

3.7 Conclusions

This chapter presents the fundamentals of the acoustic noise in SRMs. After presenting the analytical calculation of the natural frequencies in SRMs, the damping loss and the estimation of the modal damping ratio are discussed. Then, the characteristics of the electromagnetic force density, including the radial and the tangential force density, and the analytical method for the calculation of the acoustic noise in SRMs are presented.

References

[1] J. Jiang, J. Liang, J. Dong, B. Howey, and A. D. Callegaro, “Chapter 13: Noise and vibration in switched reluctance machines”, *Switched Reluctance Motor Drives: Fundamentals to Applications*, Boca Raton, FL, USA: CRC Press, ISBN: 9781138304598, Nov. 2018.

Chapter 4: Modeling and Simulation of Acoustic Noise in Internal-Rotor SRMs

4.1 Introduction

In Chapters 2 and 3, the conventional analytical method for the simulation of vibration and acoustic noise in SRMs is presented. This chapter presents a numerical modeling approach to analyze the electromagnetic forces and simulate the vibration and acoustic noise in internal-rotor (IR) SRMs.

Much effort and attempts have been made to model the vibration behavior and acoustic noise of SRMs. In the literature, two kinds of approaches in the prediction of acoustic noise for electric machines are reported: the statistical and deterministic methods. Although the statistical approach, which is based on statistical energy analysis, is applicable to complex structures in the high frequency range, this method cannot provide results with high accuracy at low-frequency range [5]. The deterministic approach includes analytical and numerical methods. The analytical method can provide a fast and computationally-efficient way for the acoustic noise prediction in both low and high frequency [2]–[7]. Therefore, it is preferred in the design, optimization and control of electric machines. On the other hand, the numerical model is more precise because more structural details can be considered in the modeling. For the numerical method, the prediction of the vibration and the acoustic noise of an electric machine is often based on three numerical models: an electromagnetic FEA model for the simulation of electromagnetic forces, a structural model for the simulation of vibration, and an acoustic model for the coupling between the aforementioned models and the acoustic simulation. The accuracy of the predicted vibration and acoustic noise depends on both the accuracy of the acoustic model and the input data. The input data includes the electromagnetic forces and the natural frequencies of SRMs [5]. A few studies in the literature present the details of a precise vibration and acoustic noise model, e.g., modeling and meshing of the structure. However, most of the numerical acoustic models in the literature are based on simplified geometries or models. The effect of winding and housing has not been considered in [8]. A precise modeling of the vibrating structure and the meshing of the structure were not reported in [8]–[11].

In this chapter, a detailed numerical modeling approach to predict the vibration and acoustic noise of a 24/16 internal-rotor SRM is presented. The modeling process is illustrated in the flow chart in Fig. 4-1. It couples electromagnetic analysis in JMAG, and modal, vibration and acoustic analysis in ACTRAN. Compared to the previous practices in the literature discussed in [8]-[12], the modeling approach in this chapter is able to take into account the effects of winding and housing. Detailed considerations and procedures to ensure the accuracy of results and to reduce the computational cost are presented in Section 4.3. This chapter also presents a useful method to quantitatively obtain and analyze the relationships between circumferential orders of the electromagnetic force density harmonics, the dominant vibration modes, the surface displacement, and the radiated acoustic noise.

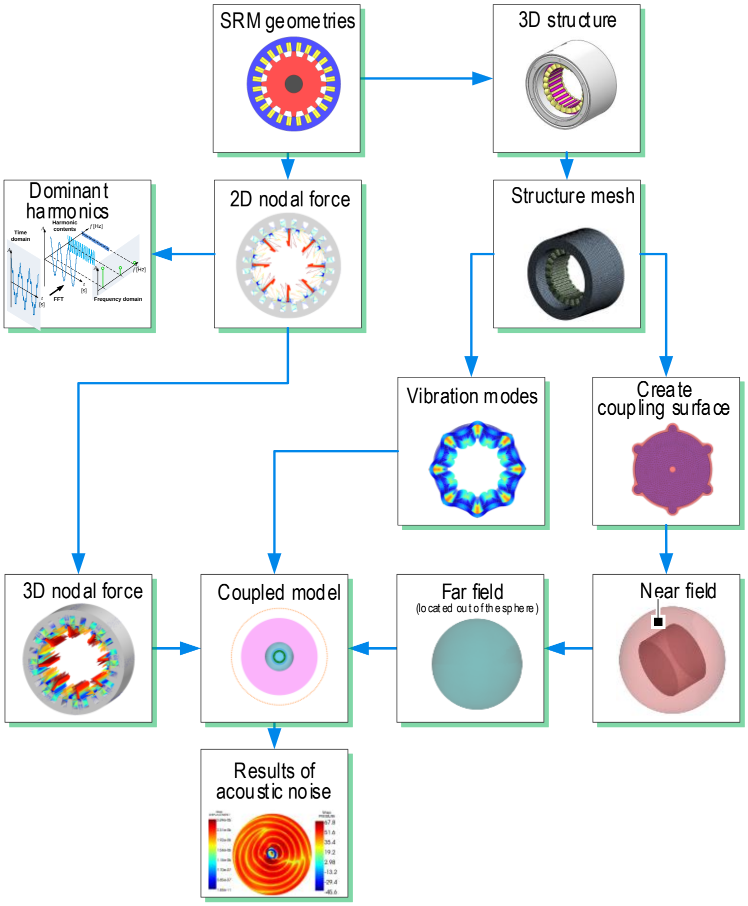

Fig. 4-1 Procedures for acoustic modeling of the 24/16 SRM.

4.2 The Design of a 24/16 SRM for Hybrid Electric Vehicle Powertrains

The vibration and acoustic analysis in this chapter is performed on a 24/16 SRM designed for traction application for a hybrid electric vehicle (HEV). Compared to internal combustion engines, which have a more broadband noise in the lower frequency range, SRMs in traction applications might radiate noise at the mid- or high-frequency range. Therefore, acoustic analysis of SRMs for traction applications is necessary [9].

Table 4-1 Comparisons of Prius 2010 traction motor and 24/16 SRM [13]

Parameter	2010 Prius	24/16 SRM
Stator outer diameter [mm]	264	264
The total axial length of active material [mm]	108	108
Air gap length [mm]	0.73	0.5
Lamination thickness [mm]	0.305	0.1
Slot fill factor	0.54	0.54
DC side voltage [V]	650	650
Maximum peak current [A]	240	240
RMS current constraint [A]	140	140
Motor peak power rating [kW]	60	60
Rotational speed rating [rpm]	13,500	13,500

The 24/16 SRM in this chapter is designed to achieve the same torque-speed envelope of the interior permanent magnet synchronous motor (IPMSM) used in the 2010 Prius powertrain [13]. Table 4-1 compares the motor specifications of the designed 24/16 SRM and the IPMSM used in the 2010 Prius powertrain. The stator outer diameter and total axial length of the active material in the 24/16 SRM are exactly the same as the IPMSM used in the 2010 Prius powertrain. Both motors can achieve similar peak power [12]. The 24/16 SRM can also achieve similar peak efficiency as that of the IPMSM used in the 2010 Prius powertrain. The peak efficiency of the 24/16 SRM is 96.5% at 7500 rpm and 60 Nm. Fig. 4-2 shows the geometries of the rotor and stator of the 24/16

SRM. The laminations are provided by Cogent Power Inc. Its grade and thickness are NO10 and 0.1 mm, respectively.

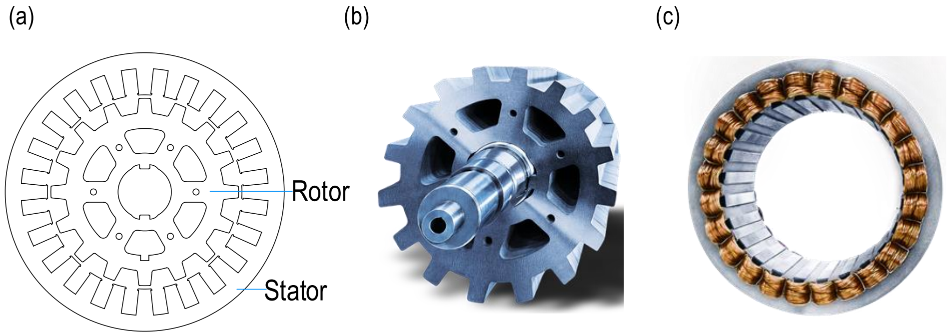

Fig. 4-2 Geometries of rotor and stator in the 24/16 SRM (a) CAD geometry, (b) rotor-shaft, and (c) stator-winding.

4.3 Numerical Acoustic Modeling of 24/16 IR SRM

4.3.1 Numerical Modeling Procedure

The procedures for the numerical modeling of vibration and the acoustic noise was shown in Fig. 4-1. The acoustic simulation needs the nodal force and the simulated vibration modes as inputs. Starting with the SRM geometries, the 2D nodal force can be generated by electromagnetic simulation in JMAG. The nodal force is a function of both time and stator circumferential positions. 2D FFT is applied to the nodal forces to analyze the dominant harmonics. Then, the 2D nodal force is extruded to 3D nodal force which is one of the inputs to the coupled noise and vibration model.

As shown in Fig. 4-1, starting with 3D motor structure, the structural meshing can be performed in ANSYS Workbench. The meshed structure is used in the simulation of vibration modes and acoustic modeling in ACTRAN. The natural frequencies and their corresponding mode shapes will be simulated in ACTRAN. The acoustic modeling is also performed in ACTRAN, including the creation and meshing of coupling surfaces, and the near field and far field. The coupling surfaces are the boundary conditions. The structural coupling surface is the boundary condition for vibration simulation and the acoustic coupling surface is the boundary condition for the acoustic noise simulation. Taking the 3D nodal force and the simulated mode shape as inputs, the coupled vibration and noise can be simulated, and the acoustic noise results are obtained.

The construction of the acoustic modeling is shown in Fig. 4-3(a). The near field is the field in which the nature of the sound wave depends on the vibration of the structure. The far field is the field in which the nature of the sound wave depends on the propagation medium, air. The near field is modeled with finite elements while the far field is modeled with infinite elements. Infinite elements are different from the finite elements. Infinite element has an exponential term in its shape function, which is better to describe the unbounded property of the far field [13]. The infinite element method is used to simulate the acoustic behavior in the far field. It is beneficial to adopt finite elements and infinite elements in the meshing for different fields. It helps to model the non-reflecting boundary conditions of the far field and provides a direct numerical estimate of the solution at all points in the far field. It has also been proven to be efficient in solving acoustic scattering problems [13-14]. The element size of the structural meshing and the acoustic meshing, as well as the connections between parts, will be discussed later. The near filed is modeled by a sphere (see Fig. 4-3(a)) in the acoustic modeling. In order to ensure the accuracy of the simulation at the expense of a low computation cost, the sphere for the near field should be at least one wavelength thick, which is measured from the surface of the SRM housing.

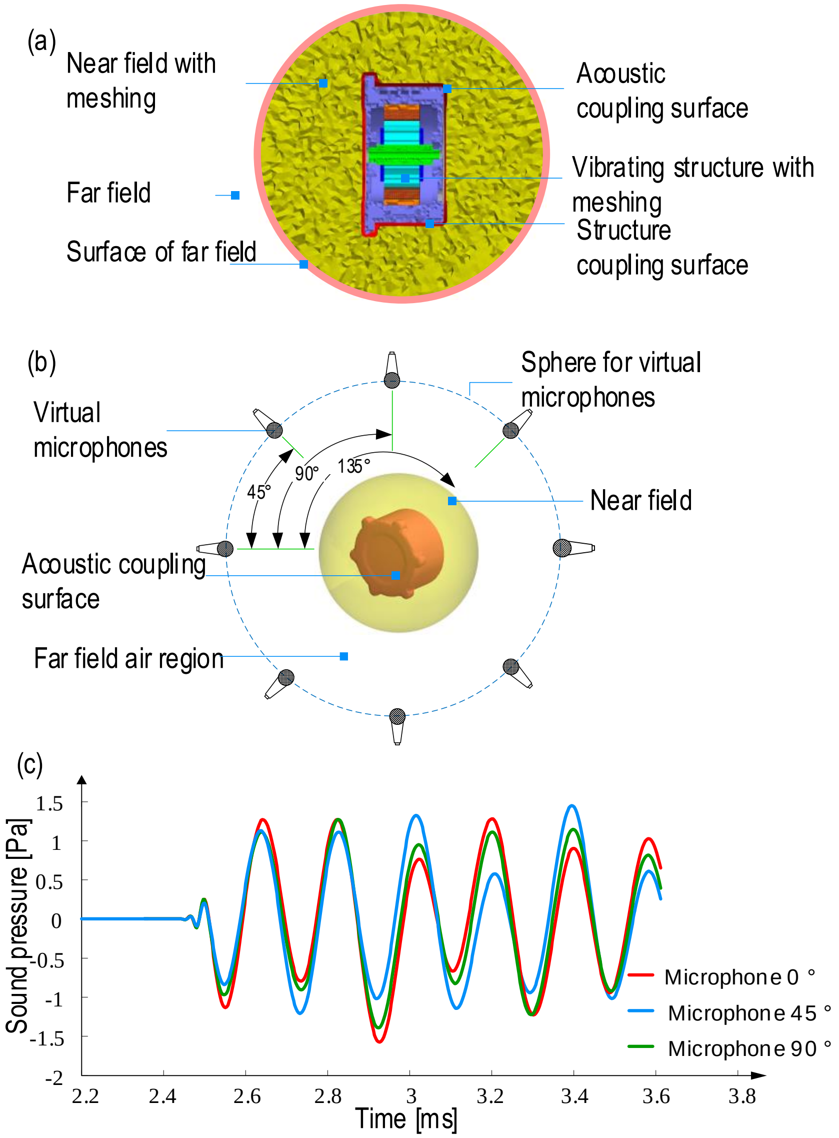

Fig. 4-3 Acoustic numerical modeling (a) acoustic model, (b) positions of virtual microphones, (c) sound pressure captured by 3 virtual microphones at different positions, motor speed 12000 rpm.

Sound pressure or sound power can be used to describe the acoustic noise level radiated from the vibrating structure. In this chapter, virtual microphones are used to measure the sound pressure of the acoustic noise radiated from the 24/16 SRM. As shown in Fig. 4-3(b), the virtual microphones are located in circles. The captured sound pressure from 3 virtual microphones are shown in Fig. 4-3(c). These 3 virtual microphones are located at 0°, 45° and 90°, respectively. Since there are differences in the amplitudes of the sound pressure captured by the 3 microphones, their positions should be selected wisely to show the characteristics of the acoustic noise in the 24/16 SRM. Virtual microphones are located in three arcs in the sphere surface, as shown in Fig. 4-4 (a). The three arcs are in three planes. Each plane has a circumferential angle of 60 degree from each other. The placement of the virtual microphones in this chapter is based on ISO 3744 standard. As shown in Fig. 4-5, a total of 20 virtual microphones are placed in a hemisphere with a radius of 1 m. Fig. 4-5 (a) and (b) are the front view and top view of the hemisphere, respectively.

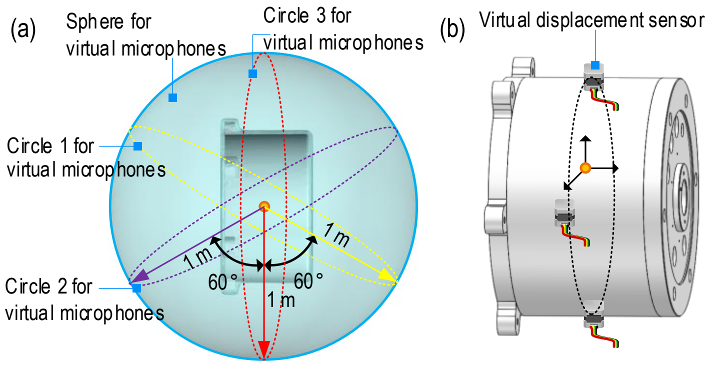

Fig. 4-4 Positions of the virtual sensors (a) virtual microphones, (b) virtual displacement sensor.

Virtual displacement sensors can also be mounted on the surface of the housing. This is beneficial for analyzing the correlation between the vibration of the structure and the radiated noise. Basically, the virtual displacement sensors should be mounted on the housing surface where maximum displacement appears. The virtual displacement sensors in this chapter are placed in the same axial position (see Fig. 4-4 (b)). The circumferential positions of the virtual displacement sensors are on the back iron aligned with the stator pole because most of the force is applied on the stator poles. Larger magnitude of vibration will be captured in this way.

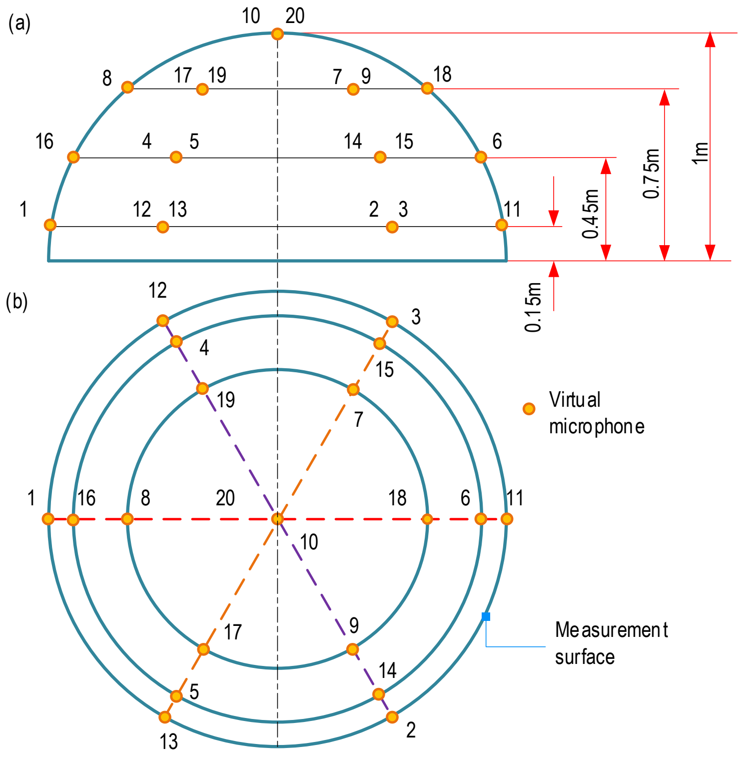

Fig. 4-5 Positions of virtual microphones for a hemispherical measurement surface based on ISO 3744 standard.

4.3.2 Calculation of Nodal Force

In order to obtain the nodal forces in the air gap, 2D electromagnetic FEA is first performed in JMAG. Fig. 4-6 (a) shows the force vectors on the SRM at a certain time step when the motor is operating at 2000 rpm. Then the 2D nodal force is extended in the axial direction to generate the 3D nodal force, as shown in Fig. 4-6 (b). The nodal forces can be divided into two parts based on their directions: radial nodal forces and tangential nodal forces. In this chapter, the radial and tangential nodal forces are both considered in the coupled simulation of vibration and acoustic noise.

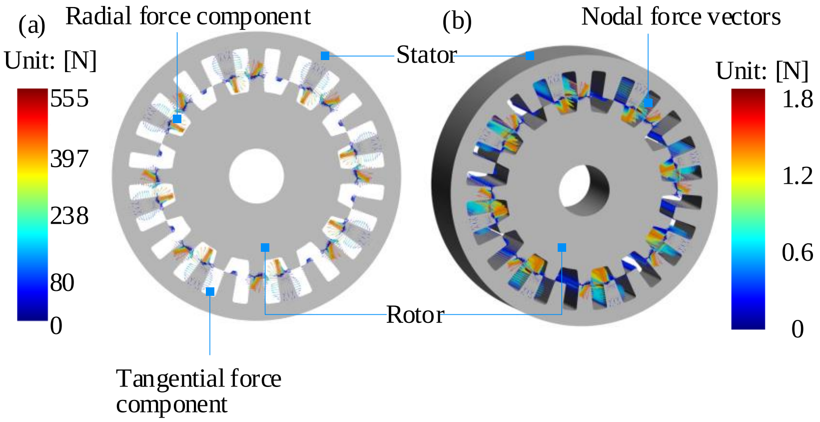

Fig. 4-6 Nodal force at 2000 rpm (a) 2D nodal force, (b) 3D nodal force

The radial nodal force at the stator pole tip is extracted as shown in Fig. 4-7. For a certain time step (e.g. at t = 0.6 s), there are eight major peaks in the circumferential position, because in a three-phase 24/16 SRM there are eight stator poles per phase. For a certain circumferential position (e.g. at the stator circumferential position of 110 mech. deg.), there is only one major pulsation on the radial force waveform with time, because in every electrical cycle each phase is excited once. Then, 2D FFT is applied on the radial nodal force in the time domain and the stator circumferential domain to analyze the dominant harmonics of the radial nodal forces. This is important and necessary to understand the dominant harmonics which lead to the highest magnitude of vibration and noise. The results and the discussion of the harmonics of the radial nodal force will be presented in Section 4.4.

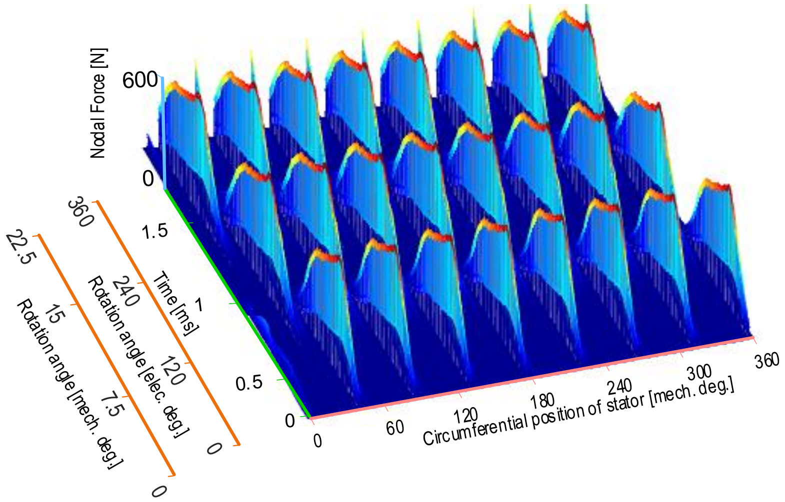

Fig. 4-7 Radial nodal force at stator pole tip of the 24/16 SRM at 2000 rpm.

4.3.3 Considerations in Modeling of the Geometry

The full assembly of the 24/16 SRM is shown in Fig. 4-8(a). It includes the endplates, end covers, shaft, stator, housing, and the rotor. For interior-rotor SRMs, literature reports that the vibration of the stator and the housing is the main source of acoustic noise [10], [11]. Therefore, the acoustic model presented in this chapter only includes the housing, stator and the windings (see Fig. 4-8(b)).

The accuracy of the predicted acoustic noise is greatly affected by the accuracy of the model. The 3D geometry of the vibrating SRM should be built up so that it is close to the actual prototyped SRM, and the natural frequency can be calculated accurately. The concentrated windings have lumped mass effect, stiffness and damping effect on the stator poles. The geometry of the coil should be modeled accurately to get the correct volume and mass of the coils, which will affect the calculation of the natural frequencies of the vibrating structure. If a coil has no connection with other coils, it will vibrate separately, as shown in Fig. 4-9 (a). This will generate many extra and unrealistic vibration modes of a single coil, which will increase the computation cost of the acoustic simulation. However, the coils of the same phase are connected together. All the coils are assumed to be integrated and thus the windings will vibrate as a whole as shown in Fig. 4-9 (b).

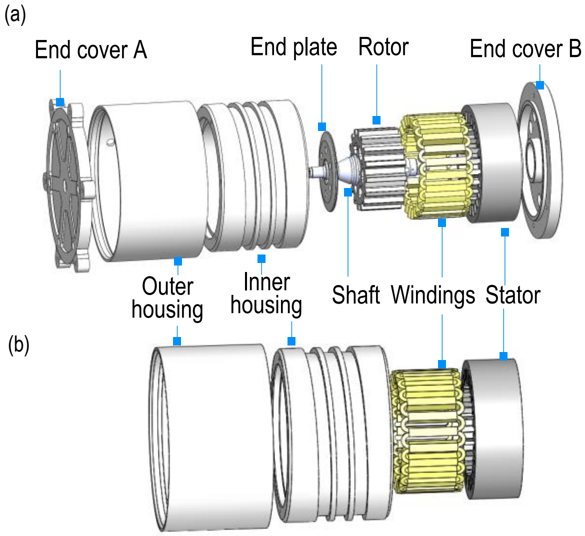

Fig. 4-8 3D geometry of the 24/16 SRM for numerical acoustic modeling (a) the complete structure, (b) housing-stator-windings structure

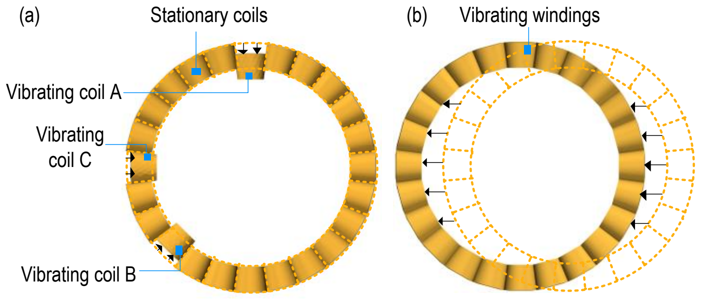

Fig. 4-9 Vibration mode of windings and a single coil (a) a single single coil, (b) the whole windings.

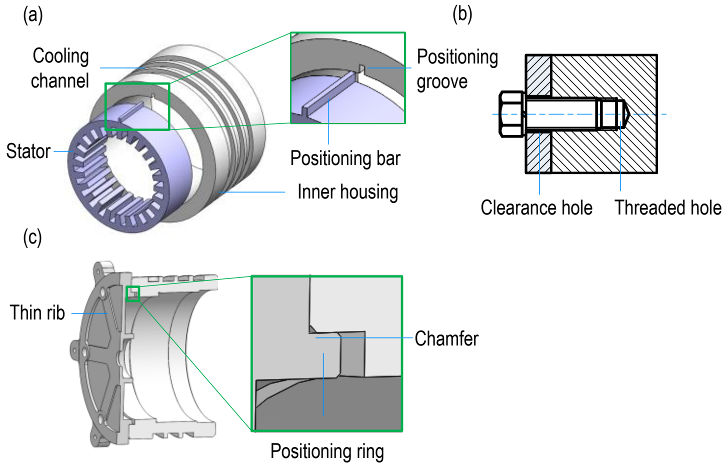

Fig. 4-10 Small features for structural simplification (a) positioning bar and groove, (b) clearance hole and threaded hole, (c) thin rib, positioning ring and chamfer.

The mass and the stiffness of the motor structure affect the accuracy of the numerical simulation. The small complicated geometrical features on the housing and the endcap need to be removed as they require finer meshing and higher computation cost. But these small complicated geometries have a relatively small effect on the simulation accuracy. The main dimensions and the masses of the housing and the endcap need to be kept the same as the original design so that the mass of the motor structure does not change after removing the small complicated features.

4.3.4 Meshing in the Numerical Modeling Approach

Proper and efficient meshing is important for numerical simulation. Considering the computation cost, the element size should not be too small. Few literatures report the calculation of element size in numerical modeling for the NVH prediction. In this section, the meshing will be discussed in detail.

Three kinds of meshing are necessary in the presented numerical model for the NVH simulation. The first one is the meshing for the electromagnetic model in JMAG to simulate the nodal force. The second kind is the structural meshing performed in ANSYS Workbench. The meshed structure will be used to calculate the natural frequencies and the simulation of the vibration. The third kind is the acoustic meshing in ACTRAN. The acoustic meshing will be generated in the near field, far field, and the coupling surfaces.

Fig. 4-11 shows the 2D simulation of nodal force in JMAG. The nodal force changes with time and circumferential position. The meshing in the electromagnetic analysis is generated in JMAG. Fine meshing is generated in the air gap, rotor pole tips, and stator pole tips, while a coarse mesh is generated in the regions that are away from the air gap.

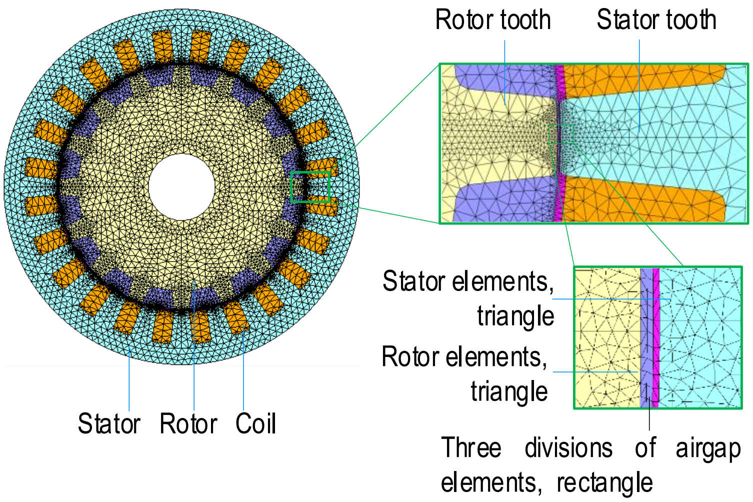

Fig. 4-11 Meshing for the simulation to generate the nodal force model.

4.3.4.1 Meshing for Electromagnetic Simulation

The mesh quality is important for the accuracy of the electromagnetic FEA simulation. The air gap has the finest meshing and rectangle elements are used. For rectangle elements in the air gap, the circumferential length and the radial length of the rectangle elements should be determined.

The radial length of the rectangle element, $E_{Airgap,\ Radial}$, can be determined by:

$$E_{Airgap,Radial} = \frac{L_{Airgap,Radial}}{N_{RadDivisions}} \tag{4.1}$$

where $L_{Airgap,\ Radial}$ is the radial length of the airgap and $N_{RadDivisions}$ is the number of radial divisions. As shown in Fig. 4-11, the number of radial divisions is 3. The radial length of the airgap, $L_{Airgap,Radial}$ is the airgap length, which is determined by the designers in the design stage of the SRM.

The circumferential length of the airgap can be calculated as follows:

$$E_{Airgap,Circ} = E_{Airgap,Radial} \times \alpha \tag{4.2}$$

where α is the aspect ratio. α should be defined by the designers based on the required meshing quality and the computation cost. Theoretically, the ideal aspect ratio is one, which makes it a square element. However, considering the computation cost, the actual aspect ratio should not be too small. If the aspect ratio is 1, the circumferential length of the element in the air gap will be the same as its radial length. Therefore, a proper value of aspect ratio should be determined based on the meshing quality and computation cost. The range of aspect ratio should be between 1 to 10.

The number of circumferential divisions, $N_{CircDivisions,}$ can be determined by:

$$N_{CircDivisions} = \frac{L_{Airgap,Circ}}{E_{Airgap,Circ}} \tag{4.3}$$

where $L_{Airgap, Circ}$ is the circumference length of the airgap.

The circumferential length of the airgap, $L_{Airgap, Circ}$, can be calculated by:

$$L_{Airgap,Circ} = 2\pi R_{Airgap,Radius} \tag{4.4}$$

where $R_{Airgap, Radius}$ is the radius of the airgap.

The element size of the rotor tip should also have fine meshing, which can be calculated by:

$$E_{Edge,Rotor} = \frac{2\pi R_{Rotor}}{N_{CircDivisions}} \tag{4.5}$$

where R_{rotor} is the radius of the rotor outer radius.

The element size of the stator tip can be calculated by

$$E_{Edge,Stator} = \frac{2\pi R_{Stator}}{N_{CircDivisions}} \tag{4.6}$$

where R_{stator} is the radius of the pole tip.

4.3.4.2 Meshing for Structural Simulation

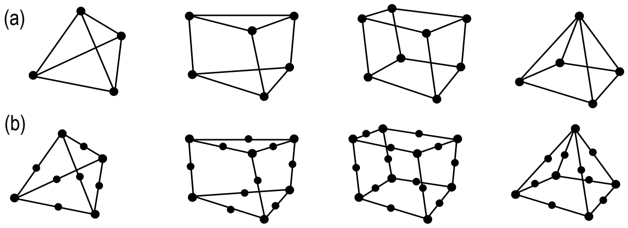

Fig. 4-12 Element types of the meshing (a) linear elements, (b) quadratic elements.

In the structural meshing (see Fig. 4-3(a)), the element size is related to the highest frequency of the noise in the simulation. The required element size of the SRM structure can be expressed as [15]:

$$\varepsilon = \frac{1}{n} \times \lambda_B \tag{4.7}$$

where λ_B is the wavelength of the bending wave and *n* is the number of elements per wavelength. The number of elements per wavelength is determined by the type of the elements in the SRM meshed structure. For linear elements, *n* can be between 8 to 10. For quadratic elements, *n* is between 4 to 6. Fig. 4-12 shows the linear elements and quadratic elements. For linear tetrahedron element, shown in Fig. 4-12 (a), it needs four interpolation nodes and the shape function is a first-order function. For quadratic tetrahedron element (see Fig. 4-12 (b)), it needs 10 nodes with a second-order shape function.

The wavelength λ_B can be calculated as:

$$\lambda_B = \frac{c_B}{f} \tag{4.8}$$

where c_B is the speed of the bending sound wave, f is the maximum frequency in the acoustic simulation. The speed of bending wave, c_B, can be calculated by:

$$c_B = (1.8 \times c_L \times t \times f)^{0.5} \tag{4.9}$$

where c_L is the longitudinal sound wave, t is the thickness of the housing. The speed of the longitudinal wave, c_L, is calculated as:

$$c_L = \left\{ \frac{E}{\rho\pi\left(1-\nu^2\right)} \right\}^{0.5} \tag{4.10}$$

where E, ρ and v are the Young's modulus, density and Poisson's ratio of the housing material, respectively.

4.3.4.2 Meshing for Acoustic Simulation

The acoustic meshing in ACTRAN includes the meshing of the far field, near field and the coupling surfaces. The element size in the acoustic meshing also depends on the highest frequency of the acoustic noise in the simulation. The element size decreases dramatically when the frequency increases. The maximum frequency simulated in this chapter is 10 kHz. The element size in the acoustic meshing can be calculated by:

$$\varepsilon = \frac{c}{n \times f} \tag{4.11}$$

where c is the speed of the sound, f is the highest frequency of the acoustic noise, n is the number of elements per wavelength. For linear elements, n should be equal to 8 to 10. For quadratic elements, n should be equal to 4 to 6. Given that enough elements per wavelength are used, the linear element mesh and quadratic element mesh should give the same results. The quadratic mesh is usually preferred because it can give more accurate results for a complex geometry or complex acoustic field.

It should be noted that the numerical method for the simulation of acoustic noise presented in this chapter is conducted in the time domain. The maximum frequency considered in the simulation of the acoustic noise of the 24/16 SRM in this chapter is 10 kHz. Therefore, the element size in the meshing of the motor structure and the near field can be calculated by using (4.7) and (4.11) with $f = 10$ kHz. In Chapter 8, an enhanced numerical modeling approach, which can reduce the computation cost significantly without sacrificing the accuracy, will be presented to conduct the acoustic noise simulation in the frequency domain.

4.3.5 Considerations for the Contacts in the Meshed Structure

Another important issue in the meshing of the structure is the connection of the nodes in the interface between parts. The connections of the nodes at the interfaces affect the stiffness of the parts and affect the natural frequency. Therefore, it is important to model the connections correctly as it will affect the structural behavior and, hence, the acoustics. The connection of the nodes can be defined by the type of the contacts between parts. In the 24/16 SRM, the assembly includes the stator core and the housings. Since the inner housing and the outer housing are welded together, the contact between them should be defined as a bonded contact. The subassembly of the stator and the windings can be seen in Fig. 4-13 (a). Although there is a thin layer of insulation between the coils and the stator poles, the contact between the coils and the stator poles is treated as a bonded contact. This is because vacuum pressure impregnation (VPI) has been applied to the stator windings. VPI is a process to seal the voids in the windings with varnish or resin by using vacuum and pressure. Therefore, the stator and the concentrated winding can also be bonded by the resin or varnish. On the other hand, the windings have more mass effect on the stator poles than stiffness effect [9]. The weak stiffness can be simulated by assigning a low value of Young's modulus to the windings, which are in bonded contact with the stator poles. In this chapter, the Young's modulus of the winding is 12 GPa [9], which is much lower than the Young's modulus of copper, 117 GPa. The material properties used in the 24/16 SRM model are listed in Table 4-2.

Table 4-2 Material properties of the 24/16 SRM

Part	Stator	Coils	Housing
Density [kg/m^3]	7268	4908	2700
Young's modulus [GPa]	176	12	68.9
Poisson's ratio	0.285	0.3	0.33

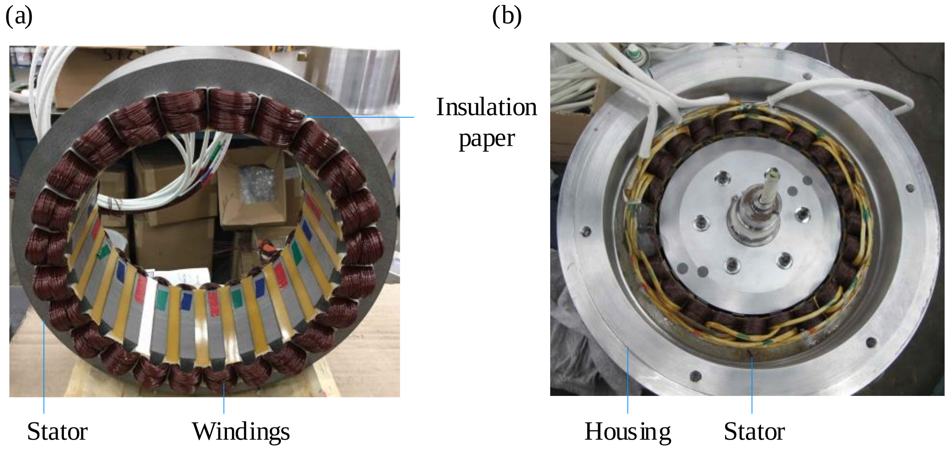

Fig. 4-13 Contacts between parts, (a) bonded contacts in stator- windings subassembly, (b) bonded contacts between stator and housing.

The connection between the stator core and the housing is treated as a bonded contact because the press fit is used between the housing and the stator core. Another reason is that two small set screws are installed in the interface between the stator core and the housing to avoid tiny relative motion between these two parts.

4.4 Acoustic Noise Analysis of 24/16 IR SRM

4.4.1 Dominant Harmonics and Vibration Mode at 2000 rpm

The harmonics of the radial force on the stator core mainly cause the vibration and the acoustic noise in SRMs [19]-[21]. Analyzing the dominant harmonics of the radial force are important for the acoustic noise analysis and noise reduction. It helps to develop a deep understanding of the dominant harmonics and the dominant vibration modes in the 24/16 SRM at a certain speed.

In this section, the nodal force at the stator pole tips (see Fig. 4-7) is extracted to perform the 2D fast Fourier transform (FFT). The 2D nodal force changes with time and stator circumferential position. The radial force is the sum of the harmonics and it can be expressed as [3]:

$$\begin{aligned}\mathcal{F}_r(\mathrm{t},\alpha) &= \sum_{v=-\infty}^{\infty}\sum_{u=-\infty}^{\infty}\left(\mathcal{F}_{r(\mathrm{u},v)}\right) \\ &= \sum_{v=-\infty}^{\infty}\sum_{u=-\infty}^{\infty}\left[F_{r(u,v)}\cos(2\pi f_{mech}ut+v\alpha+\phi_{(u,v)})\right]\end{aligned} \tag{4.12}$$

where $F_r(\alpha,t)$ is the radial force changing with time and stator circumferential position, $F_{r(u,v)}$ is the amplitude of the harmonics, f_{mech} is the mechanical frequency, u is the temporal order, v is the circumferential order, t is the time, α is the stator circumferential angle, $\Phi_{(u,v)}$ is the phase angle of the harmonic. The forcing frequency $f_{f(u,v)}$ of the harmonics can be calculated by $f_{f(u,v)} = u \times f_{mech}$. The mechanical frequency f_{mech} is calculated by $f_{mech} = n/60$, where n is the operating speed of the motor.

The amplitudes of the harmonics are shown in Fig. 4-14. The harmonics with the same absolute value of u and the same absolute value of v can be superimposed based on their phase angles. The superimposed harmonics are summarized in Table 4-3, where q is the absolute value of u, and *circ* equals to the absolute value of v. In Table 4-3, the harmonics with “+” sign means that the harmonics are rotating in the positive (counter-clockwise) direction while the harmonics with “-” sign means that the harmonics are rotating in negative (clockwise) direction. A standing wave is generated in some harmonics. A standing wave is defined as the wave in which the amplitudes of some particular points remain unchanged while other points oscillate.

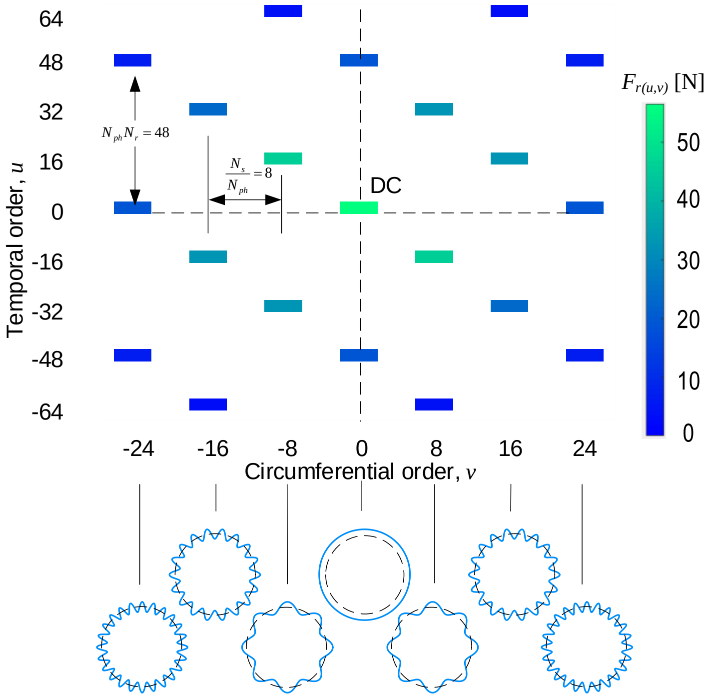

Fig. 4-14 Harmonics of radial nodal force on the stator pole tip, 2000 rpm.

Table 4-3 Amplitudes of the harmonics in a 24/16 SRM, 2000 rpm

$F_{r(circ,\,q)}$		Circumferential order, $\lvert v\rvert$ = *circ*			
Forcing frequency	Temporal order, $\lvert u\rvert = q$	0	8	16	24
4800	144	$2F_{r\,(144,\,0)}$			$-2F_{r\,(48,\,24)} + 2F_{r\,(-48,\,24)}$ Standing wave
4267 3733	128 112		$-2F_{r\,(128,\,8)}$ $+2F_{r\,(-112,\,8)}$	$+2F_{r\,(-128,\,16)}$ $-2F_{r\,(112,\,16)}$	
3200	96	$2F_{r\,(96,\,0)}$			$-2F_{r\,(48,\,24)} + 2F_{r\,(-48,\,24)}$ Standing wave
2667 2133	80 64		$-2F_{r\,(80,\,8)}$ $+2F_{r\,(-64,\,8)}$	$+2F_{r\,(-80,\,16)}$ $-2F_{r\,(64,\,16)}$	
1600	48	$2F_{r\,(48,\,0)}$			$-2F_{r\,(48,\,24)} + 2F_{r\,(-48,\,24)}$ Standing wave
1067 533	32 16		$-2F_{r\,(32,\,8)}$ $+2F_{r(-16,\,8)}$	$+2F_{r\,(-32,\,16)}$ $-2F_{r\,(16,\,16)}$	
0	0	$F_{r\,(0,\,0)}$			$2F_{r\,(24,\,0)}$

The circumferential order, v is related to the shape of the harmonics [22]-[23]. For example, the harmonic $F_{r(q=48,circ=0)}$ has a circumferential order of 0. When this harmonic is applied to the stator, the shape of the harmonic is concentric to the center of the stator. The harmonic $F_{r(q=32,circ=8)}$ has a circumferential order of 8. When this harmonic is applied to the stator, the shape of the harmonic has 8 peaks and 8 troughs in the circumferential position.

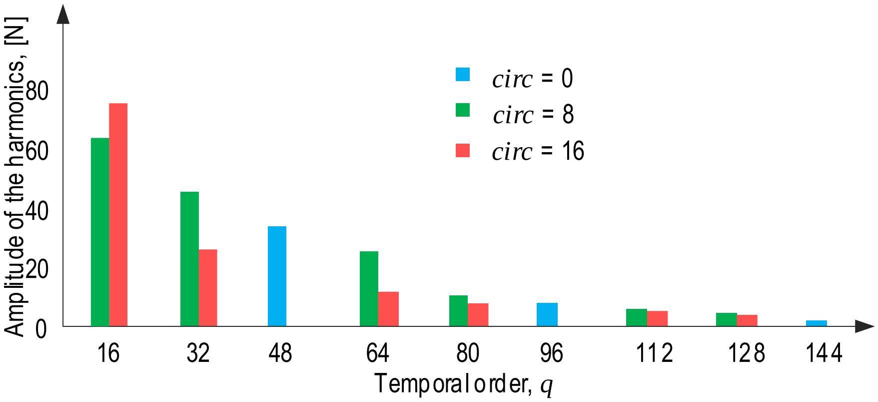

Fig. 4-15 Comparison of the amplitudes of major harmonics.

Therefore, the shape of the harmonics with the circumferential order $v = 0$ is the same as the vibration mode *circ* = 0. Provided that the forcing frequency, u of the harmonic is non-zero, this harmonic with $v = 0$ can excite vibration mode *circ* = 0. Similarly, the shape of the harmonics with a circumferential order of 8, 16 and 24 are the same as the vibration mode *circ* = 8, 16 and 24, respectively. Provided that the forcing frequency of these harmonics are non-zero, they can excite vibration modes *circ* = 8, 16, and 24 respectively. After the superposition of the harmonics, the amplitudes of the dominant harmonics in the 24/16 SRM are shown in Fig. 4-15. In the 24/16 SRM, the amplitude of the harmonic

$F_{r(q=16,circ=16)}$ is the largest at 2000 rpm among all the harmonics. However, the harmonic with the highest magnitude might change at different speeds and in different designs with the same pole configuration. For the harmonics with the same circumferential order, the amplitude tends to reduce when the temporal order increases.

4.4.2 Natural Frequencies and Mode Shapes

The natural frequencies, ω_n, and the corresponding vibration mode shapes can be calculated and simulated by the numerical method in ACTRAN. In the numerical simulation, the boundary condition is clamped-free (C-F), in which the displacement of the housing are constrained from one end while the other end of the motor is free to vibrate. The mode shapes can be distinguished by the deformation in the circumferential and axial direction. Therefore, the corresponding natural frequencies are with different axial and circumferential orders. Table 4-4 shows the natural frequencies with the same axial order (axial order of 1), but with different circumferential orders. The mode shapes of vibration mode (2,1) and (0,1) are shown in Fig. 4-16. Vibration mode (0,1), whose natural frequency is 4784 Hz, has a circumferential order of 0 and an axial order of 1.

Table 4-4 Natural frequencies in different circumferential modes calculated by method of modal extraction in ACTRAN.

Vibration mode, (*circ*, *ax)*	(0,1)	(2,1)	(3,1)	(4,1)	(5,1)	(8,1)
Natural frequency [Hz]	4784	1782	4123	6810	9637	14963

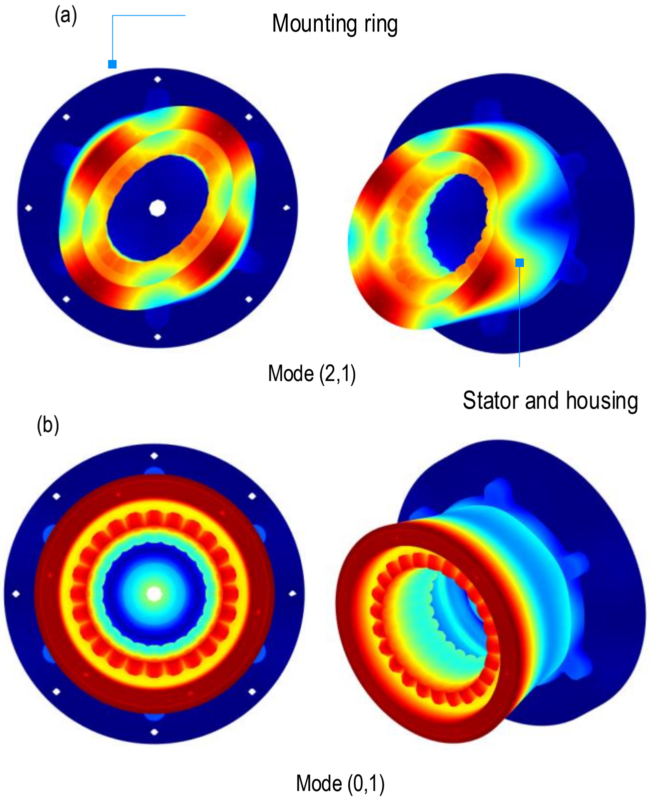

Fig. 4-16 Vibration mode shapes (a) Mode (2,1) (b) Mode (0,1)

4.4.3 Surface Displacement and Acoustic Noise

As discussed in the previous section, the harmonics with circumferential order of 0, 8, and 16 are the major harmonics that lead to vibration and acoustic noise in 24/16 SRM at 2000 rpm. The damping ratio used in the simulation of vibration and acoustic noise is calculated by [5]:

$$\zeta_{circ} = \frac{1}{2\pi}\left(2.76\times10^{-5} f_{circ} + 0.062\right) \tag{4.13}$$

where ζ_{circ} is the modal damping ratio, f_{circ} is the natural frequency of a given circumferential mode (*circ*).

An averaged damping ratio is used in this chapter by averaging the modal damping ratio of vibration mode *circ*=0 and *circ*=8. The modal damping ratio of the vibration mode *circ*=16 is not included in the calculation of the averaged damping ratio because the natural frequency of mode *circ*=16 exceeds 20 kHz, which would lead to an overestimated damping ratio.

The displacement measured by a virtual displacement sensor, which is mounted on the housing surface, is shown in Fig. 4-17(a). The location of this virtual displacement sensor was shown in Fig. 4-4(b). In the coupled simulation of vibration and noise, the 24/16 SRM starts its operation at t=0 ms and stops at t=7.5 ms. Fig. 4-17(b) shows the sound pressure captured by a virtual microphone (see Fig. 4-4(a)). The sound pressure starts to be captured at t= 2.14 ms, because the distance between the virtual microphone and the housing outer surface is 0.726 m and it takes 2.14 ms for the transmission of the sound wave from the housing surface to the virtual microphone. The value of 2.14 ms can also be calculated by the distance of 0.726 m divided by the speed of air, 340 m/s. After the motor stops at the time step t=7.5 ms, the sound wave can still be captured from the time step t=7.5 ms to the time step t=9.64 ms. This is because the sound wave, which is caused by the vibration of the housing surface at the time step t=7.5 ms, needs 2.14 ms to transmit from the housing outer surface to the virtual microphones.

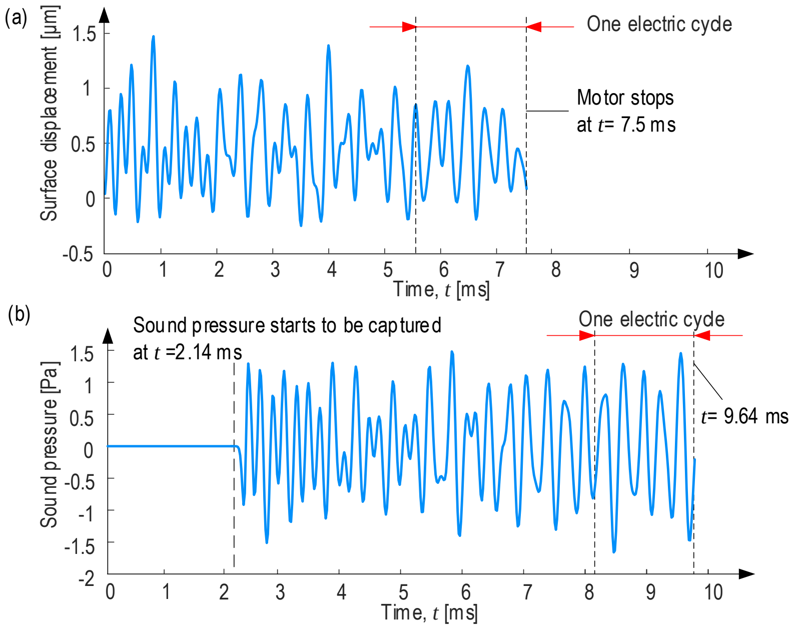

Fig. 4-17 Vibration and acoustic noise of the 24/16 SRM at 2000 rpm, (a) Displacement measured by a sensor on the housing outer surface, (b) Sound pressure measured by a microphone located 1m away from the motor center.

The surface displacement in Fig. 4-17(a) is used for the FFT analysis. The minimum required temporal length of the surface displacement for FFT analysis is one electric cycle rather than a complete mechanical cycle. Therefore, in order to reduce the computation cost, the coupled simulation of surface displacement and acoustic noise can be shortened to one electrical cycle.

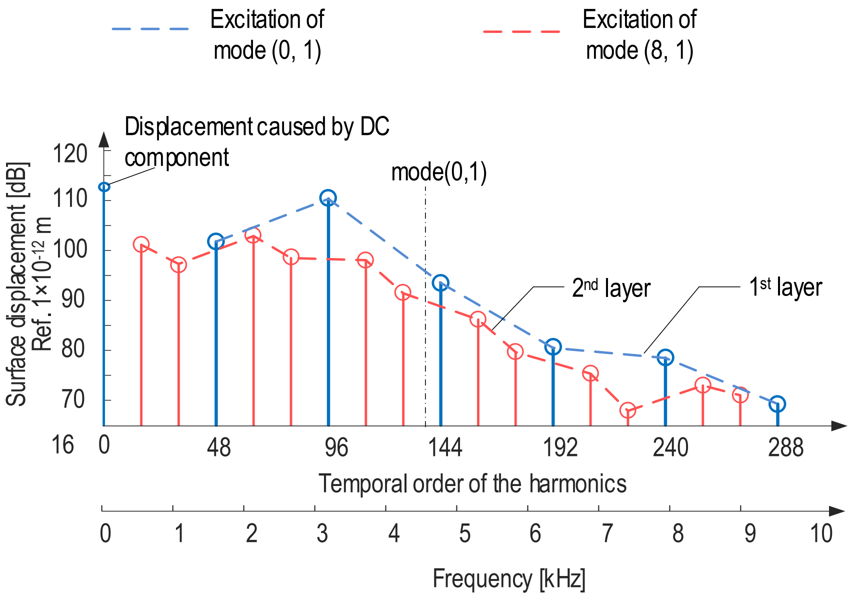

Fig. 4-18 Surface displacement of the 24/16 SRM at 2000 rpm.

The surface displacement in frequency domain is shown in Fig. 4-18. There are two layers. The first layer is the displacements caused by the harmonics $F_{r(q=48,circ=0)}$, $F_{r(q=96,circ=0)}$, $F_{r(q=144,circ=0)}$, $F_{r(q=192,circ=0)}$, $F_{r(q=240,circ=0)}$, and $F_{r(q=288,circ=0)}$. These harmonics have the same circumferential order. They only excite the vibration mode, *circ* =0, which has a circumferential order zero.

Although the forcing frequency of $F_{r(q=144,circ=0)}$ is closer to the natural frequency of vibration mode, *circ*=0, the amplitude of the harmonic $F_{r(q=96,circ=0)}$ is much higher than that of $F_{r(q=144,circ=0)}$ (see Fig. 4-15). For this reason, This layer peaks at 3200 Hz, which is caused by the harmonic $F_{r(q=96,circ=0)}$. The amplitudes of the harmonics $F_{r(q=48,circ=0)}$, $F_{r(q=96,circ=0)}$, $F_{r(q=144,circ=0)}$ decrease as they have higher temporal order (see Fig. 4-15). Therefore, the amplitude of the displacement decreases after 3200 Hz.

The displacement of the second layer is caused by the harmonics with the circumferential order 8 and the harmonics with the circumferential order 16, simultaneously. For example, the displacement at 533.33 Hz is caused by the harmonics $F_{r(q=16,circ=8)}$ *and* $F_{r(q=16,circ=16)}$ with the same temporal order, 16. This can be verified by the FFT of the nodal force shown in Table 4-3.

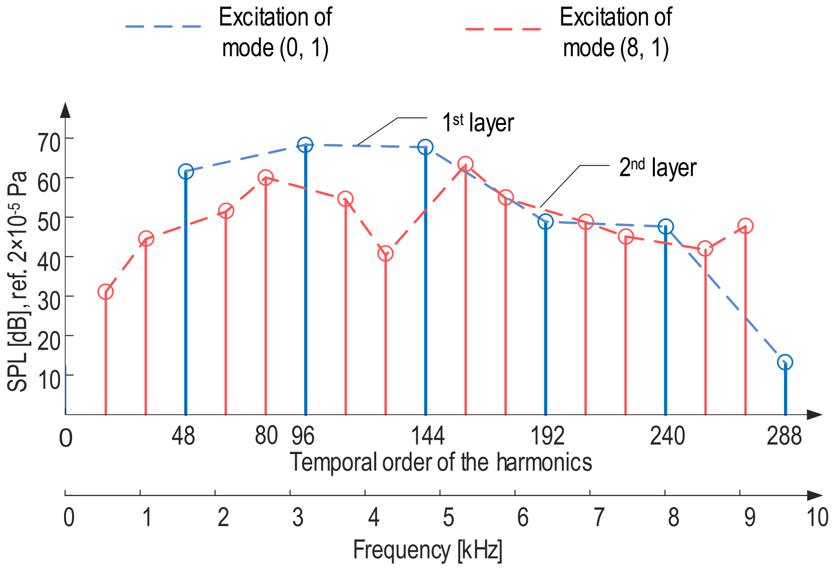

Fig. 4-19 SPL of 24/16 SRM at 2000 rpm.

By averaging the sound pressure measured by the 20 microphones on a hemisphere, the averaged sound pressure is obtained. The locations of the virtual microphones were shown in Fig. 4-4 and Fig. 4-5. Then the averaged sound pressure is used for the FFT decomposition. The sound pressure level (SPL) of the 24/16 SRM at 2000 rpm is shown in Fig. 4-19. Since the acoustic noise is caused by the surface displacement, there are also two layers in the SPL as well. Similar to the surface displacement, the first layer is caused by harmonics $F_{r(q=48,circ=0)}$, $F_{r(q=96,circ=0)}$, $F_{r(q=144,circ=0)}$, $F_{r(q=192,circ=0)}$, $F_{r(q=240,circ=0)}$, and $F_{r(q=288,circ=0)}$.

The SPL of the 24/16 SRM has two maximum values as shown in Fig. 4-19. These maximums occur at the frequency of 3200 Hz and 4800 Hz and they are caused by the harmonics of $F_{r(q=96,circ=0)}$ and $F_{r(q=144,circ=0)}$. In this case, a large magnitude of acoustic noise is generated since the forcing frequencies of $F_{r(q=96,circ=0)}$ (3200 Hz, see Table 4-3), and $F_{r(q=144,circ=0)}$ (4800 Hz, see Table 4-3), are close to the natural frequency of vibration mode, *circ* = 0, 4784 Hz.

If we compare the surface displacement for the same speed in Fig. 4-18 and the sound power in Fig. 4-19, we can notice that, although the surface displacement caused by $F_{r(q=144,circ=0)}$ is much smaller than that caused by $F_{r(q=96,circ=0)}$, the SPL caused by $F_{r(q=144,circ=0)}$ is close to that of $F_{r(q=96,circ=0)}$. This is because $F_{r(q=144,circ=0)}$ has a higher forcing frequency.

There are two peaks in the second layer of the SPL in Fig. 4-19, which appear at 2666 Hz and 5333 Hz. The acoustic noise generated in this layer is due to the harmonics exciting the vibration modes, *circ*=8 and *circ*=16. The SPL at this layer is caused by harmonics with the circumferential order 8 and 16, simultaneously.

4.5 Experimental Results

In order to validate the numerical model of the 24/16 SRM, the natural frequency of the experimental motor has been analyzed. For the 24/16 SRM, vibration mode (0,1) is the dominant vibrating mode. Its excitation, which is caused by the dominant harmonics of the radial force density, contributes mainly to the acoustic noise of the 24/16 SRM in this chapter. Therefore, the natural frequency of vibration mode (0,1) has been validated experimentally through a hammer test.

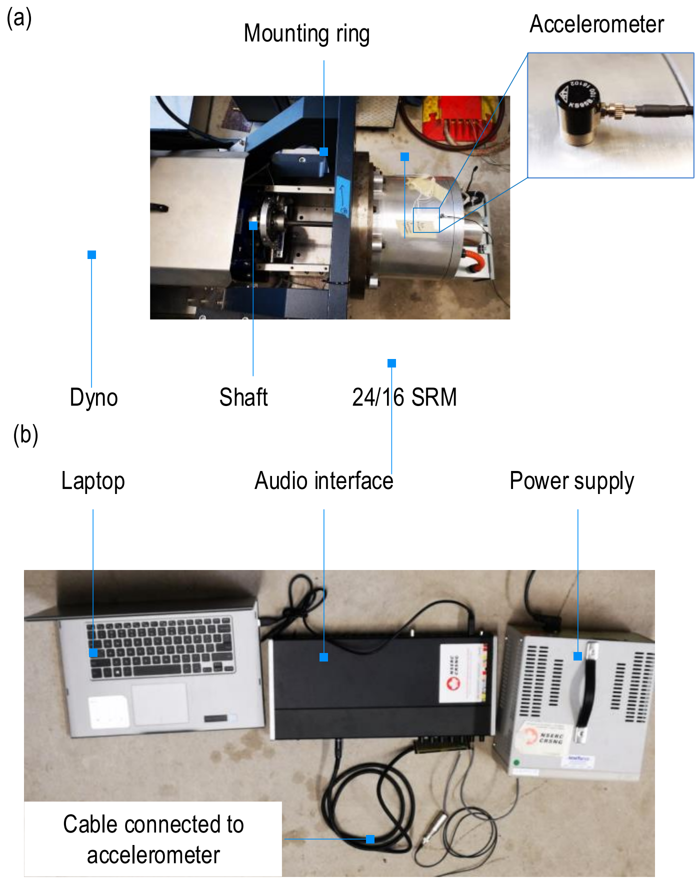

Fig. 4-20 Setup for the hammer test of the 24/16 SRM, (a) 24/16 SRM mounted in the dyno, (b) audio interface and power supply.

The setup for the hammer test of the 24/16 SRM is shown in Fig. 4-20. An accelerometer is mounted on the surface of the motor to measure the response of the surface acceleration.

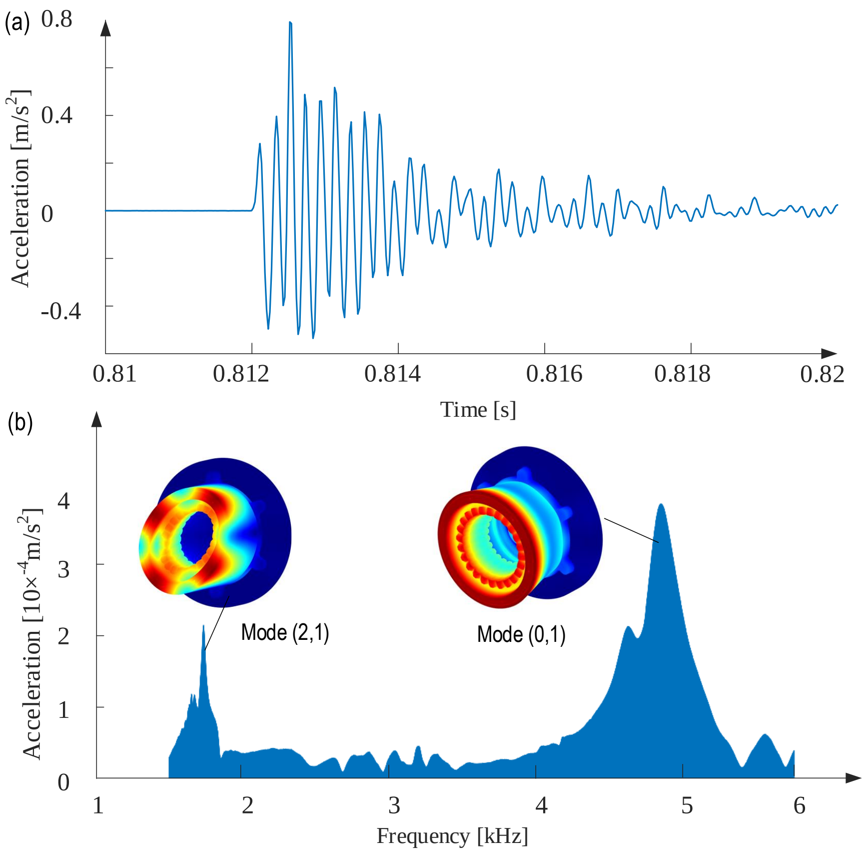

Fig. 4-21 Hammer test of the 24/16 SRM, (a) response in the time domain, (b) response in the frequency domain.

The response of the accelerometer in the time domain is shown in Fig. 4-21(a). After the FFT, the response in the frequency domain can be seen in Fig. 4-21(b). It can be observed that there are two major peaks appearing in 1735 Hz and 4852 Hz. As shown in Table 4-4, the simulated natural frequencies of vibration mode (2,1) and vibration mode (0, 1) were 1782 Hz and 4784 Hz, respectively. Therefore, there is a good match between the simulated natural frequency and the hammer test result for vibration mode (0, 1), which is the dominant vibration mode for the 24/16 SRM in this chapter.

4.6 Conclusions

In this chapter, a numerical modeling procedure has been presented to predict the vibration and acoustic noise caused by electromagnetic force harmonics in internal-rotor SRMs. This numerical model couples the electromagnetic analysis in JMAG, and modal, vibration and acoustic analysis in ACTRAN. Detailed considerations in the modeling to ensure the accuracy of the results and to reduce the computational cost are also presented. This chapter also proposes a useful method to quantitatively obtain and analyze the relationships between dominant harmonics of the radial electromagnetic force, dominant vibration mode, vibration (or surface displacement), and the radiated acoustic noise of an SRM. The acoustic results for a 24/16 IR SRM at 2000 rpm are shown as an example. The harmonics with circumferential order *circ* = 0, is found to excite the vibration mode *circ* = 0 and cause the maximum vibration and acoustic noise for a 24/16 SRM at 2000 rpm. Harmonics with high temporal order in the 24/16 SRM can lead to noise and vibration when the motor is operating at low and medium speed.

REFERENCES

[1] J. Gieras, C. Wang, and J. Lai, *Noise of Polyphase Electric Motors*. Boca Raton, FL, USA: CRC press, ISBN: 0-8247-2381-3, Dec. 2005.

[2] W. R. Finley, M. M. Hodowanec, and W. G. Holter, "An analytical approach to solving motor vibration problems," *IEEE Transactions on Industrial Electronics*, vol. 36, no. 5, pp. 217–232, May 2000.

[3] J. Dong, J. Jiang, B. Howey, H. Li, B. Bilgin, A. Callegaro, A. Emadi., "Hybrid acoustic noise analysis approach of conventional and mutually coupled switched reluctance motors," *IEEE Transactions on Energy Conversion*, vol. 32, no. 3, pp. 1042–1051, Feb. 2017.

[4] Z. Zhu, X. Liu, and Z. Pan, "Analytical model for predicting maximum reduction levels of vibration and noise in switched reluctance machine by active vibration cancellation," *IEEE Transactions on Energy Conversion*, vol. 26, no. 1, pp. 36–45, Mar. 2011.

[5] M. Anwar and I. Husain, "Radial force calculation and acoustic noise prediction in switched reluctance machines," *IEEE Transactions on Industrial Electronics*, vol. 36, no. 6, pp. 1589–1597, Nov./Dec. 2000.

[6] A. Putri, S. Rick, D. Franck, and K. Hameyer, "Application of sinusoidal field pole in a permanent-magnet synchronous machine to improve the NVH behavior considering the MTPA and MTPV operation area," *IEEE Transactions on Industrial Electronics*, vol. 52, no. 3, pp. 2280–2288, May/June 2016.

[7] M. Takiguchi, H. Sugimoto, N. Kurihara, and A. Chiba, "Acoustic noise and vibration reduction of SRM by elimination of third harmonic

component in sum of radial forces," *IEEE Transactions on Industrial Electronics*, vol. 30, no. 3, pp. 883–891, Sept. 2015.

[8] F. Santos, J. Anthonis, F. Naclerio, J. Gyselinck, H. Auweraer, and L. Goes, "Multiphysics NVH modeling: simulation of a switched reluctance motor for an electric vehicle," *IEEE Transactions on Industrial Electronics*, vol. 61, no. 1, pp. 469–476, Jan. 2014.

[9] M. Bösing, Acoustic Modelling of Electrical Drives, Ph.D. Dissertation, RWTH Aachen University, Dec.2013.

[10] C. Lin and B. Fahimi, "Prediction of acoustic noise in switched reluctance motor drives," *IEEE Transactions on Energy Conversion*, vol. 29, no. 1, pp. 250–258, Mar. 2014.

[11] S. Castano, B. Bilgin, E. Fairall, and A. Emadi, "Acoustic noise analysis of a high-speed high-power switched reluctance machine: frame effects," *IEEE Transactions on Energy Conversion*, vol. 31, no. 1, pp. 69–77, Mar. 2016.

[12] J. W. Jiang, B. Bilgin, and A. Emadi, "Three-phase 24 / 16 switched reluctance machine for a hybrid electric powertrain," *IEEE Transactions on Transportation Electrification*, vol. 3, no. 1, pp. 76–85, Feb. 2017.

[13] S. Marburg and B. Nolte, *Computational Acoustics of Noise Propagation in Fluids: Finite and Boundary Element Methods*, Germany: Springer, ISBN: 978-3-540-77448-8, Feb. 2008.

[14] R. Astley and J. Coyette, “The performance of spheroidal infinite elements,” *International Journal for Numerical Methods in Fluids*, vol. 52, no. 12, pp. 1379–1396, Sept. 2001.

[15] M. Norton and D. Karczub, *Fundamentals of Noise and Vibration Analysis for Engineers*. Cambridge, UK: Cambridge University Press, ISBN: 978-0521499132, Oct. 2003.

Chapter 5: Acoustic Noise Modeling and Analysis in External-Rotor Switched Reluctance Machines

5.1 Introduction

Due to the solid rotor structure of the internal-rotor (IR) SRMs, the acoustic noise caused by the vibration of the rotor is often negligible in IR SRMs. The stator and rotor pole heights are often short enough in IR SRMs so that the natural frequencies of the tangential modes of the poles are usually high. Thus, the acoustic noise caused by the tangential vibration of the stator and rotor poles is often negligible. Therefore, the radial vibration of the stator back iron is often the primary source of the acoustic noise in IR SRMs.

However, this is not necessarily the case for the external-rotor (ER) SRMs. Due to the differences in the designs compared with the IR SRMs, ER SRMs can show different vibration and acoustic noise behavior in the stator and the rotor. For example, the rotor back-iron of the ER SRM is often designed with a small thickness in order to reduce the inertia, and the stator can sometimes be designed with a long pole height to increase the average torque. These design differences make the acoustic noise modeling and analysis of the ER SRMs different from the

IR SRMs. The thin rotor back iron affects the modal stiffness and the mass of the rotor-endcap subassembly, which affects the natural frequencies of the dominant radial vibration modes of the rotor-endcaps subassembly. Besides, if a long stator pole height is adopted in the design of an ER SRM, it tends to reduce the natural frequencies of the tangential vibration modes of the stator pole. All the aforementioned features of the ER SRMs can make the tangential vibration of the stator poles one of the sources of acoustic noise in ER SRMs.

This chapter aims to model and analyze the vibration behavior and the acoustic noise in ER SRMs. One issue that will be addressed in this chapter is whether the radial vibration of the rotor back iron or the tangential vibration of the stator poles is the primary source of the acoustic noise in ER SRMs. First, two numerical models will be built to simulate the vibration and acoustic noise in the rotor-endcaps and the stator-shaft subassemblies, respectively. Then, the vibration modes, the electromagnetic force harmonics, the vibration and acoustic noise behavior of the stator and the rotor will be compared. A 12/16 ER SRM designed for a direct-drive e-bike application will be used for the modeling and analysis of vibration and acoustic noise in this chapter.

5.2 12/16 External-Rotor Switched Reluctance Motor

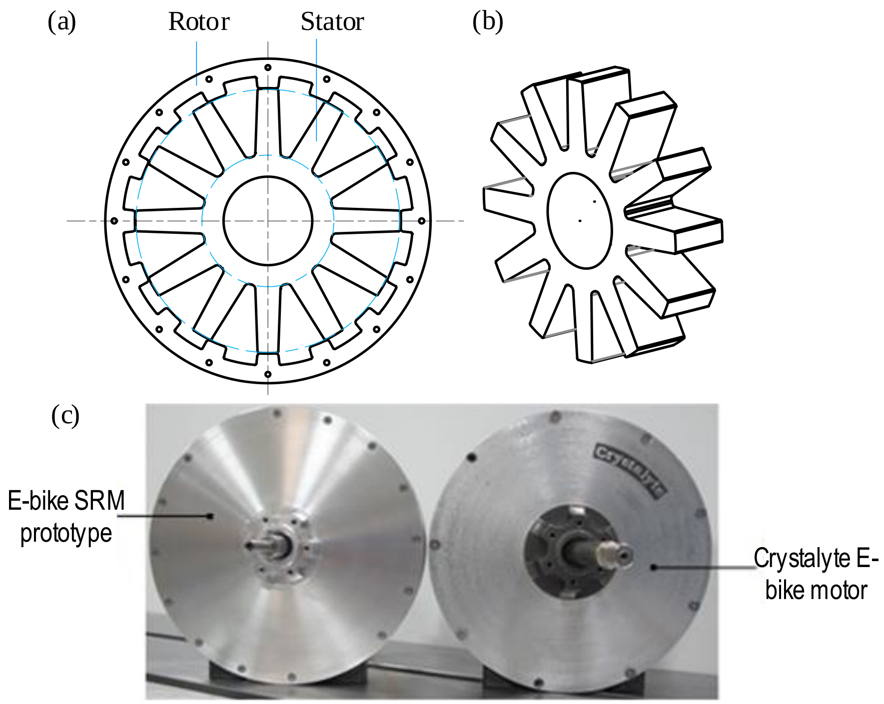

Fig. 5-1. Geometries of the 12/16 external-rotor SRM: (a) CAD drawing of the assembly, (b) 3D drawing of the stator, (c) prototype of the E-bike motor.

The 12/16 ER SRM is designed based on the geometry constraints and performance targets of the commercial Crystalyte HS3548 e-bike motor, which is a surface permanent magnet synchronous motor. The axial length, stack length, and the outer diameter of the motor are 52.5 mm, 34.1 mm, and 220 mm, respectively. The motor can operate at its max speed, 400 rpm, with 36 V DC link voltage. In [1], different pole configurations have been compared and evaluated, and it was concluded that a 12/16 SRM can provide the best performance in terms of average torque, torque quality, and efficiency. The 12/16 SRM prototype can deliver 38 Nm at 100 rpm. Fig. 5-1 shows the geometry and the prototype of the 12/16 ER motor. It can be observed that the pole height of the stator is much larger than that of the rotor, and the rotor back iron is thin. This chapter will discuss how these design features affect the vibration behavior and acoustic noise in ER SRMs.

5.3 Acoustic Noise Modeling and Analysis

5.3.1 Mechanism of Vibration Generation

This section will first discuss the vibration mechanisms when the radial and tangential force density excite the motor structure. The radial and tangential force densities cause vibrations in different ways. As shown in Fig. 5-2, the radial force density can excite the radial vibration modes and causes the radial vibration of the back iron. On the other hand, the tangential force density excites the tangential vibration modes of the poles, causing tangential vibration.

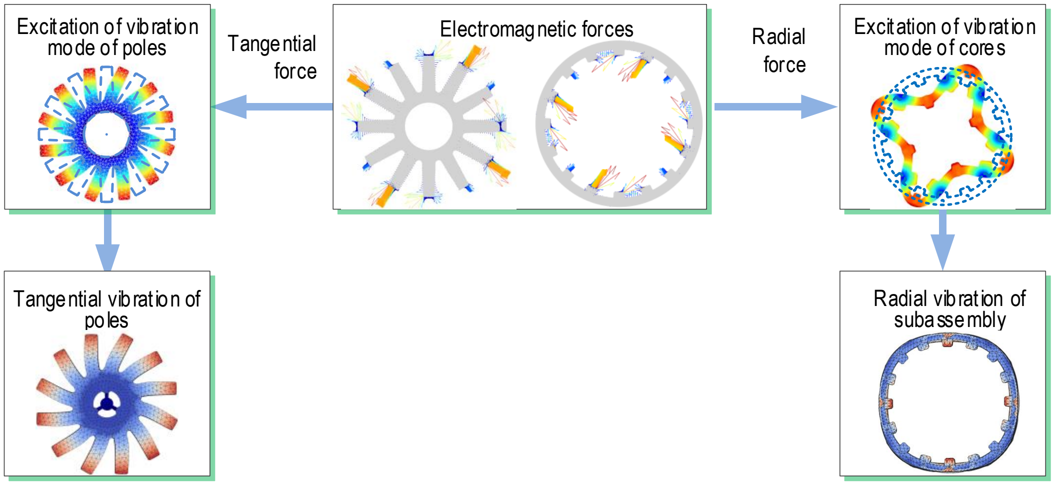

Fig. 5-2 Vibration caused by the radial and tangential electromagnetic forces.

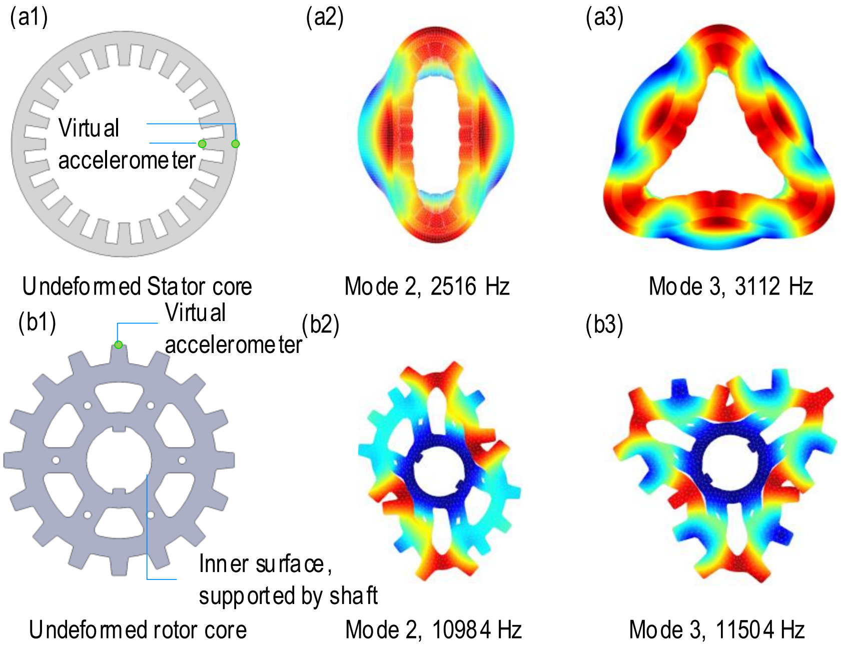

Fig. 5-3 Mode shapes of the stator and rotor cores with different circumferential order in a 24/16 IR SRM, (a) stator, (b) rotor.

The radial force density can excite the radial vibration modes of both the stator and rotor. However, for an IR SRM, the radial stiffness of the rotor back iron is typically higher than that of the stator. The reverse is usually true for ER SRMs. In ER SRMs, the rotor diameter is larger and the rotor back iron thickness is smaller. The comparison of different mode shapes in the stator and rotor of a 24/16 IR SRM with different circumferential orders and with the first axial order is shown in Fig. 5-3. The material properties and the boundary conditions for the simulation of natural frequencies are provided in the Appendix. The natural frequency of the circumferential mode two of the stator (2516 Hz) in Fig. 5-3(a2) is much lower than that of the rotor (10894 Hz) for the 24/16 SRM. Similarly, the mode three natural frequency of the stator is also lower than that of the rotor. Due to much higher natural frequencies in the circumferential mode shapes of the rotor in the IR SRM or the stator of ER SRM, they are typically more difficult to be excited compared with the stator of the IR SRM or the rotor of the ER SRM.

Table 5-1 Comparison of the first tangential modes of the stator and rotor poles.

SRM	12/16 ER	6/4 IR	24/16 IR	8/6 IR	6/14 IR
Stator OD [mm]	179.2	160	264	170	139.2
Stator ID [mm]	60	90.6	184	90	99.2
Rotor OD [mm]	220	90	183	89.3	98.4
Rotor ID[mm]	180	25	50	30	12.7
Stack length[mm]	39.5	75	92	90	74
Stator pole height [mm]	45	19.7	25	23	10
Rotor pole height [mm]	8	15	14.5	10.2	7
NF* of the 1st tangential mode of stator pole [Hz]	6,243	31,192	18,565	21,996	54,751
NF of the 1st tangential mode of rotor pole [Hz]	65,155	39,329	38,575	44,603	83,236

* NF stands for the natural frequency

The tangential vibration in the poles, which is caused by the tangential force density, is almost often negligible or appears in the very high-frequency range for IR SRMs. The tangential vibration of the poles happens when the forcing frequencies of the tangential force density harmonics are close to the natural frequencies of the tangential vibration modes of the poles. However, the natural frequencies of the tangential modes of the poles in IR SRMs are usually very high, which makes them difficult to excite.

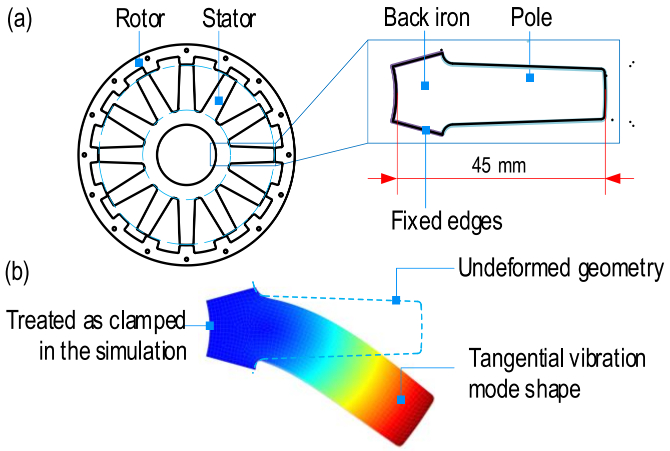

Fig. 5-4 Tangential vibration mode of a single stator pole of a 12/16 ER SRM modeled as a cantilever, (a) the geometry of a 12/16 ER SRM and a stator pole, (b) mode shape of the first tangential vibration mode of a stator pole.

The natural frequency of the tangential vibration mode in a pole can be calculated and simulated by treating the pole as a cantilever, as shown in Fig. 5-4. Table 5-1 shows the comparison of the first tangential mode of the poles in several SRMs. The material properties for the simulation of the tangential vibration mode in the stator and rotor poles in the 6/4, 24/16, 6/14, 8/6 IR SRM, 12/16 ER SRM are 175 GPa for Young's modulus, 7600 kg/m^3 for material mass density and 0.285 for Poisson's ratio. The natural frequencies of the first tangential vibration mode of the stator or rotor poles in 6/4, 24/16, 8/6, 6/14 IR SRM are very high and exceed 15 kHz. For IR SRMs with an operating speed smaller than 10k RPM, the forcing frequencies of the dominant harmonics are usually smaller than 10 kHz. Therefore, the tangential vibration mode of poles in IR SRMs is difficult to be excited. The natural frequency of the first tangential vibration mode in the stator pole of the 12/16 ER SRM is 6273 Hz. This is because the stator pole has a long pole height. Therefore, the tangential vibration caused by the stator poles of the 12/16 ER SRM can be one of the sources of the acoustic noise in this motor. In the following sections, the acoustic noise caused by the radial vibration of the rotor and the tangential vibration of the stator will be simulated and compared.

5.3.2 Modeling Considerations

Fig. 5-5 shows the motor assembly, rotor-shaft subassembly, and the stator-shaft subassembly of the 12/16 ER SRM. The geometry of the shaft has been simplified to reduce the required thickness in the meshing of the near field (hence to reduce the computation cost) without sacrificing the accuracy. As shown in Fig. 5-6, two numerical models are built to study and compare the vibration behavior and the acoustic noise of the motor subassemblies: (a) rotor subassembly model to simulate the radial vibration of the rotor, (b) stator subassembly model to simulate the tangential vibration of the stator poles. Each model consists of the simulation of vibration modes, generation of the nodal forces, analysis of the radial or tangential force density harmonics, and the simulation of the vibration and acoustic noise.

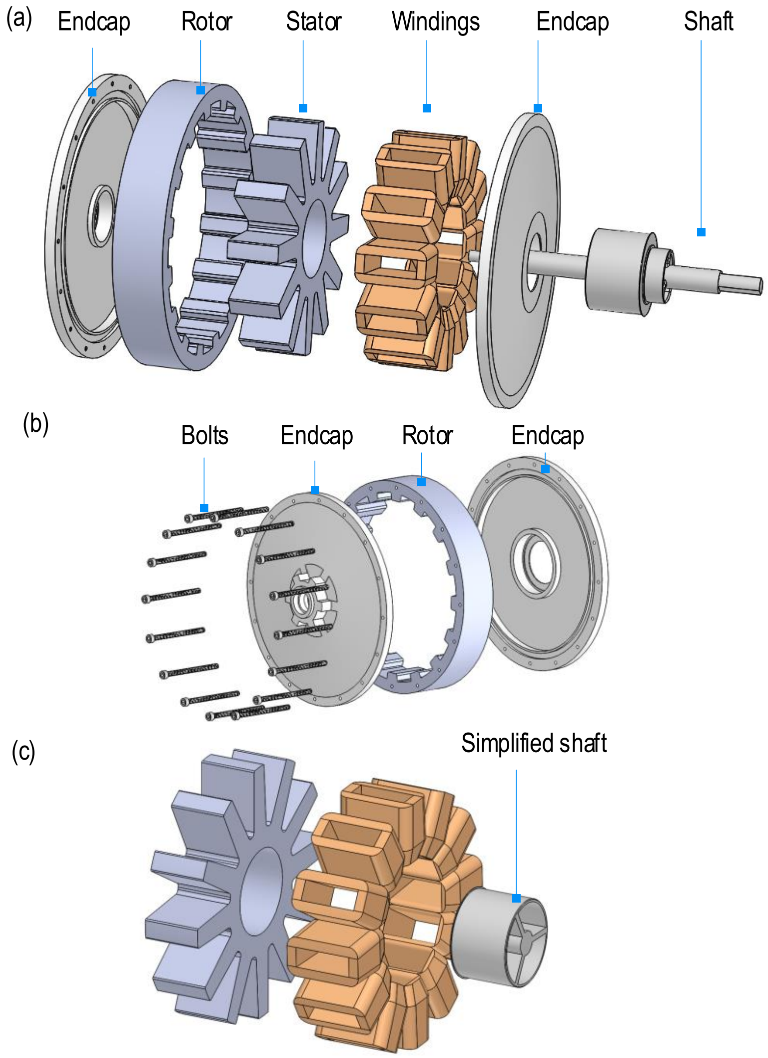

Fig. 5-5. Assembly of the 12/16 E-bike SRM, (a) motor assembly, (b) rotor-endcaps subassembly, (c) stator-shaft-winding subassembly.

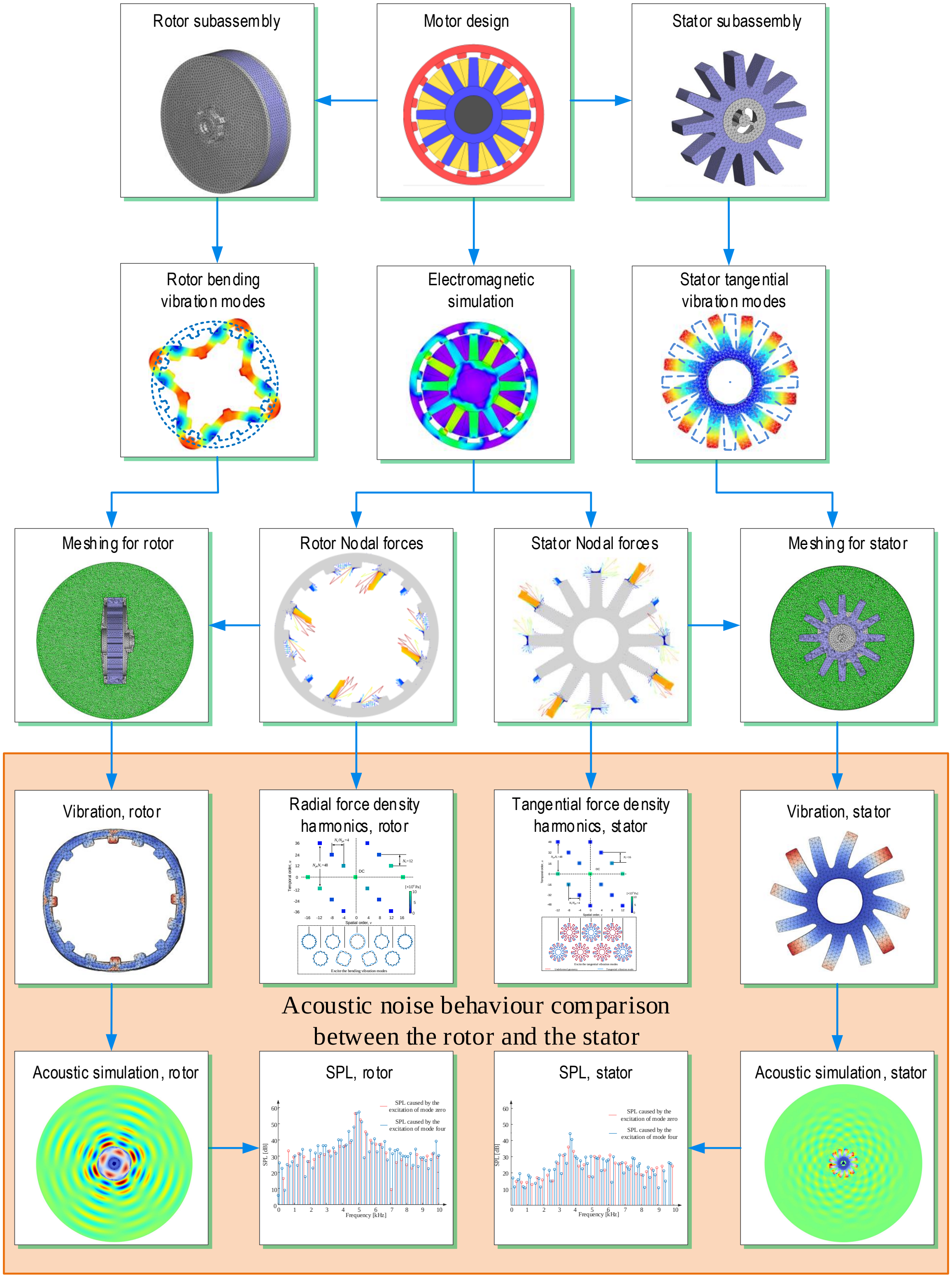

Fig. 5-6 Two acoustic noise models for the rotor and stator subassemblies.

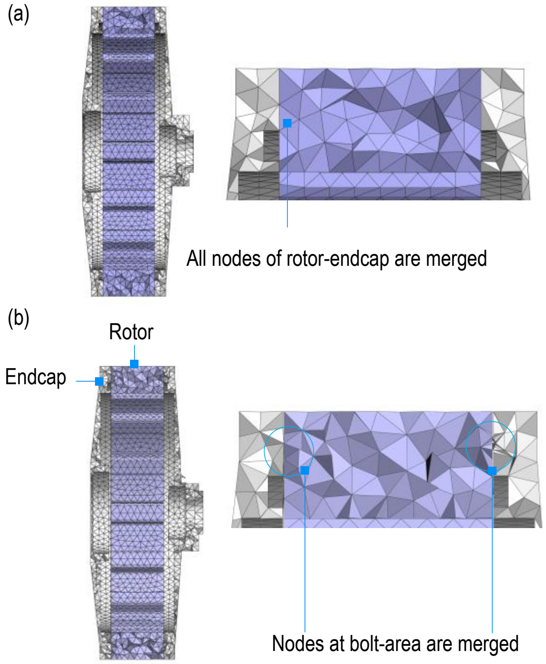

Fig. 5-7. Contacts between parts in the modal simulation for the rotor subassembly.

It should be noted that the contacts between the rotor and the endcaps affect the simulation accuracy. Fig. 5-7 shows how the contacts between the rotor and the endcaps are built. In the prototype of this motor, the rotor and the endcaps are connected by bolts only. In order to model the contact between the rotor and the endcaps correctly, only the nodes at the bolt area of the rotor-endcap interface should be merged, as shown in Fig. 5-7(b). The boundary conditions for the simulation of the natural frequencies in the two subassemblies are shown in Fig. 5-8.

The meshing of the near fields and the motor structures for the rotor-endcaps and the stator-shaft subassemblies are shown in Fig. 5-9. The near filed is thick enough and the element size in the meshing of the near field is fine enough to ensure the simulation accuracy.

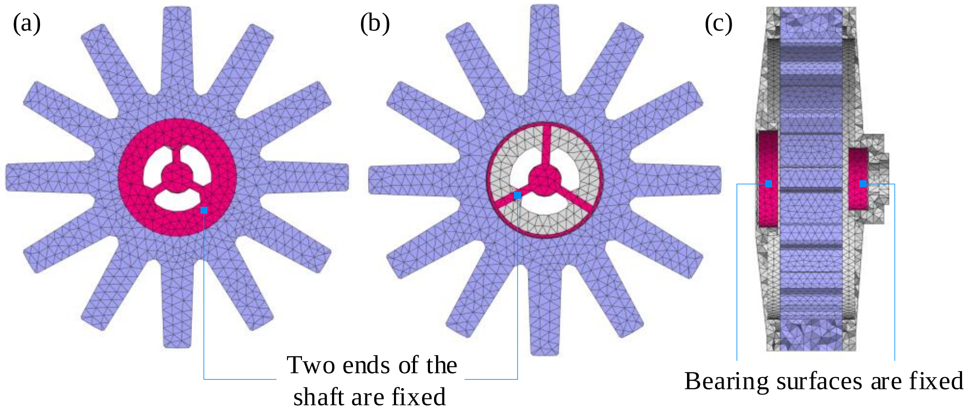

Fig. 5-8 Boundary conditions, (a) front view of the stator-shaft subassembly, (b) back view of the stator-shaft subassembly, (c) rotor-endcaps subassembly.

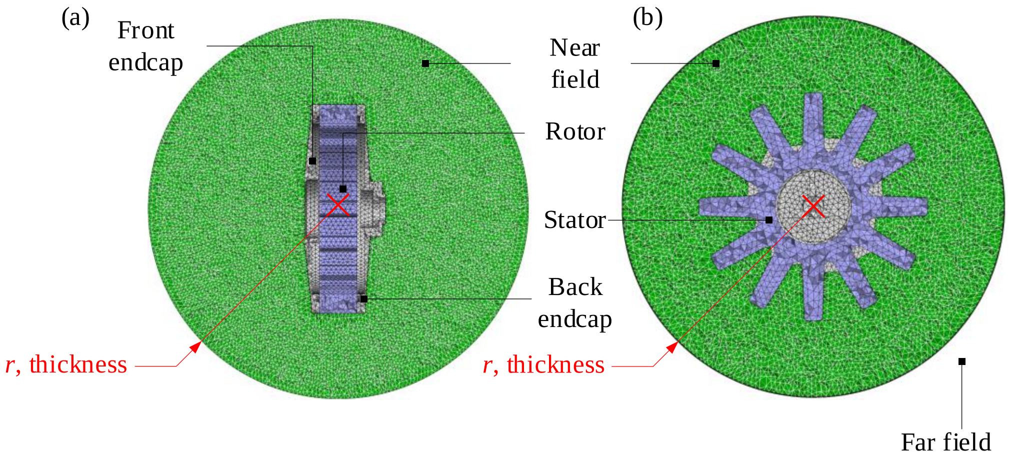

Fig. 5-9 Meshing of the motor structure and the near field, (a) rotor-endcaps subassembly, (b) stator-shaft subassembly.

5.3.3 Analysis of the Vibration Modes

The simulation of the vibration modes presented in this section is conducted by using the numerical method in ACTRAN. Fig. 5-10 shows the radial vibration modes of the rotor-endcaps subassembly, where the free deformation and vibration appear in the radial direction. It will be shown in

Section 5.3.4 that the radial vibration modes four and zero are the dominant vibration modes of the rotor-endcaps subassembly. It can also be observed that the natural frequencies of mode four and zero are quite high.

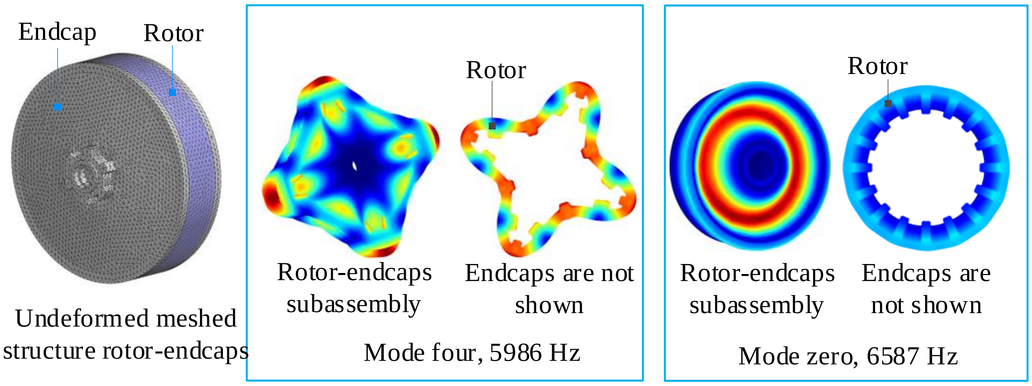

Fig. 5-10 Vibration modes of the rotor-endcaps subassembly.

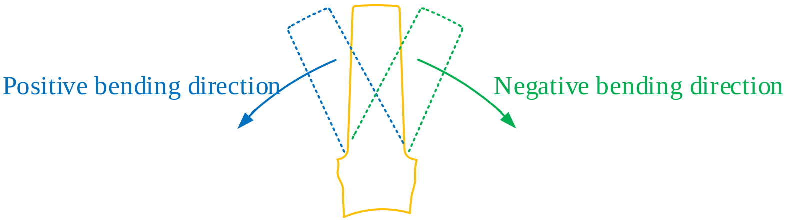

Fig. 5-11 Illustration of the bending directions in a stator pole.

Before the discussion of the tangential vibration modes of the stator poles, it should be noted that a pole can vibrate and bend in either the positive (counter clockwise) or negative (clockwise) direction, as shown in Fig. 5-11. Fig. 5-12 shows the vibration modes in the stator of the ER SRM. In Fig. 5-12 (b), the tangential vibration mode zero of the stator-shaft subassembly is shown. It can be seen that all the stator poles bend in the same direction. Tangential vibration mode zero is one of the dominant vibration modes for the stator-shaft subassembly. This will be verified in the analysis of the electromagnetic force density harmonics in

Section 5.3.4 and the simulated SPL diagram in Section 5.4. Tangential mode four is shown in Fig. 5-12 (c). It can be seen that there are four groups of stator poles with significant free deformation in the tangential vibration mode four. Each group consists of two stator poles and these two poles bend in opposite directions.

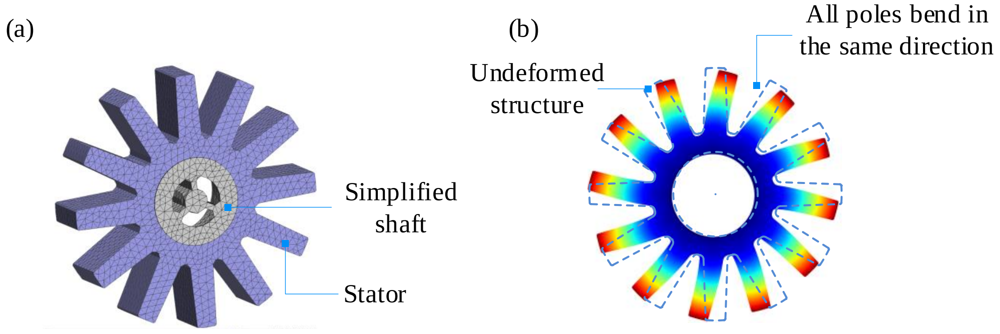

Undeformed stator and shaft

Tangential mode zero, 3988 Hz

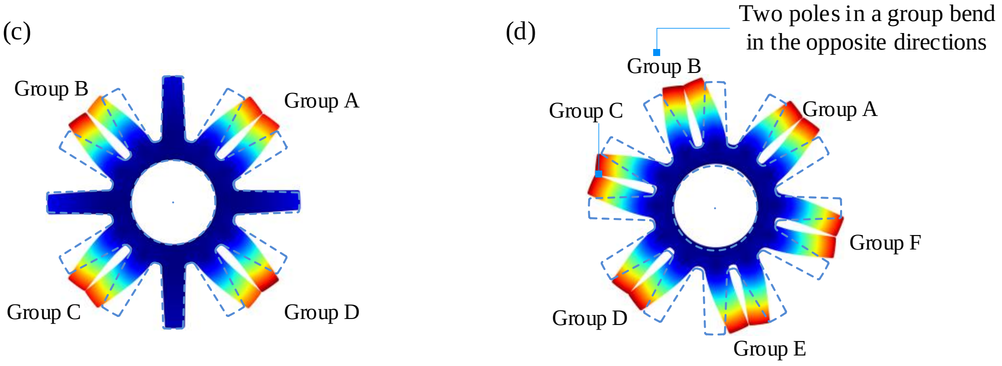

Tangential mode four, 4186 Hz

Tangential mode six, 4137 Hz

Fig. 5-12 Vibration modes of the stator with 12 poles, (a) undeformed structure, (b) tangential mode zero, (c) tangential mode four, (d) tangential mode six.

Tangential mode six is shown in Fig. 5-12 (d), where six groups of stator poles with significant free deformation can be observed. It can be concluded that the largest tangential vibration mode of the stator is limited by the number of stator poles. For this stator with twelve poles, mode six is the largest mode number of the tangential vibration mode. Any tangential vibration mode that has a mode number higher than six does not exist for this stator. This is not the case for the radial vibration modes of the rotor. The largest mode number of the radial vibration mode is not related to the number of rotor poles. This is because the rotor poles can be regarded as additional mass and stiffness attached to the rotor back iron.

5.3.4 Analysis of the Electromagnetic Force Density Harmonics

Before presenting the analysis and discussion of the simulated vibration and the acoustic noise of the 12/16 ER SRM, the harmonic components in the tangential force density of the stator and the radial force density of the rotor need to be analyzed. First, the tangential force density on the stator pole tip and the radial force density on the rotor pole tip are extracted after running the 2D electromagnetic FEA simulation.

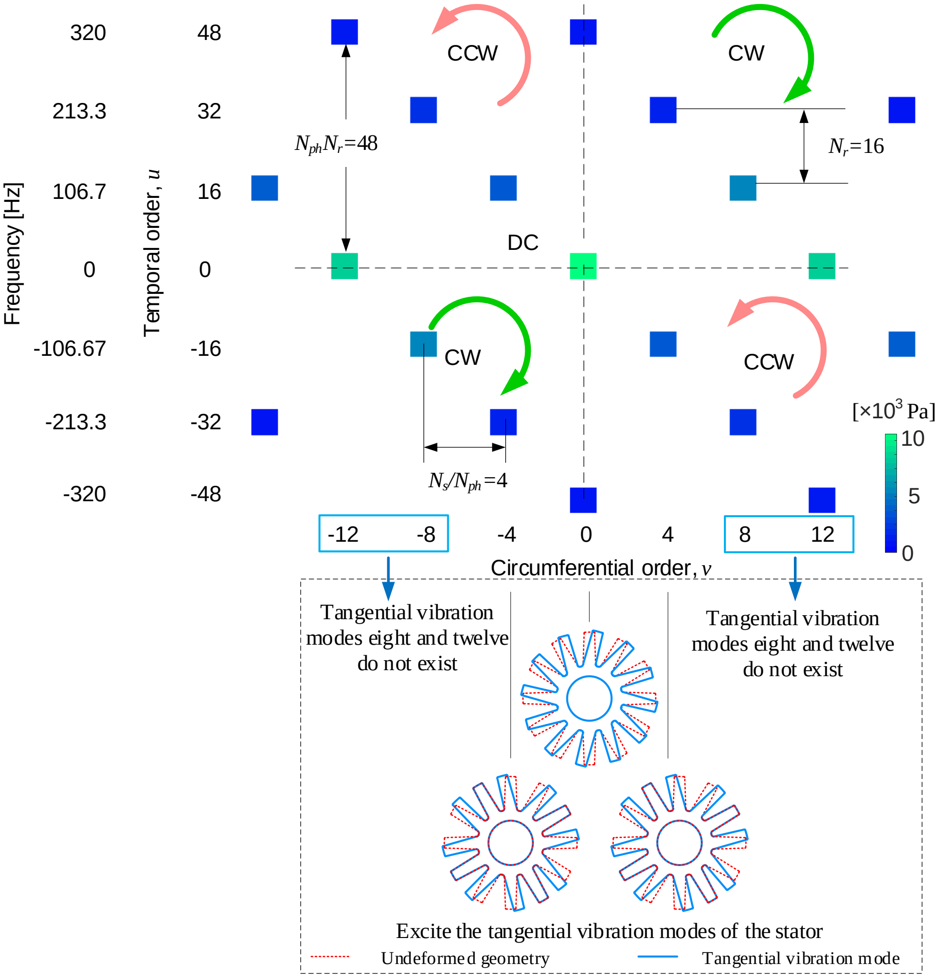

Fig. 5-13. Tangential force density harmonics in the 12/16 ER SRM stator when the rotor rotates at 400 RPM, CCW direction, where the frequencies of the harmonics can be calculated by u × 6.67.

5.3.4.1 Tangential Force Density Harmonics of the Stator

Fig. 5-13 shows the tangential force density harmonics of the 12/16 ER SRM stator. Since the tangential force density is applied in the tangential direction, it only causes tangential vibration on the stator poles. Fig. 5-13 also shows how different tangential vibration modes of the stator will be excited.

When the absolute value of the circumferential order is smaller than or equal to four, the tangential force density harmonics excite the corresponding circumferential order of the tangential vibration mode. This is because mode six is the largest mode number of the tangential vibration mode in this 12-pole stator, as discussed in Section 5.3.3. The tangential force density harmonics in Fig. 5-13 do not have the 6th circumferential order, because this is a four-pole motor and the circumferential orders are in multiples of four.

When the absolute value of the circumferential order is higher than four, the corresponding tangential vibration mode cannot be excited because these vibration modes do not exist. In this case, the tangential force density harmonic excites a smaller circumferential-order tangential vibration mode due to the sampling effect.

Fig. 5-14 shows how the waveform of the high-circumferential-order harmonic is sampled when it is applied to the stator with 12 poles. For better illustration, it is assumed that the stator is cut in half and open flat. Taking the harmonic with the 8th circumferential order (see Fig. 5-14 (a)) as an example, there are eight peaks and eight troughs in the waveform of the harmonic (the blue line in Fig. 5-14(a)) before the sampling. After the sampling, there are four peaks and four troughs, which will excite the vibration mode four. Similar cases apply to the harmonics with 16th and 20th circumferential order as shown in Fig. 5-14 (c) and Fig. 5-14 (d), respectively. For the harmonics with the 12th circumferential order, there are no peaks and troughs after the sampling; hence, it excites the vibration mode zero.

(a) N_s = 12, |v| = 8, after sampling |v’| = 4 (b) N_s = 12, |v| = 12, after sampling |v’| = 0

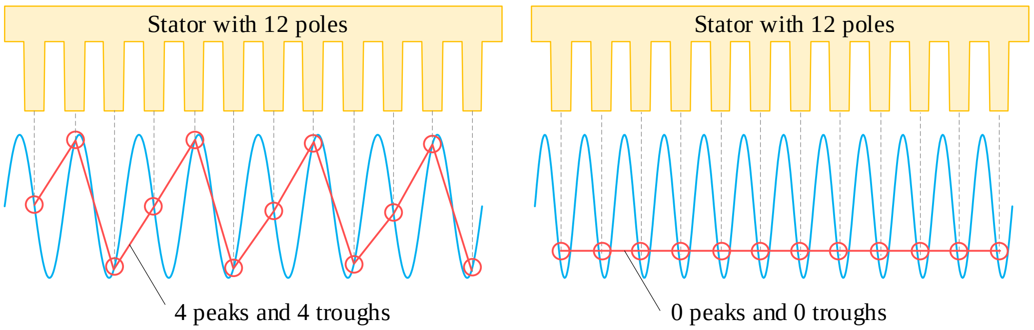

(c) N_s = 12, |v| = 16, after sampling |v’| = 4 (d) N_s = 12, |v| = 20, after sampling |v’| = 4

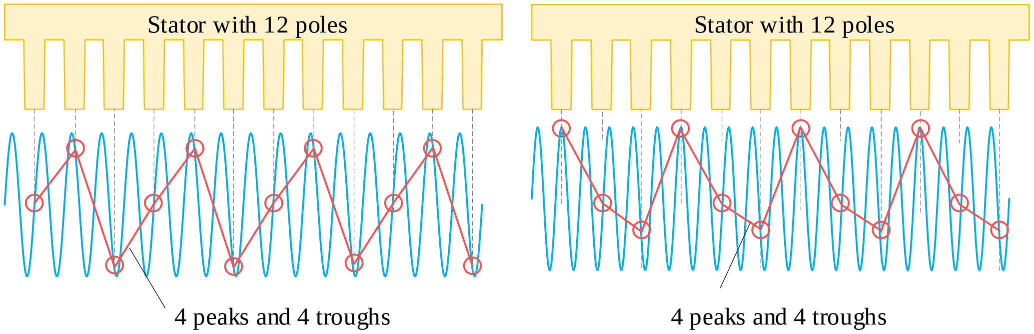

Fig. 5-14. Sampling effect of the high-circumferential-order electromagnetic force density harmonics, (a) |v| = 8, after sampling |v’| = 4, (b) |v| = 12, after sampling |v’| = 0, (c) |v| = 16, after sampling |v’| = 4, (d) |v| = 20, after sampling |v’| = 4.

5.3.4.2 Radial Force Density Harmonics of the Rotor

The radial force density harmonics of the rotor of the 12/16 ER SRM are shown in Fig. 5-15. When the circumferential order is smaller than or equal to eight, the harmonics in the rotor radial force density excites the same circumferential order of the radial vibration mode. For example, the radial force harmonics with the circumferential order eight excites the radial vibration mode eight.

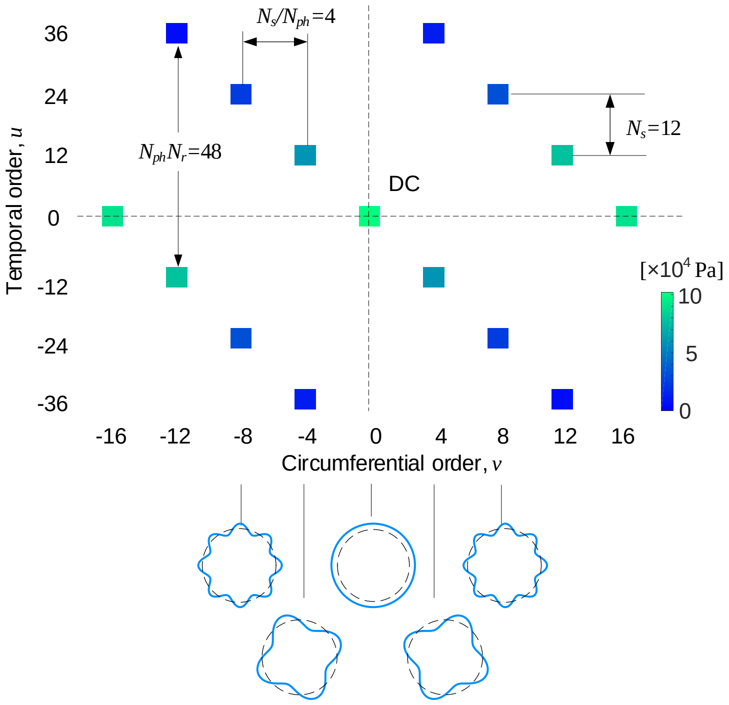

Fig. 5-15. Radial force density harmonics in the rotor of the 12/16 ER SRM when the rotor rotates in the CCW direction.

5.3.4.3 Summary of the Electromagnetic Force Density Harmonics

The rotor radial force density harmonics and the stator tangential force density harmonics can be summarized by using (5.1) and (5.2), respectively. It should be noted that these two equations are related to the topology, the phase excitation sequence, and the rotor rotational direction of the 12/16 external-rotor SRM. The comprehensive analysis of the pattern in the radial force density harmonics of external-rotor and internal-rotor SRMs will be presented in Chapter 7.

$$\text{For rotor} \begin{cases} u = N_r \times N_{ph} \times j - N_s \times k = 48 \times j - 12 \times k \\ v = \dfrac{N_s}{N_{ph}} \times k = 4 \times k \end{cases} \tag{5.1}$$

$$\text{For stator} \begin{cases} u = N_r \times N_{ph} \times j - N_r \times k = 48 \times j - 16 \times k \\ v = \dfrac{N_s}{N_{ph}} \times k = 4 \times k \end{cases} \tag{5.2}$$

where j and k can be any arbitrary integer, N_r is the number of rotor poles, N_s is the number of stator poles.

Table 5-2 Temporal and circumferential orders, (|*u*|, |*v*|) of the harmonics in the force density of 12/16 ER SRM rotor and stator when the rotor rotates in the CCW direction.

Part	**Force direction**	**Temporal order, |*u*|**	**Circumferential order, |*v*|**
Stator	Tangential	48, 96, 144, 192, 240, 288, 336…|48 × *j*|	0
		16, 32, 64, 80, 112, 128, 160, 176, 208, 224, 256, |-16 + 48 × *j*|	4
		16, 32, 64, 80, 112, 128, 160, 176, 208, 224, 256, |-32 + 48 × *j*|	8
Rotor	Radial	48, 96, 144, 192, 240, 288, 336, 384, 432…|48 × *j*|	0
		12, 36, 60, 84, 108, 132, 156, 180…|-12 + 48 × *j*|	4
		24, 72, 120, 168, 216, 264, 312…|-24 + 48× *j*|	8

*: *j* can be any integer.

Some harmonics with circumferential order zero, four, and eight are shown in Table 5-2. Please note that the temporal orders for the 0th-circumferential-order harmonics of the rotor and the stator are exactly the same.

This is because in this case the temporal orders for the harmonics of the stator and the rotor are only related to the number of strokes, $N_r \times N_{ph}$. Table 5-3 shows the frequencies of the dominant harmonics when the motor operates at 400 rpm. These frequency points will be used to explain the simulated and tested SPL in Section 5.4.

Table 5-3 Frequencies of the harmonics in the force density of 12/16 ER SRM rotor and stator when the rotor rotates at 400 rpm, CCW direction.

Part	**Force direction**	**Frequency [Hz]**	**Circumferential order, $\|v\|$**
Stator	Tangential	320, 640, 960, 1280, 1600, 1920, 2240…$\|320 \times j\|$	0
		106.7, 213.3, 426.7, 533.3, 746.7, 853.3, 1066.7, 1173.3, 1386.7, 1493.3, 1706.7, $\|-106.7 + 320 \times j\|$	4
Rotor	Radial	320, 640, 960, 1280, 1600, 1920, 2240…$\|320 \times j\|$	0
		80, 240, 400, 560, 720, 880, 1040, 1200…$\|-80+320 \times j\|$	4
		160, 480, 800, 1120, 1440, 1760, 2080…$\|-160+320 \times j\|$	8

*: *j* can be any integer.

5.4 Results and Discussions

Following the modeling and simulation procedures presented in Fig. 5-6, the vibration behavior and the acoustic noise are simulated by using the numerical method. Fig. 5-16 shows the displacement in the rotor and the stator of the 12/16 ER SRM at 400 rpm with a reference current of 75 A at $t = 0.19$ s. It can be seen that the displacement in the rotor is a combination of the displacements caused by the excitations of the radial vibration mode four and zero. The displacement of the stator, which is shown in Fig. 5-16(b), is caused mainly by the excitation of the tangential vibration mode zero (see Fig. 5-12(b)) and vibration mode four (see

Fig. 5-12 (c)). In Fig. 5-16(b), all the stator poles bend in the clockwise direction, because in vibration mode zero, all the stator poles have the same displacement in the same direction as shown in Fig. 5-12(b). However, in Fig. 5-16(b), the stator poles of different phases have different displacements. Medium displacement can be observed on the stator poles A1, A2, A3, and A4. These stator poles belong to Phase A. The stator poles of Phase B (B1, B2, B3, and B4) have the largest displacement, and the stator poles of Phase C (C1, C2, C3, and C4) have the smallest displacement. This is due to the vibration mode four.

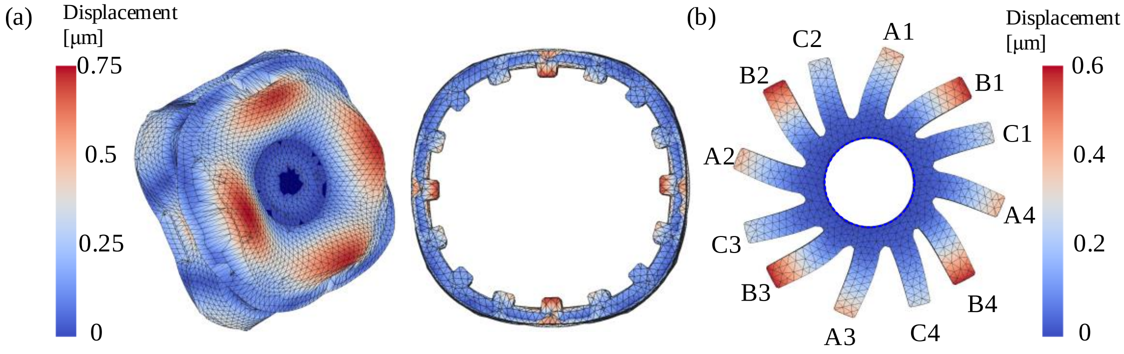

Fig. 5-16 Displacement in the 12/16 external-rotor SRM at 400 rpm with a reference current of 75 A, t = 1.13 ms, t = 0.19 s, (a) rotor, (b) stator.

As shown in Fig. 5-12(c), in vibration mode four, the stator poles vibrate in groups. Each group includes the stator poles of two different phases, which bend in opposite directions. The stator poles of the remaining phase does not have significant displacement. In Fig. 5-16(b), stator poles of Phase C and Phase B are the poles that belong to the vibrating groups in vibration mode four. In vibration mode four, the stator poles of Phase B bend in the same direction as in vibration mode 0. This is the reason why the stator poles B1, B2, B3, and B4 have the largest displacement. In vibration mode four, the stator poles of Phase C bend in the opposite direction as compared to vibration mode 0. This is the reason why stator poles C1, C2, C3, and C4 have the lowest displacement. In Fig. 5-16(b), the stator poles of Phase A do not belong to the group that vibrate in vibration mode four. Therefore, in this vibration mode, they do not have significant displacement. This is the reason why the stator poles A1, A2, A3, and A4 have the medium displacement in Fig. 5-16(b). The displacement of these stator poles is mainly due to vibration mode zero.

Fig. 5-17 and Fig. 5-18 show how the sound pressure develops and radiates from the vibrating rotor or stator, respectively. In order to clarify the difference between these two cases, Fig. 5-19 compares the sound pressure of the rotor and the stator at a certain time step. As shown in Fig. 5-19(a), for the rotor, the positive air pressure region designated by dashed lines is surrounded by two positive air pressure regions and two negative air pressure regions. This means that the sound pressure caused by the rotor travels in the radial direction only. The positive pressure regions can be considered as the peaks of a sinusoidal wave and the negative pressure regions as the troughs.

In Fig. 5-19 (b), for the stator, the positive pressure region designated by the dashed lines is surrounded by four negative air pressure regions. Therefore, the sound pressure caused by the stator travels in both the radial and the tangential directions. It travels in the tangential direction due to the tangential vibration caused by the stator poles as shown in Fig. 5-16(b). The sound pressure from the stator also travels in the radial direction. This is because the acoustic noise waveform is the source of acoustic noise and it needs to travel to the far field through the radial direction so it can reach human ears.

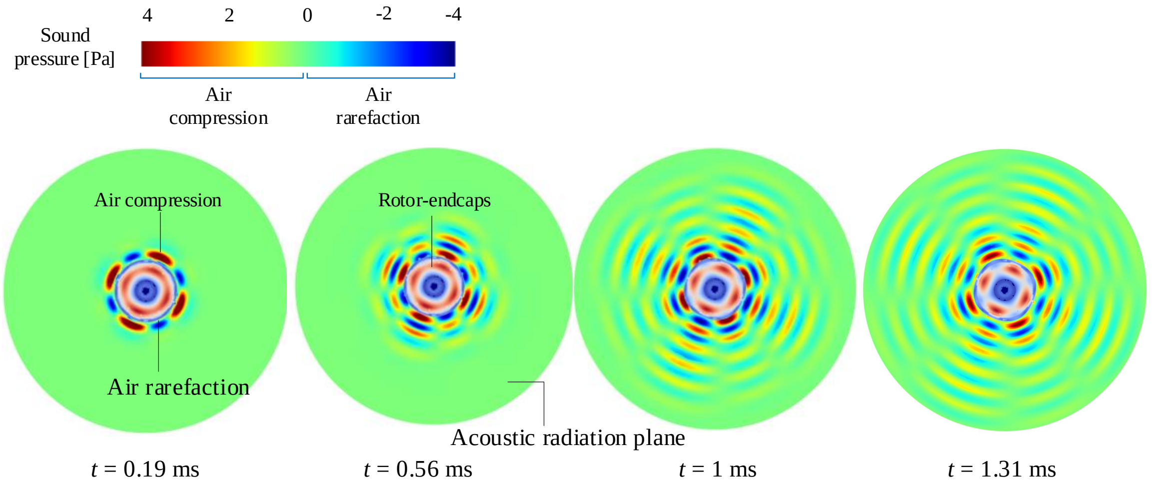

Fig. 5-17 Sound pressure map of the rotor-endcaps subassembly, 12/16 external-rotor SRM, 400 RPM with a reference current of 75 A.

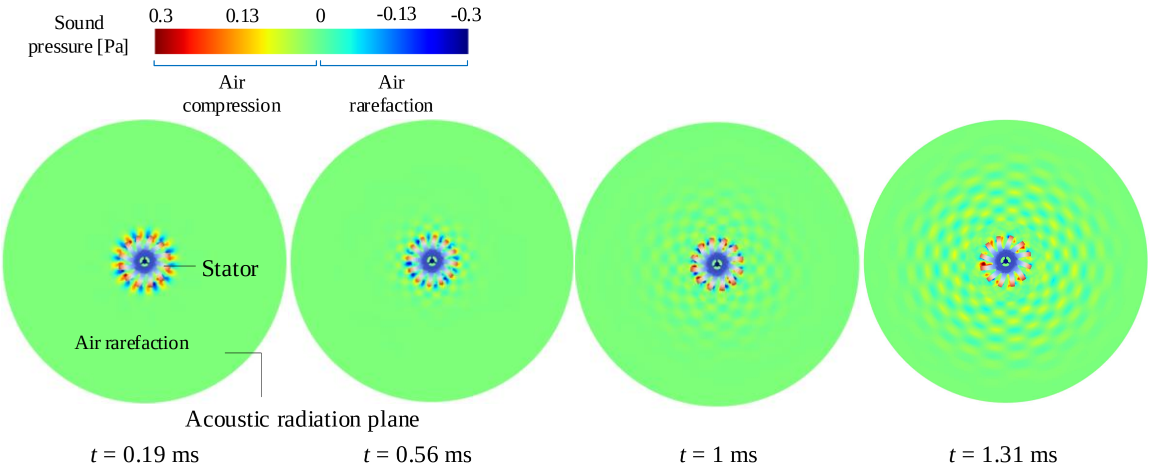

Fig. 5-18 Sound pressure map of the stator-shaft subassembly, 12/16 external-rotor SRM, at 400 RPM with a reference current of 75 A.

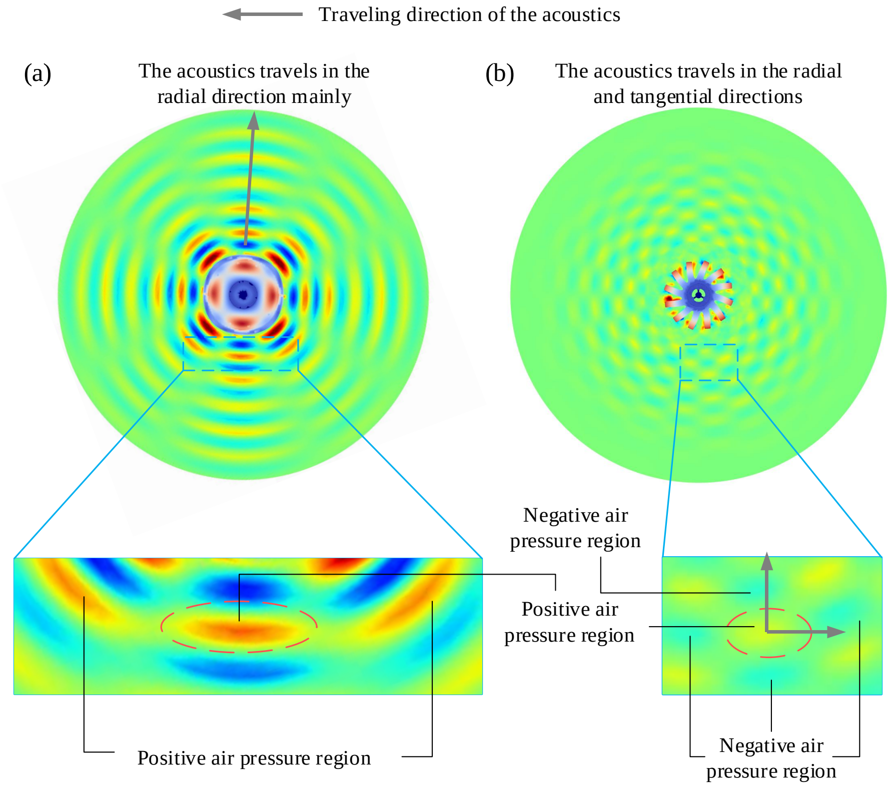

Fig. 5-19 Comparison between the sound pressure caused by the vibration of the stator and the rotor, (a) rotor, (b) stator.

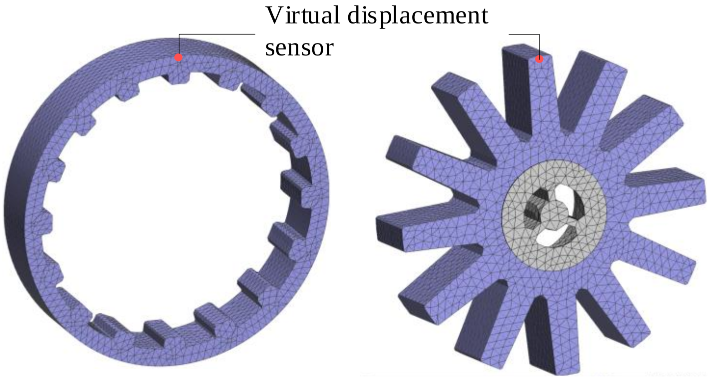

Fig. 5-20 Positions of the virtual displacement sensors.

In order to further compare the vibration behavior of the rotor and the stator, virtual displacement sensors are placed in the rotor and the stator. The captured displacements of the stator and the rotor are shown in Fig. 5-21. It can be seen that the rotor has a higher vibration magnitude than the stator. The stator and rotor displacement waveforms have many harmonic components. All these harmonics of the vibrations are sources of acoustic noise. However, since they have different radiation ratios and different forcing frequencies, the maximum SPL does not necessarily occur by the harmonic which has the largest amplitude.

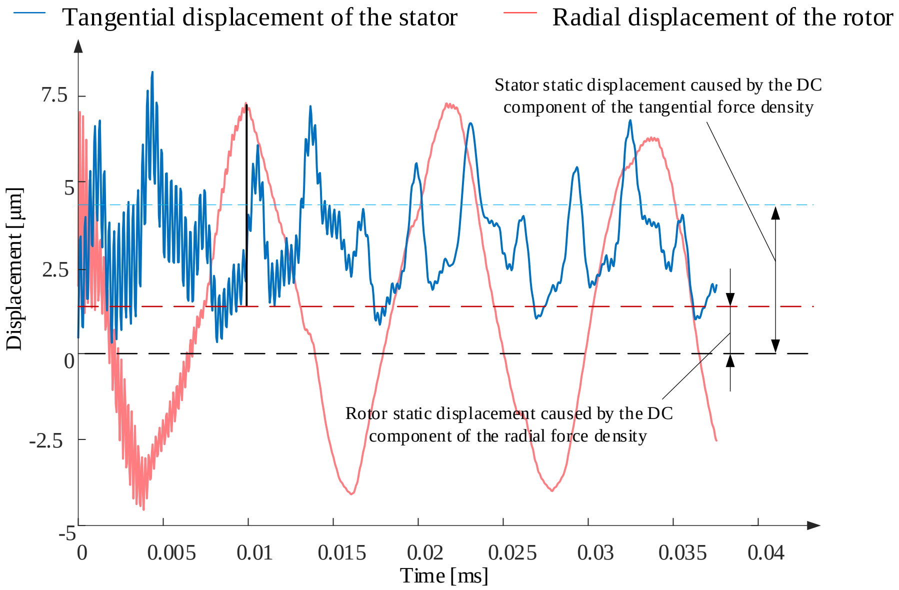

Fig. 5-21 Tangential displacement of the stator and the radial displacement of the rotor in the 12/16 external-rotor SRM, at 400 rpm with a reference phase current of 75 A.

Fig. 5.22 and Fig. 5.23 show the SPL of the stator and the rotor of the 12/16 ER SRM at 400 rpm with a reference current of 75 A. The excitations of the stator tangential vibration mode zero and four, and the rotor radial vibration mode zero and four are causing the acoustic noise in this 12/16 ER SRM. The maximum SPL radiated from the rotor-endcaps subassembly is higher than the max SPL radiated from stator-shaft subassembly. It can be concluded that for this 12/16 ER

SRM, which is designed with a thin rotor back iron and long stator poles, the acoustic noise caused by the radial vibration of the rotor dominates in the total acoustic noise of the motor.

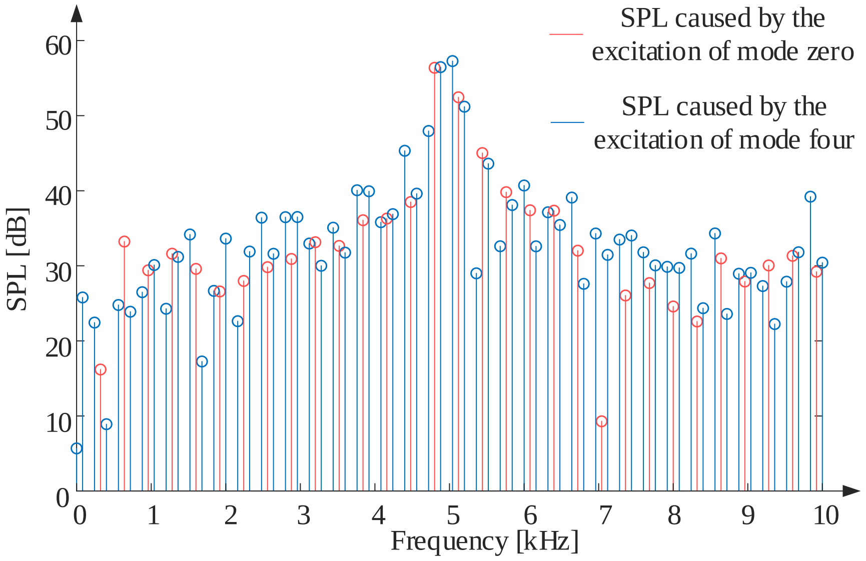

Fig. 5.22 Sound pressure level radiated from the rotor-shaft subassembly of the 12/16 external-rotor SRM, 400 rpm with a reference current of 75 A.

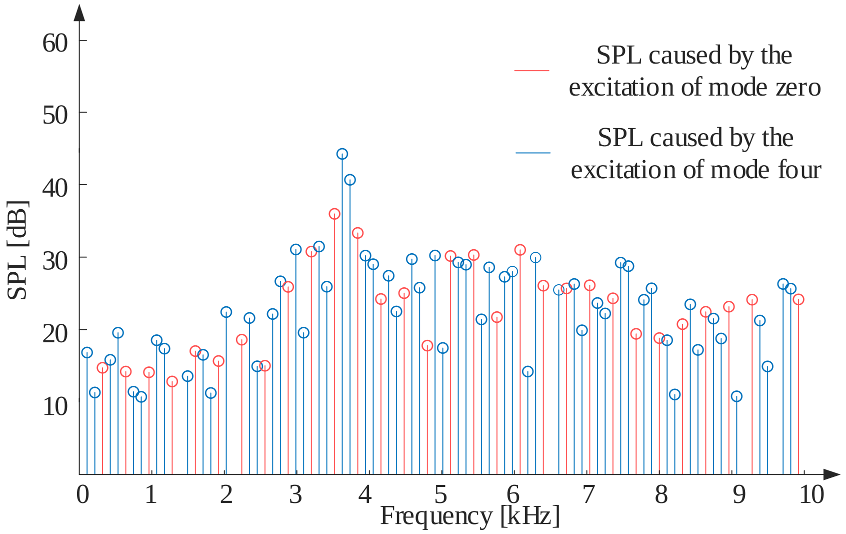

Fig. 5.23 Sound pressure level radiated from the stator-endcaps subassembly of the 12/16 external-rotor SRM, 400 rpm with a reference phase current of 75 A.

Fig. 5-24 shows the tested SPL of the 12/16 ER SRM at 400 rpm and with a reference current of 75 A. Many peaks of the SPL, which are caused by numerous harmonics in the stator tangential force density and the rotor radial force density, can be observed. There are also two SPL peaks appearing at 1280 Hz and 4480 Hz, which are caused simultaneously by the circumferential order of zero for the rotor radial force density harmonics and stator tangential force density harmonics. For the other SPL peaks, they are either caused by the stator tangential vibration or the rotor radial vibration.

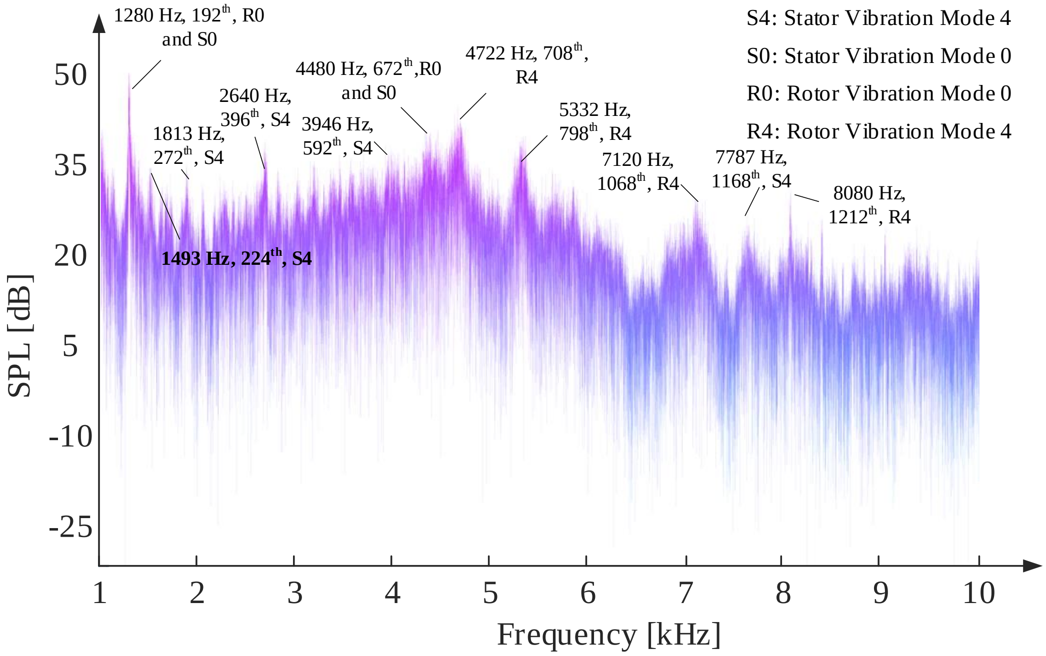

Fig. 5-24. Experimental results of the SPL in the 12/16 external-rotor SRM, 400 rpm, with a reference phase current of 75 A.

5.5 Conclusions

This chapter presents the considerations in the acoustic noise modeling and analysis of the external-rotor SRM stator and rotor. The harmonic components in the tangential force density of the stator and the radial force density of the rotor are analyzed and compared. The vibration modes, the vibration behavior, and the acoustic noise of the stator and the rotor are also compared. A 12/16 external-rotor SRM designed for direct-drive e-bike application is used for the modeling and analysis of vibration and acoustic noise. It is concluded that the acoustic noise caused by the radial vibration of the rotor is the primary source of the acoustic noise for the ER SRMs.

Table 5-4 Material properties of the stator and rotor cores in the 24/16 SRM.

Part	Stator	Rotor	Coils	Housing
Density [kg/m^3]	7268	7268	4908	2700
Young’s modulus [GPa]	176	176	12	68.9
Poisson’s ratio	0.285	0.285	0.3	0.33

Appendix

In the simulation of the natural frequency of the stator core, the subassembly of the stator, coils and the housings is taken into account in the simulation and the support of the subassembly is defined as the clamped-free, where one end of the subassembly is clamped and the other end of the assembly is free to vibrate. In the simulation of the natural frequencies of the rotor cores, the support in the simulation is defined in the inner surface of the rotor core (see Fig. 5-3(b1)). The material properties of the parts are shown in Table 5-4.

References

[1] B. Howey, “Non-coupled and mutually coupled switched reluctance machines for an e-bike traction application: pole configurations, design, and comparison,” Ph.D. Thesis, Department of Mechanical Engineering, McMaster University, Hamilton, Canada, 2018.

[2] J. Jiang and J. Liang, “Chapter 12: Fundamentals of waves and vibrations”, *Switched Reluctance Motor Drives: Fundamentals to Applications*, Boca Raton, FL, USA: CRC Press, ISBN: 9781138304598, Nov. 2018.

Chapter 6: A Novel Analytical Acoustic Modeling Approach to Simulate the Acoustics in 3D Domain

6.1 Introduction

As discussed in Section 2.4 of Chapter 2, for any vibration mode, it has the free deformation in the circumferential and axial direction, which can be described by the corresponding circumferential and axial orders. The effect of the circumferential vibration modes on the vibration and acoustic noise has been studied in Chapter 3 to Chapter 5. However, the effect of the axial vibration modes on the acoustic noise is not clear and not reported in the literature. This chapter presents a novel method to analytically simulate the vibration and acoustic noise in radial-flux switched reluctance motors in the 3D domain when the excitations of the high-axial-order vibration modes are considered. The input data for the analytical calculations include the forcing frequencies and the magnitudes of the radial force density harmonics, the modal properties (e.g. natural frequencies, mode shapes, and the modal damping ratios), and the radiation ratios. These parameters need to be in the 3D domain and they should be functions of the temporal, circumferential, and axial orders.

First, the method of obtaining the input data for the 3D analytical simulation is presented. Besides, the effect of the major motor dimensions on the natural frequencies of different circumferential and axial orders is analyzed. Then, an analytical model for calculating the 3D radiation ratio, which considers the effect of the boundary conditions on the two ends of the motor, is presented. After decomposing the 2D radial force density into its temporal and circumferential orders, the axial modifying factors for different axial orders are introduced to further decompose the radial force density harmonics into axial orders. The axial modifying factors are optimized by genetic algorithm (GA) based on different boundary conditions of the motor. Finally, the acoustic noise results from the numerical simulation and experiments in an 8/6 switched reluctance motor drive are used to validate the analytical method presented in this chapter.

6.2 Analytical Method for the Calculation of Acoustic Noise

6.2.1 Analytical Calculation Process

In the analytical calculation of acoustic noise, when the excitation of the high-axial-order vibration modes are considered, all the input data need to be in the three-dimensional format and they should be represented as functions of the temporal order, q, circumferential order, $circ$, and the axial order, ax. The block diagram of the 3D analytical calculation process is shown in Fig. 6-1. The input data include the forcing frequency, $\omega_{f\,(q,\,circ,\,ax)}$, the magnitude of the radial force harmonics $F_{\mathrm{r}(q,\,circ,\,ax)}$, the natural frequency, $\omega_{n\,(q,\,circ,\,ax)}$, the damping ratio, $\zeta_{(q,\,circ,}$

$_{ax)}$, and the radiation ratio, $\sigma_{(q,\ circ,\ ax)}$. The following sections will present how to obtain the 3D format for all the input data.

Obtaining the radial force magnitudes $F_{\mathrm{r}(q,\ circ,\ ax)}$ is one of the most important steps in the 3D acoustic noise modeling. In the conventional 2D analytical method, the radial force harmonics are used in the $F_{\mathrm{r}(q,\ circ)}$ format. $F_{\mathrm{r}(q,\ circ)}$ is usually obtained by decomposing the 2D radial force density $P_{\mathrm{r}(q,\ circ)}$ which varies with time and circumferential position. The radial force density waveform can be generated directly from 2D electromagnetic FEA simulation or by using a dynamic model of the motor that utilizes look-up tables obtained from the FEA model [3]. As it will be presented later in this chapter, if $P_{\mathrm{r}(q,\ circ,\ ax)}$ can be obtained from the 2D radial force density harmonics $P_{\mathrm{r}(q,\ circ)}$, the radial force harmonics $F_{\mathrm{r}(q,\ circ,\ ax)}$ can be calculated as: $F_{\mathrm{r}(q,\ circ,\ ax)} = \pi \times D \times L_{\mathrm{s}} \times P_{\mathrm{r}(q,\ circ,\ ax)}$, where D is the inner diameter of the stator and L_{s} is the stack length.

Then, the displacement $D_{(q,\ circ,\ ax)}$ and the sound power, $\Pi_{(q,\ circ,\ ax)}$, are calculated as:

$$D_{(q,circ,ax)} = \frac{F_{r(q,circ,ax)} / M}{\sqrt{(\omega_{n(q,circ,ax)}^2 - \omega_{f(q,circ,ax)}^2)^2 + 4\zeta_{(q,circ,ax)}^2 \omega_{f(q,circ,ax)}^2 \omega_{n(q,circ,ax)}^2}} \tag{6.1}$$

$$\Pi_{(q,circ,ax)} = \rho_0 c_0 \left(\frac{\omega_{(q,circ,ax)} D_{(q,circ,ax)}}{\sqrt{2}} \right)^2 \sigma_{(q,circ,ax)} A_s \tag{6.2}$$

where M is the mass, A_{s} is the area of the acoustic radiation surface, ρ_0 is the mass density of air, and c_0 is the speed of sound in air at the room temperature. The forcing frequency, ω_f is a function of only the temporal order, q. In Fig. 6-1 and equation (6.1), it is shown in the $\omega_{f\,(q,\,circ,\,ax)}$ format so that the matrices for all components of displacement calculation have the same dimensions. The forcing frequency can be calculated by $\omega_{f\,(q,\,circ,\,ax)} = 2\pi \times q \times f_{\mathrm{mech}} = 2\pi \times q \times n / 60$, where f_{mech} is the mechanical frequency in Hz and n is the motor speed in rpm. After the displacement, $D_{(q,\,circ,\,ax)}$, and sound power, $\Pi_{(q,\,circ,\,ax)}$, are obtained, the total sound power caused by the excitation of different axial and circumferential modes can be superimposed by using (6.3). Then, the sound power level $\mathrm{SWL}_{(q)}$ and the sound pressure level $\mathrm{SPL}_{(q)}$ as well as the A-weighted sound pressure level $\mathrm{SPLA}_{(f)}$ can be calculated as depicted in Fig. 6-1 [6].

$$\hat{\Pi}_{(q)} = \sum_{ax=1}^{ax\_\max} \sum_{circ=0}^{circ\_\max} \Pi_{(q,circ,ax)} \tag{6.3}$$

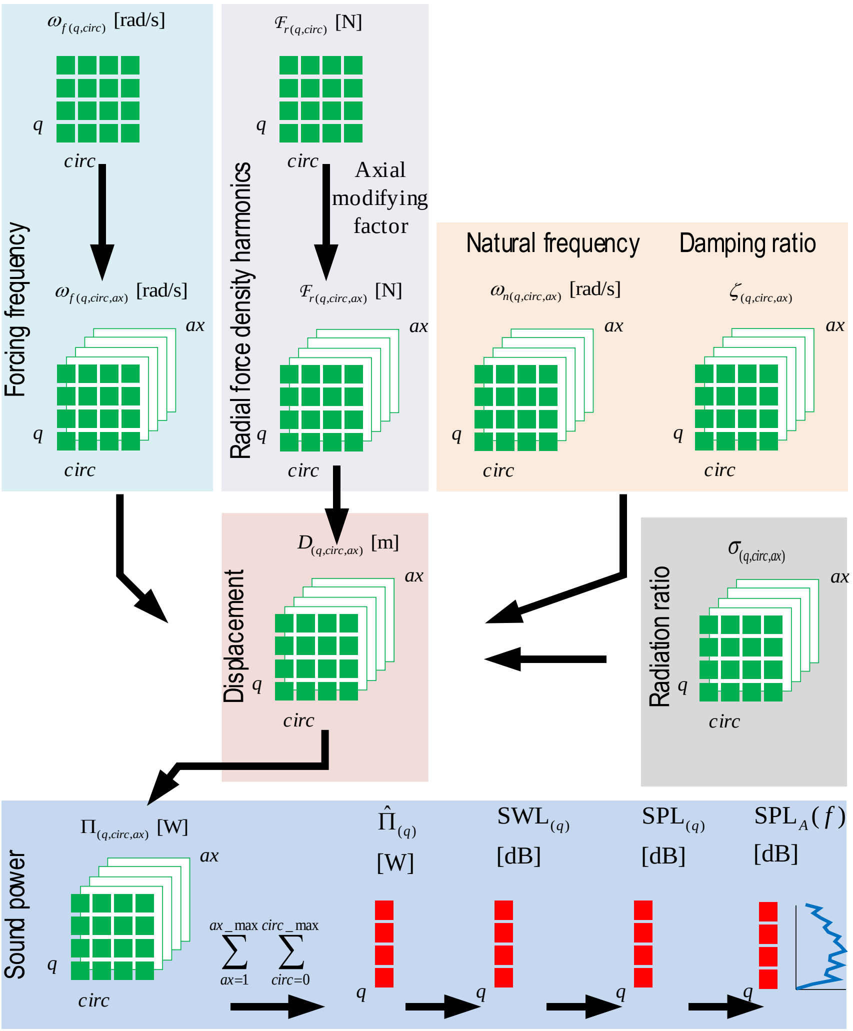

Fig. 6-1 The block diagram of the 3D analytical modeling of acoustic noise.

6.2.2. Vibration Modes

As shown in Fig. 6-1, the natural frequencies, ω_n and the modal damping ratios, ζ are parts of the inputs for the 3D analytical modeling. They are only functions of the circumferential and axial orders, but they are presented in $\omega_{\mathrm{n}\ (q,\ circ,\ ax)}$ and $\zeta_{(q,\ circ,\ ax)}$ format in Fig. 6-1 to obtain matrices in three dimensions.

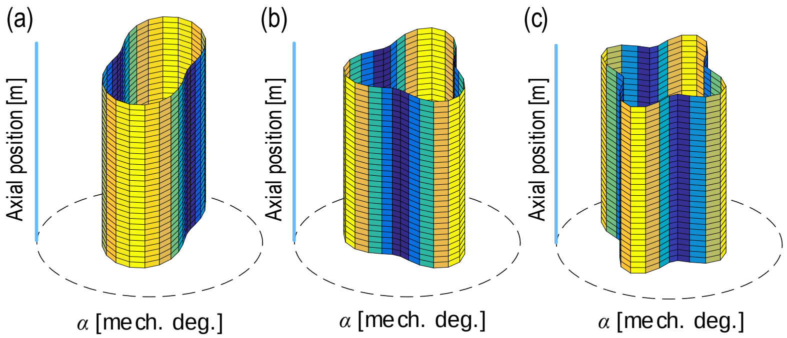

Fig. 6-2 Vibration modes of a cylindrical shell with different circumferential orders for *ax* =1, (a) *circ* =2, (b) *circ* = 3, (c) *circ* = 4 [6].

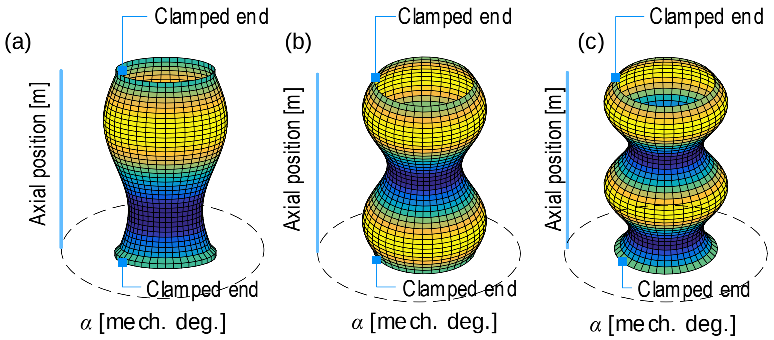

Fig. 6-3 Vibration modes of a cylindrical shell with different axial orders for *circ* = 0, (a) *ax* = 2, (c) *ax* = 3, (c) *ax* = 4.

As shown in Fig. 6-2 for a cylindrical shell, the stator of an SRM will have different vibration modes for different circumferential orders. As shown in Fig. 6-3, the same stator would have different mode shapes when considering the axial orders. For the 3D analytical modeling, the natural frequencies can be calculated numerically using the methods that were detailed in [4]. After the natural frequencies are calculated, the modal damping ratios of the vibration modes can be calculated using (6.4). Modal tests can also be used to obtain the natural frequencies and damping ratios.

$$\zeta_{(circ,ax,q)} = \zeta_{(circ,ax)} = \frac{1}{2\pi}\left(2.76\times10^{-5} f_{n(circ,ax)} + 0.062\right) \tag{6.4}$$

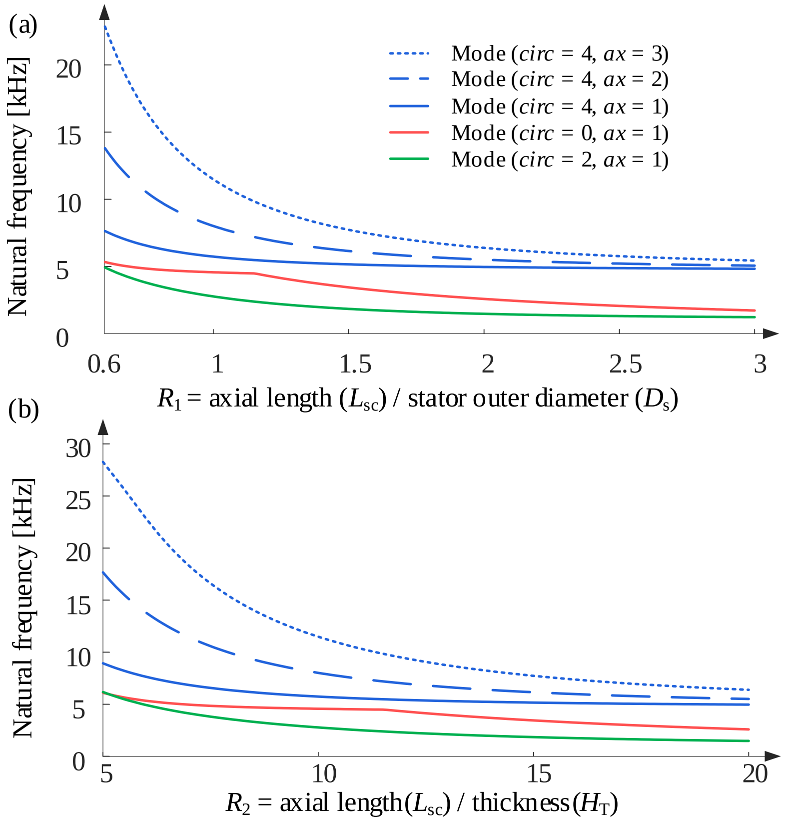

Fig. 6-4 Natural frequency of a cylindrical shell, (a) R_1 varies, (b) R_2 varies.

It should be noted that the motor dimensions, including the axial length, L_{sc} the total thickness, H_T (stator back iron plus the housing thickness), and the motor outer diameter, D_S (including the stator and the housing) have a significant effect on the natural frequencies. Fig. 6-4 shows how the natural frequencies of a cylindrical shell change with the ratios of motor axial length to the motor outer diameter ($R_1 = L_{sc} / D_s$) and also to the total thickness ($R_2 = L_{sc}/H_T$). As shown in Fig. 6-4(a), as the axial length increases, the natural frequencies of all the vibration modes tend to decrease due to the decrease in the modal stiffness. When

R_1 is small, the natural frequencies increase dramatically with the axial order for the same circumferential order. The difference gets smaller as R_1 increases. Fig. 6-4(b) shows how the natural frequencies change with R_2. In this case, the axial length and the outer diameter of the cylindrical shell are fixed and equal, and only the thickness varies. It can be observed that, for lower values of R_2, the natural frequencies of the vibration modes with high axial orders increase dramatically.

6.2.3. Radiation Ratios

The radiation ratio characterizes the radiation property of the acoustic noise from the vibrating motor structure. The boundary conditions of the motor structure at both ends affect not only the magnitude of the vibration but also the modal radiation ratios [22]. The modal radiation ratios are functions of the temporal order, *q*, circumferential order, *circ*, and axial order, *ax*. Assuming that the motor structure is modeled as a cylindrical shell with a certain type of boundary conditions at both ends, the modal radiation ratios are expressed as [22]:

$$\sigma_{(circ,q,ax)} = \frac{k_0}{\pi^2} \times \frac{1}{\int_0^L \left|\gamma_{ax}(x'/L)\right|^2 a dx} \int_{-k_0}^{k_0} \frac{\left|\Gamma_{ax}(k_z)\right|^2}{k_r^2 \left|\frac{\mathrm{d}H_{circ}{}^{(2)}(k_r a)}{\mathrm{d}(k_r a)}\right|^2} dk_z \tag{6.5}$$

where k_0 is the acoustic wavenumber and it is a function of the temporal order, q, mechanical frequency, f_{mech}, and the speed of sound in air, c_0: $k_0 = 2\pi q \times f_{\mathrm{mech}} / c_0$. L and a are the axial length and the outer radius of the cylindrical shell, respectively. x' denotes a position on the axial length of the cylindrical shell. k_z and k_r are two orthogonal components of k_0: $k_0^2 = k_z^2 + k_r^2$. $H_{circ}^{(2)}(k_r a)$ is the

Hankel function of the second kind. $\gamma_{\mathrm{ax}}(x)$ is the mode shape function of a beam with different boundary conditions, as shown in the second column in Table 6-1. The mode shape functions of a beam are used here because they provide a good approximation to describe the mode shapes of a cylindrical shell in the axial direction [23]. The mode shape function is calculated using β and σ_{ax} in the third and fourth columns in Table 6-1.

Table 6-1. Mode shape functions of a beam, with different axial order, *ax* [18]-[19].

Type of constraint	The function of mode shape, $\gamma_{\mathrm{ax}}(x)$	β_{ax}	σ_{ax}
Supported-supported	$\sin n\pi x$	N/A	N/A
Clamped-free	$\cosh(\beta_{ax}x)-\cos(\beta_{ax}x)$ $-\sigma_n\left[\sinh(\beta_{ax}x)-\sin(\beta_{ax}x)\right]$	$\frac{(2\times ax-1)\pi}{2}$	$\delta_{ax}=\frac{\sinh(\beta_{ax})-\sin(\beta_{ax})}{\cosh(\beta_{ax})+\cos(\beta_{ax})}$
Clamped-clamped	$\cosh(\beta_{ax}x)-\cos(\beta_{ax}x)$ $-\sigma_n\left[\sinh(\beta_{ax}x)-\sin(\beta_{ax}x)\right]$	$\frac{(2\times ax+1)\pi}{2}$	$\delta_{ax}=\frac{\cosh(\beta_{ax}L)-\cos(\beta_{ax}L)}{\sinh(\beta_{ax}L)-\sin(\beta_{ax}L)}$

* Note: *x* is the normalized axial position, $x = x'/L$.

In (6.5), the term $\Gamma_{\mathrm{ax}}(k_z)$ is used to transform the mode shape function $\gamma_{\mathrm{ax}}(x)$ to the domain of k_z by using Fourier transform, as shown in:

$$\Gamma_{ax}(k_z)=\int_0^1 \gamma_{ax}(x)e^{jk_z x}dx \tag{6.6}$$

where *j* represents the imaginary unit. If both ends of the SRM are supported-supported (S-S), then (6.5) can be expressed explicitly as in (6.7). Equations (6.5) and (6.7) can be solved by using numerical integration to calculate the radiation ratio waveforms as a function of circumferential and axial orders for different temporal orders. Fig. 6-5 shows the radiation ratios of a cylindrical shell for different boundary conditions and axial orders.

$$\sigma_{(circ,q,ax)} = \int_{-k_0}^{k_0} \frac{2k_0 l}{\pi^2 a k_r^2 \left| \dfrac{\mathrm{d}H_{circ}{}^{(2)}(k_r a)}{\mathrm{d}(k_r a)} \right|^2} \times \left[\frac{ax \cdot \pi / l}{k_z + ax \cdot \pi / l} \right]^2 \frac{\sin^2[(k_z - ax \cdot \pi / l) l / 2]}{[(k_z - ax \cdot \pi / l) l / 2]^2} \mathrm{d}k_z \quad (6.7)$$

Fig. 6-5(a) shows the effect of S-S and clamped-clamped (C-C) boundary conditions on the radiation ratio of a cylindrical shell when the axial order is one. It can be seen that the radiation ratio of S-S is slightly larger than that of the C-C for the same circumferential and temporal orders. This is because the acoustic radiation at two ends is constrained for the C-C boundary condition. The radiation ratios both for C-C and S-S tend to approach unity as the temporal order increases. Fig. 6-5(b) compares the radiation ratios of different axial orders when the motor has C-C boundary condition. The peak value of the radiation ratio with *ax* = 2 is larger than that with *ax* = 1 for the same circumferential order. In the low-frequency range, the radiation ratio with the first axial order is higher than the radiation ratio with the second axial order.

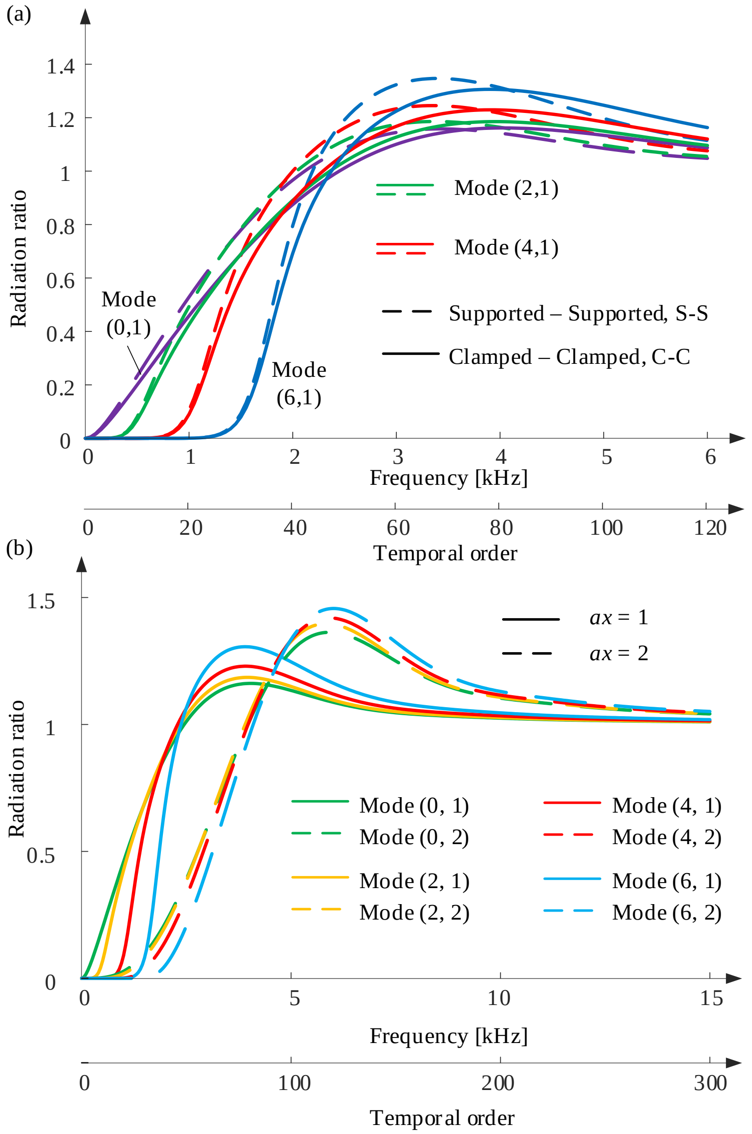

Fig. 6-5 Comparison of radiation ratios of a cylindrical shell at 3000 rpm when the axial length is 90 mm and the outer radius is 170 mm, (a) comparison of S-S and C-C, (b) C-C for different axial orders, *ax* = 1 and *ax* =2.

6.3 Decomposing the Radial Force Density into Circumferential, Temporal, and Axial Orders

6.3.1. Vibration Generation Mechanism

As it was shown in the block diagram for the 3D analytical acoustic noise modeling in Fig. 6-1, the electromagnetic forces need to be decomposed into harmonic components with a circumferential order, *circ*, temporal order, *q*, and the axial order, *ax*.

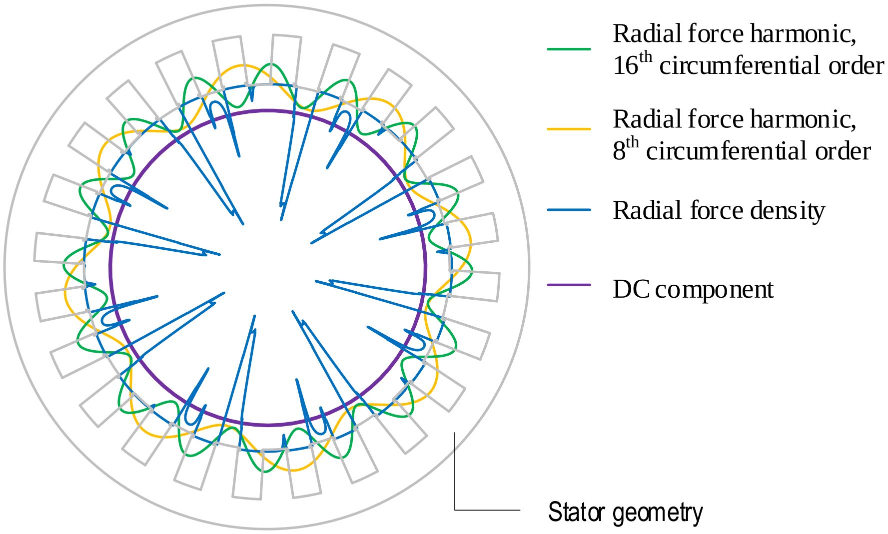

Fig. 6-6 1D decomposition of the radial force density into harmonics with different circumferential orders in the polar coordinate system.

In this section, we will first briefly discuss the relationship between the circumferential orders of the radial force density and the vibration modes of the motor structure, which creates the basis for the calculation of the axial orders. If 1D FFT is applied to the radial force density, which was extracted from the FEA model at a certain time step, the harmonics with different circumferential orders can be obtained. The results are shown in the polar coordinate system in Fig. 6-6. It can be observed that the 8^{th} and 16^{th} circumferential order of the radial force density harmonics have larger magnitudes. The shapes of these two harmonics are the same as the 8th and 16th circumferential vibration modes.

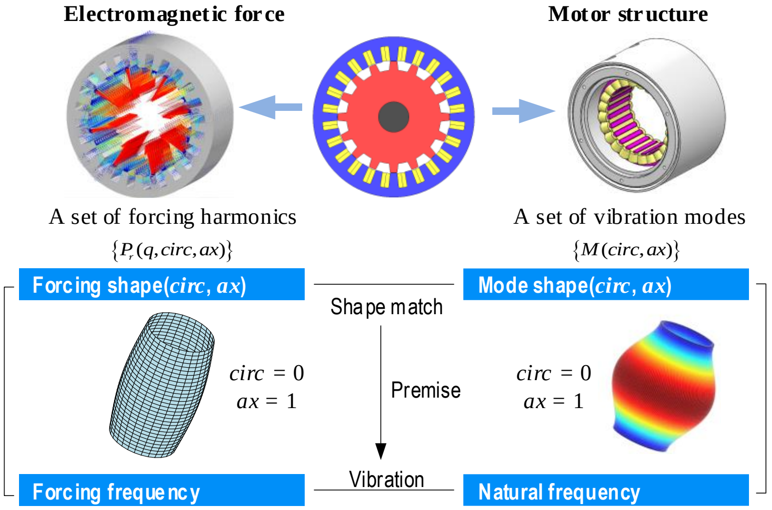

Fig. 6-7. Vibration generation mechanism [6].

Therefore, vibration happens when the shape of the radial force density harmonic match with the shape of the vibration modes for both circumferential and axial orders, provided that the forcing frequency of the harmonic is not zero. This mechanism for vibration generation is illustrated in Fig. 6-7. For the decomposition of the radial force density into its axial orders, we will utilize the same mechanism: the shape of the radial force density harmonics in the axial direction should be the same as the axial vibration modes.

6.3.2. Axial orders and Axial Modifying Factors

In this section, the axial modifying factor is introduced to model the excitation of the axial-order vibration modes. The axial modifying factor, A_{ax}

decomposes the radial force density waveform into the axial orders as shown in Fig. 6-8. It can be regarded as a weighting factor for different axial orders.

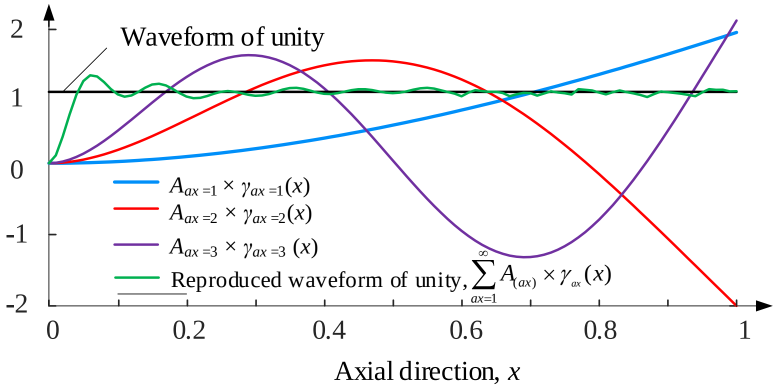

Fig. 6-8 The waveform of unity reproduced by using the axial modifying factors when the motor has C-F boundary conditions on its two ends.

When the radial force density is extracted from 2D FEA as illustrated in Fig. 6-9, it is considered constant along the axial direction. This is represented with the waveform of unity in Fig. 6-8. As a weighting factor, the axial modifying factor changes the contribution of the radial force density of different axial orders along the axial direction. Therefore, at each axial position, when the radial force densities for each axial order are summed, the reproduced waveform replicates the waveform of unity as shown in Fig. 6-8. In order to obtain A_{ax}, an optimization problem is formulated with the objective function:

$$\min \left(\int_0^1 [\sum_{ax=1}^{\infty} A_{ax} \times \gamma_{ax}(x) - 1]\, dx\right) \tag{6.8}$$

where x is the normalized axial position and can be calculated by x'/L. Here, x' and L are the axial position and total axial length of the motor, respectively. In the objective function, the axial modifying factor is multiplied by the mode shape functions, $\gamma_{\mathrm{ax}}(x)$ from Table 6-1. This is because the vibration mode shapes in the axial direction depend on the boundary conditions. This is illustrated in Fig. 6-10 with the vibration modes of a cylindrical shell for different constraints at both ends. It can be noticed that the boundary conditions greatly affect the mode shapes in the axial direction, which lead to different vibration behavior. The optimization problem is solved using Genetic Algorithm (GA) to define A_{ax} for different axial orders.

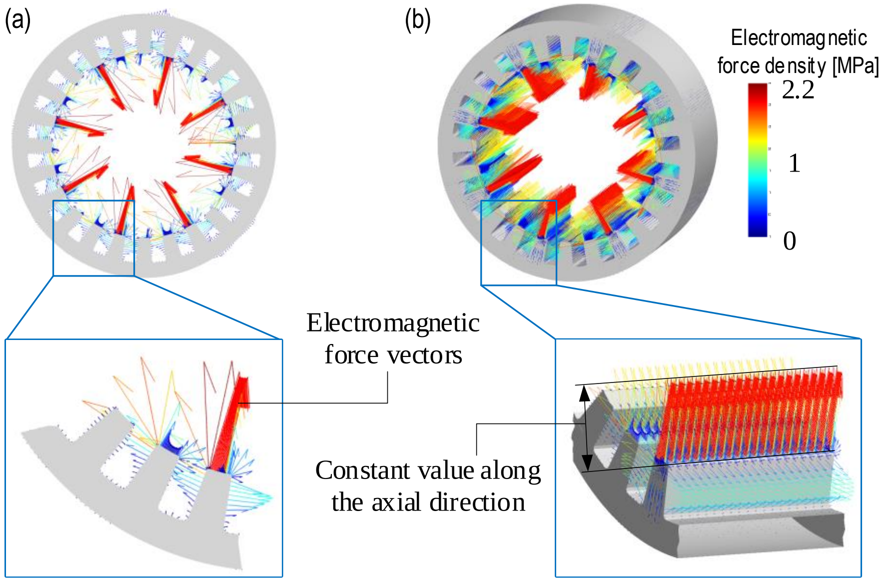

Fig. 6-9 Electromagnetic force density of a 24/16 SRM stator at 2000 rpm, t = 0.8 ms, (a) 2D, (b) 3D.

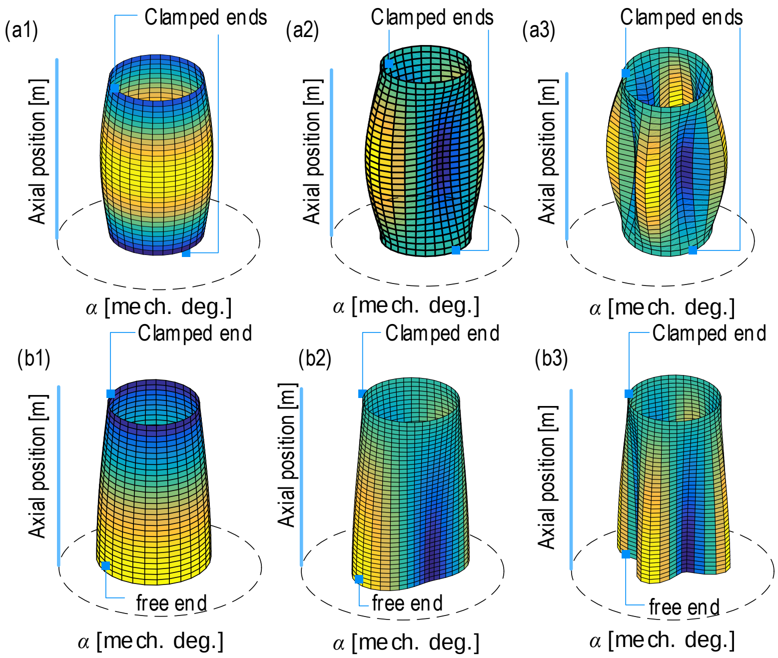

Fig. 6-10 Vibration modes of a cylindrical shell with different constraints on two ends, (a1) to (a3) clamped-clamped (C-C), (b1) to (b3) clamped-free (C-F), (a1) and (b1) are for *circ* = 0, (a2) and (b2) are for *circ* = 2, (a3) and (b3) are for *circ* = 4.

Table 6-2 and Fig. 6-11 show the optimized values of A_{ax} for S-S, C-F, and C-C boundary conditions on the two ends of the motor. For the cylindrical shell with S-S and C-C, A_{ax} is zero when the axial order is an even number. This is because the axial mode shape functions $\gamma_{\mathrm{ax}}(x)$ for C-C and S-S are similar to sinusoidal functions [24]. Based on the Fourier's theorem, a square wave can be decomposed into sinusoidal waves with only odd-integer orders. Besides, the axial modifying factor of the odd axial order for S-S is higher than that of C-C. This is because there are more constraints applied to the two ends of the motor in the C-C boundary condition.

Table 6-2. Axial modifying factors for different boundary conditions.

	Axial order, *ax*								
	1	**2**	**3**	**4**	**5**	**6**	**7**	**8**	**9**
S-S	1	0	0.42	0	0.25	0	0.18	0	0.14
C-C	0.83	0.01	0.36	0	0.23	0	0.17	0	0.13
C-F	0.91	0.47	0.25	0.18	0.14	0.12	0.10	0.08	0.08

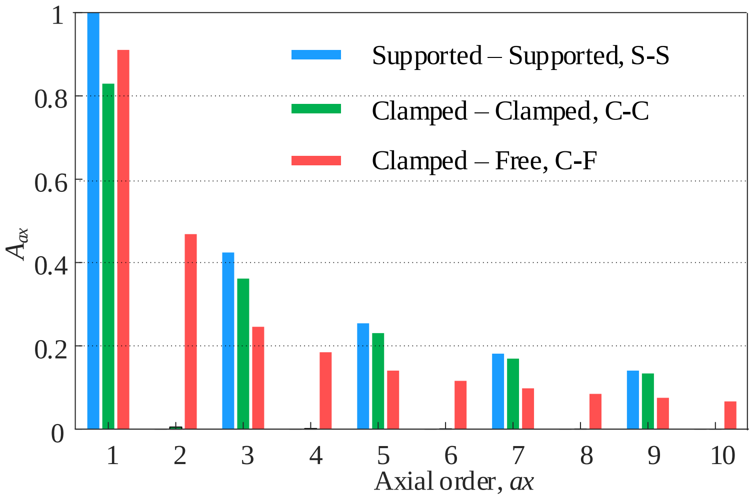

Fig. 6-11. Comparison of axial modifying factors for different boundary conditions.

When the axial order is one in the S-S boundary condition, the corresponding axial modifying factor $A_{\mathrm{ax}\,=\,1} = 1$. This is the case in the conventional 2D analytical method, where the axial modifying factor for the first axial order is equal to one and the excitations of all the high-axial-order vibration modes are ignored. For all the three types of boundary conditions, $A_{\mathrm{ax}\,=\,1}$ has the largest value and the axial modifying factors decrease as the axial order increases. An SRM is often supported with C-C or C-F boundary conditions and, thus, the motor designers need to select the proper axial modifying factors in the analytical acoustic noise simulation based on the actual constraints on the two ends of the motor.

The axial modifying factors for the C-F boundary condition show a different pattern compared with the C-C and S-S. A_{ax} is nonzero when the axial order is an even number for the C-F boundary condition. This is due to the different mode shape functions for the C-F boundary condition. Because of the effect of the free end, the mode shapes in the C-F are different from that of the sinusoidal waveforms, as shown in Fig. 6-8.

Fig. 6-8 also shows the reproduced waveform of unity for C-F by using the optimized values of A_{ax} for the first ten axial orders. It can be seen that there is a good match between the reproduced waveform and the waveform of unity. It should be noted that the optimized axial modifying factors are not functions of the motor axial length and can be applied to other radial-flux SRMs. This is because the normalized axial position x is used in the optimization objective in (6.8) and in the expression of the axial mode shape function $\gamma_{\mathrm{ax}}(x)$ in Table 6-1.

6.3.2. Applying the Axial Modifying Factor

This section discusses how the axial modifying factors can be used in the decomposition of the radial force density harmonics along the axial direction. Fig. 6-9 depicted how the electromagnetic force density is extracted from the FEA model of a 24/16 SRM. First, by applying 2D FFT to the time-varying and circumferential-position-varying radial force density waveform obtained from 2D electromagnetic FEA simulation, the harmonics associated with circumferential and temporal orders are calculated as:

$$P_{r(t,\alpha)} = \sum_{u=-\infty}^{+\infty} \sum_{v=-\infty}^{+\infty} P_{r(u,v)} \times \cos(2\pi f_{mech} ut + v\alpha + \phi_{(u,v)}) \tag{6.9}$$

where $P_{r(u,\ v)}$ is the magnitude of the harmonic, $\Phi_{(u,v)}$ is the phase angle of the harmonic, α is the circumferential position, and t represents time. Fig. 6-12 shows an example of the 2D radial force density harmonics on a 24/16 SRM stator.

Then, the axial modifying factors for different axial orders are used to further decompose the harmonics into their axial orders. The flow diagram in Fig. 6-13 describes this process. Based on the Fourier's theorem, the decomposition of the multi-dimensional data into harmonics along different directions can be conducted separately in each direction [28]. Therefore, the radial force density harmonics associated with the circumferential, temporal, and axial orders can be expressed as

$$P_{r(t,\alpha,x)} = \sum_{u=-\infty}^{+\infty} \sum_{v=-\infty}^{+\infty} \sum_{ax=1}^{\infty} A_{ax} \times \gamma_{ax} \times P_{r(u,v)} \times \cos(2\pi f_{mech} ut + v \times \alpha + \phi_{(u,v)}) \tag{6.10}$$

In (6.10), $A_{ax} \times \gamma_{ax}$ is used to decompose the radial force density into the axial orders. For the motor with S-S boundary condition, (6.10) can be expressed as in (11) by using the γ_{ax} expression in Table 6-1.

$$P_{r(t,\alpha,x)} = \sum_{u=-\infty}^{+\infty} \sum_{v=-\infty}^{+\infty} \sum_{ax=1}^{\infty} A_{ax} \times P_{r(u,v)} \times \sin(n\pi x + \phi) \times \cos(2\pi f_{mech} ut + v \times \alpha + \phi_{(u,v)}) . \tag{6.11}$$

In (6.11), $A_{ax} \times P_{r(u,v)}$ is the magnitude of the radial force density harmonic with temporal order, u, circumferential order, v, and axial order, ax.

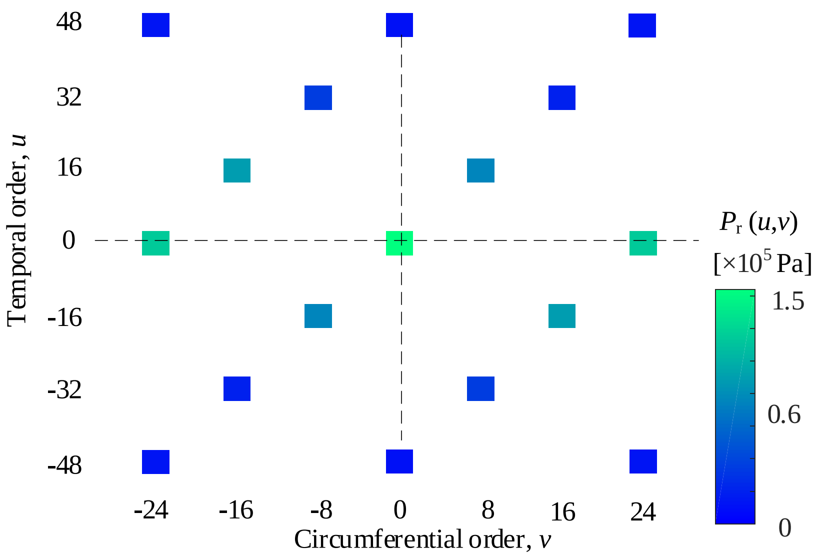

Fig. 6-12. 2D radial force density harmonics of a 24/16 SRM stator when the rotor rotates in the counter clockwise direction.

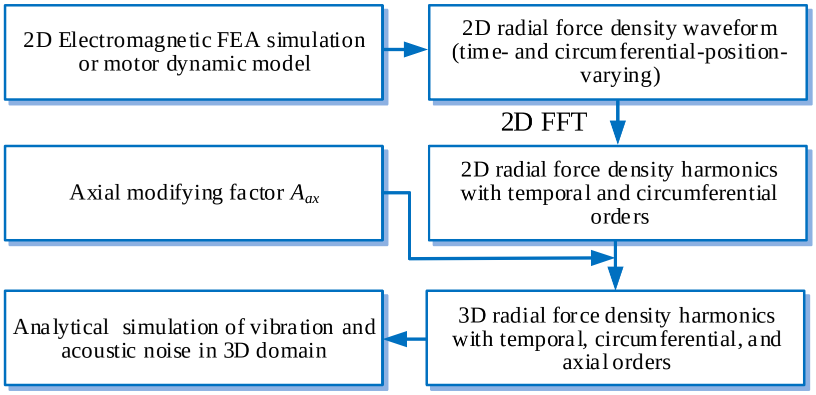

Fig. 6-13 Obtaining the 3D the radial force density harmonics with temporal, circumferential, and axial orders.

6.4 Results and Discussions

The proposed method is applied to simulate the acoustic noise of an 8/6 SRM considering the excitation of the high-axial-order vibration modes. It will be validated with numerical simulations and experiments for the same motor. The phase currents shown in Fig. 6-14 will be used in the analysis, where the motor operates at 2048 rpm and 5 Nm. The electromagnetic forces are obtained from the FEA simulations in JMAG, and they will be utilized for the calculation of the acoustic noise in the numerical simulations and in the proposed analytical model.

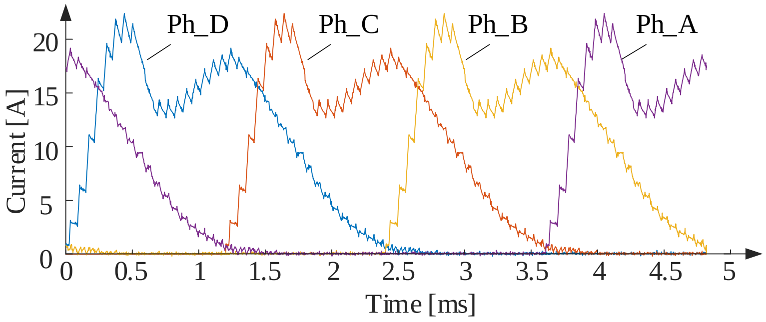

Fig. 6-14 The phase currents of the 8/6 SRM in the electromagnetic FEA simulation and motor tests at 2048 rpm with 5 Nm.

6.4.1. Natural Frequencies and Modal Damping Ratios for the Analytical and Numerical Simulation

As stated in Section 6.3, the natural frequencies of the dominant vibration modes should be calculated for acoustic noise analysis. For the proposed method, the natural frequencies of higher-order axial modes should also be considered.

First, the natural frequencies obtained from the numerical simulation and the hammer test will be compared. For the 8/6 SRM, the dominant vibration mode is *circ* = 2, since this motor has two poles per phase [21]. Fig. 6-15 shows the vibration modes (2, 1) and (2, 2) obtained from the numerical simulation in ACTRAN [6, 9, 12]. The first number shows the circumferential mode, *circ*, and the second number shows the axial mode, *ax*. The natural frequencies of these two vibration modes appear in the low-frequency range.

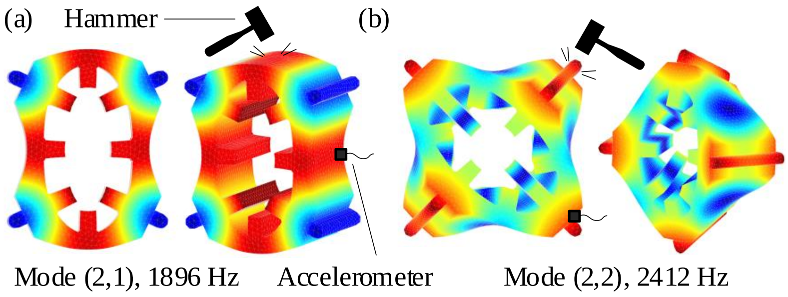

Fig. 6-15 Mode shapes and the natural frequencies in the 8/6 SRM, numerical simulation, (a) vibration mode (2, 1), (b) vibration mode (2, 2) [20]-[21].

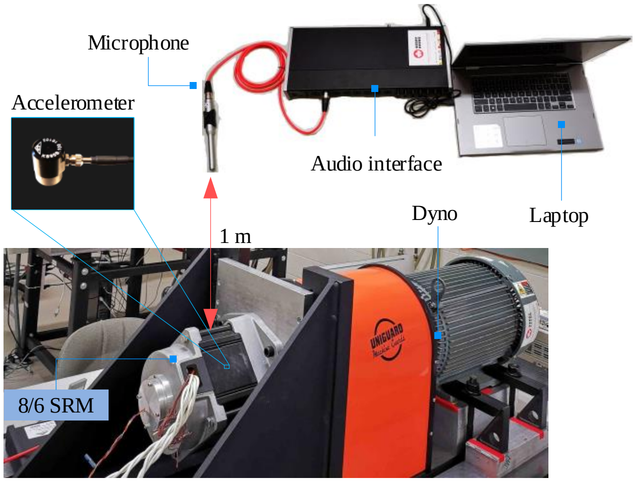

Fig. 6-16 Setup for the hammer test and acoustic noise measurement of an 8/6 SRM.

Fig. 6-16 shows the setup for the hammer test and the acoustic noise measurement of the 8/6 SRM. Different vibration modes of the stator can be excited by hammering different locations of the stator. The hammering locations for exciting the vibration modes (2, 1) and (2, 2) are shown in Fig. 6-15(a) and (b), respectively. The time-domain damped oscillation and the frequency-domain response from the hammer tests for vibration modes (2,1) and (2,2) are shown in Fig. 6-17 and Fig. 6-18, respectively.

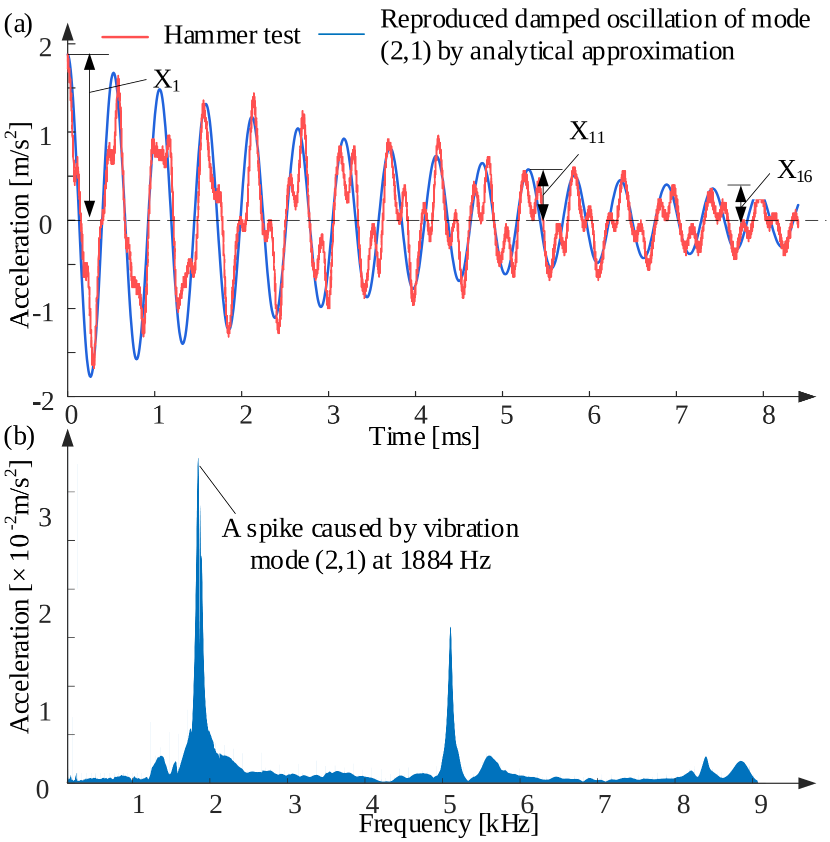

Fig. 6-17. Hammer test results for mode (2,1): (a) damped oscillation in time domain, (2) response in the frequency domain.

As shown in Fig. 6-17(b) and Fig. 6-18(b), the experimental natural frequencies of the vibration modes (2, 1) and (2, 2) appear at 1884 Hz and 2435 Hz, respectively. These results are very close to the numerically simulated natural frequencies at 1896 Hz and 2412 Hz (see Fig. 6-15).

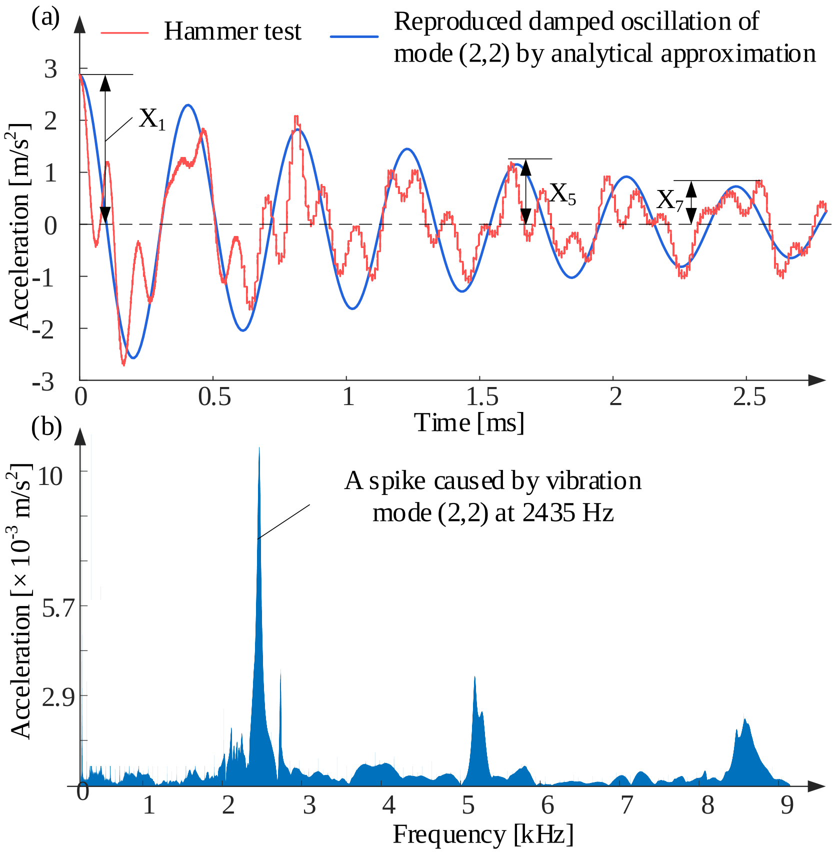

Fig. 6-18. Hammer test results for mode (2,2): (a) damped oscillation in time domain, (2) response in the frequency domain.

In Fig. 6-17(b) and Fig. 6-18(b), the spikes caused by the vibration modes (2, 1) and (2, 2) have the lowest natural frequencies compared to the other major spikes in their corresponding responses from the hammer tests. This means that, for both cases, the time-domain damped oscillation of the lowest-natural-frequency vibration modes has the lowest decay rate in the time-domain response as compared to other high-natural-frequency vibration modes [20]. Therefore, the time-domain damped oscillations of the high-natural-frequency vibration modes would decay to almost zero after several cycles, and the response of the lowest-natural-frequency vibration mode would dominate in the remaining oscillations cycles. This allows us to estimate the modal damping ratios, ζ, of mode (2, 1) and (2, 2) from their corresponding time-domain damped oscillations (see Fig. 6-17(a) and Fig. 6-18(a)) [25]-[27]:

$$\zeta = \frac{1}{2\pi(n-m)}\ln(\frac{X_m}{X_n}) \tag{6.12}$$

where X_m and X_n are the magnitudes of the m^{th} and n^{th} oscillation in Fig. 6-17(a) and Fig. 6-18(a), respectively. These numbers approximate the cycles where high-natural-frequency vibration modes have decayed to zero. For mode (2, 1) $m = 11$ and $n = 16$, and for mode (2, 2) $m = 5$ and $n = 7$ are used in the calculations of the corresponding modal damping ratios.

The modal damping ratios for the vibration modes (2, 1) and (2, 2) can be calculated as 0.0188 and 0.0365, respectively. In order to validate these damping ratios, the reproduced time-domain damped oscillations caused only by vibration mode (2,1) or (2,2) can be calculated by [20]:

$$a(t) = X_1 \times e^{-2\pi\zeta ft}(\cos(\sqrt{1-\zeta^2}\,2\pi f \times t) - \frac{\zeta}{\sqrt{1-\zeta^2}}\sin(\sqrt{1-\zeta^2}\,2\pi f \times t)) \tag{6.13}$$

where f is the natural frequency of the vibration mode (2,1) or (2,2) in [Hz], t is the time in seconds, and ζ is the damping ratio. Fig. 6-17(a) and Fig. 6-18(a) show the reproduced damped oscillation from (13) in addition to the damped oscillation obtained from the hammer test. It can be observed that there is a good match between these waveforms. The modal damping ratios of the vibration modes (2, 1) and (2, 2) obtained from the modal tests will be used in the analytical and numerical simulations.

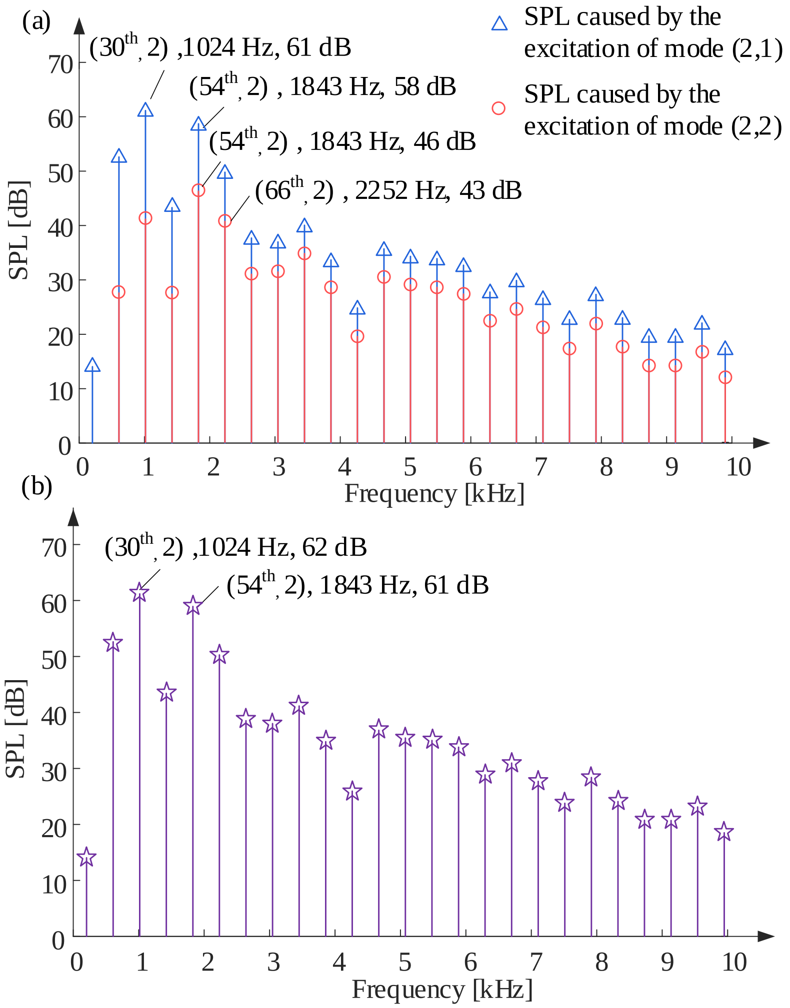

Fig. 6-19 Analytical results of the SPL in an 8/6 SRM at 2048 rpm with 5 Nm, (a) the SPL caused by the individual excitation of vibration mode (2, 1) and (2,2), (b) the summed SPL.

6.4.2. Analytical Simulation Results

At this point, the calculation of all the inputs for the three-dimensional analytical calculation of the SPL (see Fig. 6-1) has been presented. By utilizing these inputs, we will calculate the SPL in this section using the proposed analytical method, which takes the axial modifying factor (hence the axial orders) and vibration behavior of the dominant axial orders into account.

The analytical results of the SPL in the 8/6 SRM are shown in Fig. 6-19. The symbol "∆" in Fig. 6-19(a) shows the SPL when only the excitation of the vibration mode (2,1) is considered in the analytical acoustic noise analysis. The maximum SPL appears at 1024 Hz, which is caused by the radial force harmonic (30th, 2) with a temporal order 30 and circumferential order 2. In the same figure, the symbol "○" shows the SPL when only the excitation of the vibration mode (2, 2) is considered. The max SPL is 46 dB and appears at 1843 Hz. It should be noted that the SPL caused by the excitation of vibration mode (2, 1) and (2, 2) appear at the same frequency points. This is because the SPL is generated by the radial force density harmonics, $P_{r(u,\ v,\ ax)}$, with the same temporal and circumferential orders, but with different axial order. Fig. 6-19(b) shows the summed SPL when the vibration mode (2, 1) and (2, 2) are both excited. The summed SPL at a certain frequency point, *f*, can be calculated as:

$$\mathrm{SPL}_{sum(f)} = 20\log_{10}[10^{\frac{SPL_1(f)}{20}} + 10^{\frac{SPL_2(f)}{20}}] \tag{6.14}$$

where the SPL caused by the individual excitation of vibration mode (2, 1), $\mathrm{SPL}_1(f)$, and the SPL caused by the individual excitation of vibration mode (2, 2), $\mathrm{SPL}_2(f)$, are treated as correlated signals because they appear at the same frequency and the phase difference between them is constant [29]. In Fig. 6-19(b), the maximum total SPL also appears at 1024 Hz with a value of 62 dB. The summed SPL is mainly affected by the excitation of vibration mode (2, 1).

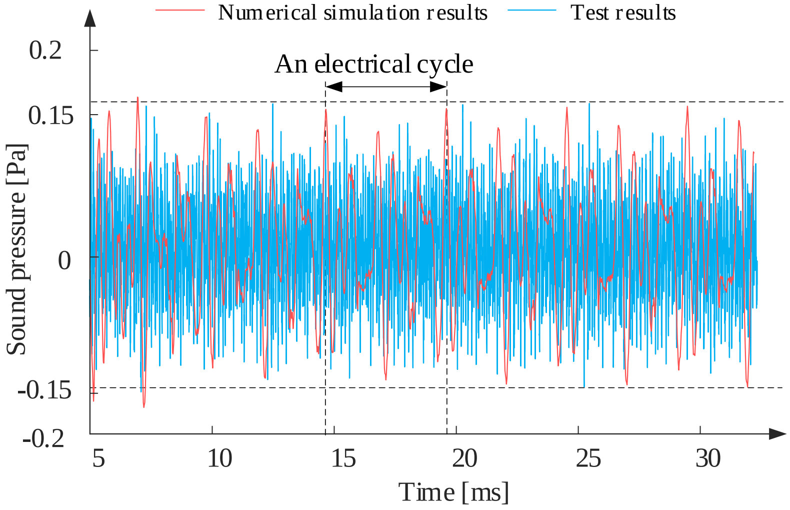

Fig. 6-20 The sound pressure in the 8/6 SRM at 2048 rpm, 5 Nm.

6.4.3. Numerical Simulation Results and Experimental Validation

In this section, the summed SPL obtained by the proposed analytical method is validated by the results from the numerical simulation and motor tests. The time-domain numerical simulation of the acoustic noise is performed in ACTRAN. The details of the numerical acoustic noise modeling are presented in [4]-[6]. The sound pressure obtained by the numerical simulation and the motor test is shown in Fig. 6-20. Both sound pressure waveforms have similar amplitudes.

The SPLs of the numerical simulation and the experimental results are shown in Fig. 6-21 and Fig. 6-22, respectively, which show a good match with respect to the acoustic noise calculated by the analytical method presented in this chapter. In both Fig. 6-21 and Fig. 6-22, there is a significant SPL peak appearing at 1843 Hz. This is because the forcing frequency of the 54th harmonic at 1843 Hz is very close to the natural frequency of the vibration mode (2, 1), 1896 Hz. Also, in both Fig. 6-21 and Fig. 6-22, there are two SPL peaks at 2252 Hz and 2662 Hz, which are caused by the 66th and the 78th harmonic, respectively. The frequencies of these two SPL peaks are close to the natural frequency of vibration mode (2, 2), 2412 Hz. However, the SPL values of these two peaks are smaller than the SPL at 1843 Hz. This is due to the axial modifying factors presented in Table 6-2. As mentioned previously, the axial modifying factors can be seen as weighting factors, which show the contribution of the radial force density harmonics of different axial orders along the axial direction. For the 8/6 SRM with C-F boundary condition, the axial modifying factor for *ax* = 2 is smaller than that for *ax* = 1. The results confirm that after introducing the axial vibration mode in the simulation, the vibration and acoustic noise behavior of the SRM can be better understood and more accurate simulation results can be obtained.

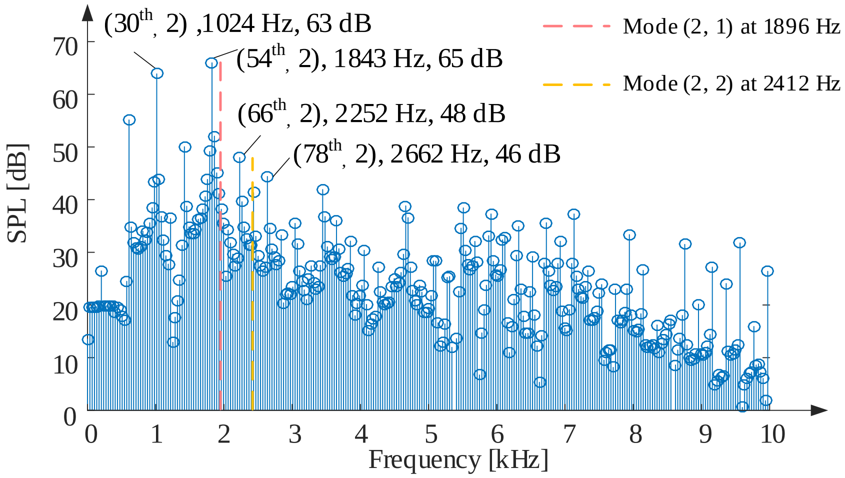

Fig. 6-21 Numerical results of the SPL in the 8/6 SRM, 2048 rpm, 5 Nm.

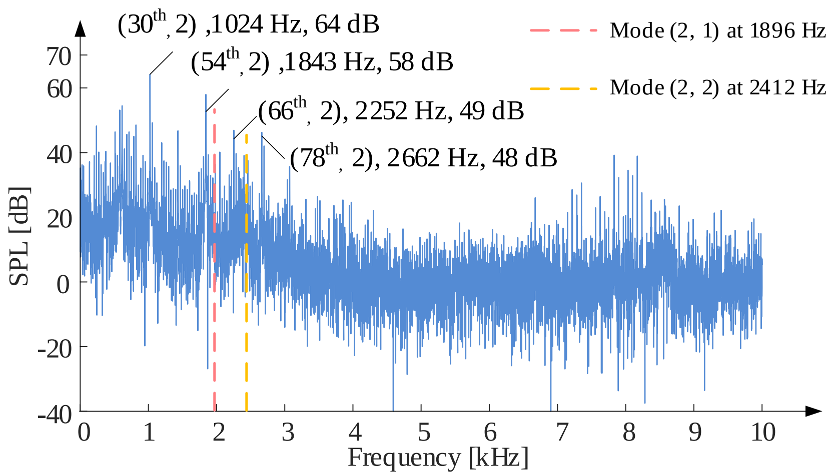

Fig. 6-22. Experimental results of the SPL in the 8/6 SRM at 2048 rpm, 5 Nm.

6.5 Conclusions

This chapter presents a novel analytical method to simulate the vibration and acoustic noise in the 3D domain when the excitation of the high-axial-order vibration modes of the motor structure is considered. Methods of obtaining the input data for the 3D analytical simulation are presented. An analytical model for the calculation of the radiation ratio in the 3D domain, which considers the effect of the boundary conditions on the two ends of the motor, is presented. Results show that the boundary conditions of the SRM affect the radiation ratio. When the temporal order is small, the radiation ratio with a low axial order has a higher magnitude compared with the radiation ratio with a high axial order. After decomposing the 2D radial force density into 2D harmonics with temporal and circumferential orders, the axial modifying factors for different axial orders are introduced to further decompose the radial force density harmonics into the axial orders. The axial modifying factors are optimized by genetic algorithm (GA) based on different boundary conditions on the two ends of the motor. The acoustic noise results from the numerical simulation and motor tests in an 8/6 SRM are used to validate the proposed 3D analytical method.

References

[1] B. Bilgin and A. Emadi, “Electric motor industry and switched reluctance machines," in *Switched Reluctance Motor Drives: Fundamentals to Applications*, Boca Raton, FL, USA: CRC Press, ISBN: 978-1138304598, Nov. 2018.

[2] B. Bilgin and A. Sathyan, “Fundamentals of electric machines,” *Advanced electric drive vehicles*, Boca Raton, FL, USA: CRC Press, ISBN: 978-1138072855, Mar. 2017.

[3] B. Bilgin, J. Liang, M. Terzic, J. Dong, R. Rodriguez, E. Trickett, and A. Emadi, “Modeling and analysis of electric motors: state-of-the-art review,” *IEEE Transactions on Transportation Electrification*, vol. 5, no. 3, pp. 602-617, Sep. 2019.

[4] E. Bostanci, M. Moallem, A. Parsapour and B. Fahimi, “Opportunities and challenges of switched reluctance motor drives for electric propulsion: a comparative study, ” *IEEE Transactions on Transportation Electrification*, vol. 3, no. 1, pp. 58-75, Mar. 2017.

[5] S. Li, S. Zhang, T. G. Habetler and R. G. Harley, “Modeling, design

optimization, and applications of switched reluctance machines—a review, ” *IEEE Transactions on Industry Applications*, vol. 55, no. 3, pp. 2660-2681, May-June 2019.

[6] J. W. Jiang, J. Liang, J. Dong, B. Howey, and A. D. Callegaro, “Noise and vibration in switched reluctance machines,” in *Switched Reluctance Motor Drives: Fundamentals to Applications.* Boca Raton, FL, USA: CRC Press, ISBN: 978-1138304598, Nov. 2018.

[7] J. Dong, J. Jiang, B. Howey, H. Li, B. Bilgin, A. D. Callegaro, and A. Emadi., “Hybrid acoustic noise analysis approach of conventional and mutually coupled switched reluctance motors,” *IEEE Transactions on Energy Conversion*, vol. 32, no. 3, pp. 1042–1051, Feb. 2017.

[8] M. Zhang, I. Bahri, X. Mininger, C. Vlad and E. Berthelot, “Vibration reduction control of switched reluctance machine, ” *IEEE Transactions on Energy Conversion*, vol. 34, no. 3, pp. 1380-1390, Sep. 2019.

[9] J. Liang, Y. Li, C. Mak, B. Bilgin, D. Al-Ani, and A. Emadi, “A comprehensive analysis of the acoustic noise in an interior permanent magnet traction motor,” in *Proc. IEEE Energy Conversion Congress and Exposition (ECCE)*, Sep. 2019.

[10] F. Lin, S. Zuo, and X. Wu, “Electromagnetic vibration and noise analysis of permanent magnet synchronous motor with different slot-pole combinations,” *IET Electric Power Applications*, vol. 10, no. 9, pp. 900-908, Nov. 2016.

[11] S. M. Castano, B. Bilgin, E. Fairall, and A. Emadi, “Acoustic noise analysis of a high-speed high-power switched reluctance machine: frame effects,” *IEEE Transactions on Energy Conversion*, vol. 31, no. 1, pp. 69-77, Mar. 2016.

[12] J. Liang, J. W. Jiang, A. D. Callegaro, B. Bilgin, J. Dong, D. Reeves, and A. Emadi, “Prediction of acoustic noise and vibration of a 24/16 traction switched reluctance, machine,” *IET Electrical Systems in Transportation*, 2019, Early Access.

[13] M. S. Islam, R. Islam, and T. Sebastian, “Noise and vibration characteristics of permanent-magnet synchronous motors using electromagnetic and structural analyses,” *IEEE Transactions on Industry Applications*, vol. 50, no. 5, pp. 3214-3222, Sep. 2014.

[14] X. Guo, R. Zhong, M. Zhang, D. Ding and W. Sun, “Resonance reduction by optimal switch angle selection in switched reluctance motor, ” *IEEE Transactions on Industrial Electronics*, vol. 67, no. 3, pp. 1867-1877, Mar. 2020.

[15] H. Kim, C. Nerse, J. Lee and S. Wang, “Multidisciplinary analysis and multiobjective design optimization of a switched reluctance motor for improving sound quality, ” *IEEE Access*, vol. 7, pp. 66020-66027, June 2019.

[16] Y. Fang and T. Zhang, “Vibroacoustic characterization of a permanent magnet synchronous motor powertrain for electric vehicles,” *IEEE*

Transactions on Energy Conversion, vol. 33, no. 1, pp. 272-280, Mar. 2018.

[17] M. Bösing, "Acoustic modeling of electrical drives," Ph.D. Dissertation, RWTH Aachen University, Aachen, Germany, 2014.

[18] Z. Yang, F. Shang, I. P. Brown, and M. Krishnamurthy, "Comparative study of interior permanent magnet, induction, and switched reluctance motor drives for EV and HEV applications," *IEEE Transactions on Transportation Electrification*, vol. 1, no. 3, pp. 245-254, Oct. 2015.

[19] D. J. Inman, *Engineering Vibration*. Upper Saddle River, Pearson Education, NJ, USA: ISBN: 978-0132871693, Mar. 2013.

[20] A. D. Callegaro, B. Bilgin, and A. Emadi, "Radial force shaping for acoustic noise reduction in switched reluctance machines,". *IEEE Transactions on Power Electronics*, vol. 34, no. 10, pp. 9866-9878, Oct. 2019.

[21] A. D. Callegaro, J. Liang, J. W. Jiang, B. Bilgin, and A. Emadi, "Radial force density analysis of switched reluctance machines: the source of acoustic noise," *IEEE Transactions on Transportation Electrification*, vol. 5, no. 1, pp. 93-106, Mar. 2019.

[22] G. Jacek, C. Wang, and J. Lai. *Noise of Poly-Phase Electric Motors*. Boca Raton, FL, USA: CRC Press, ISBN: 9780824723811, Dec. 2005.

[23] C. Wang and J. Lai, "Prediction of natural frequencies of finite length circular cylindrical shells," *Applied Acoustics*, vol. 59, no. 4, pp. 385-400, July 1999.

[24] J. W. Jiang and J. Liang, “Fundamentals of vibrations and acoustic noise,” in *Switched Reluctance Motor Drives: Fundamentals to Applications.* Boca Raton, FL, USA: CRC Press, ISBN: 978-1138304598, Nov. 2018.

[25] X. Guo, R. Zhong, M. Zhang, D. Ding, and W. Sun, “Fast computation of radial vibration in switched reluctance motors,” *IEEE Transactions on Industrial Electronics*, vol. 65, no. 6, pp. 4588-4598, June 2018.

[26] Z. Tang, P. Pillay, and A. Omekanda, “Vibration prediction in switched reluctance motors with transfer function identification from shaker and force hammer tests,” *IEEE Transactions on Industry Applications*, vol. 39, no. 4, pp. 978–985, July 2003.

[27] M. Kimpara, S. Wang, R. Reis, J. Pinto, M. Moallem and B. Fahimi, “On the cross coupling effects in structural response of switched reluctance motor drives, ” *IEEE Transactions on Energy Conversion*, vol. 34, no. 2, pp. 620-630, June 2019.

[28] K. Rao, D. Kim, J. Hwang, *Fast Fourier Transform: Algorithms and Applications*. Netherlands: Springer, ISBN: 978-94-007-3359-6, Feb. 2011.

[29] K. Shin and J. Hammond, *Fundamentals of Signal Processing for Sound and Vibration Engineers*. West Sussex, UK: John Wiley & Sons, ISBN: 978-0470511886, Apr. 2008.

Chapter 7: Pattern of Radial Force Density Harmonics in Switched Reluctance Machines

As presented in Chapter 4 and Chapter 5, the harmonic components in the acoustic noise are caused mainly by the radial force density harmonics in the stators for internal-rotor (IR) SRMs and the rotors for external-rotor (ER) SRMs. It is essential to calculate and obtain the temporal and circumferential orders of the radial force density harmonics for a certain SRM topology in the design and control of the SRMs. Applying 2D FFT on the radial force density is a general method to obtain the harmonic components. However, it is often time-consuming to obtain the radial force density by either electromagnetic FEA simulation or motor dynamic modeling. The goal of this chapter is to present an analytical expression to calculate the temporal and circumferential orders for different SRM topologies directly without running the electromagnetic FEA simulation.

7.1 Introduction

Although SRM has a simple, robust, and magnet-free structure, the salient pole construction is causing a more considerable acoustic noise compared with the induction machines and permanent magnet synchronous machines [1]-[2]. During the operation, an SRM produces acoustic noise with many harmonic components. The harmonic components of the acoustic noise, which are caused by the harmonics of the radial force density, should be reduced to achieve acoustic noise reduction [3]-[6]. The study of the radial force density harmonics is the basis for the reduction of noise and vibration in SRMs [7]-[9].

The radial electromagnetic force density in the air gap is a function of time and circumferential position. For acoustic noise analysis, the radial force density waveform should be decomposed into harmonic components with different temporal and circumferential orders. In [10]-[11], the circumference-position-varying and time-varying radial electromagnetic force density is decomposed first by 1D fast Fourier transform (FFT) in the circumferential domain and then by 1D FFT in the time domain. 2D FFT can also be applied on the radial force density waveform in order to decompose it directly into harmonics components with different temporal and circumferential orders. In [12], the harmonics of the radial force density in a 24/16 SRM at 2000 rpm is obtained by 2D FFT. In [13], the harmonics of the radial force density between a 12/10/12 double-stator SRM and a 12/8 SRM have been compared. With 2D FFT analysis on the radial force density of a 12/8 SRM, it was concluded in [9] that the lowest non-zero circumferential order of the radial force harmonics can be calculated by the number of stator poles divided by the number of phases. However, a comprehensive study on the pattern of the harmonics in the radial force density of SRMs is not reported in the literature.

In this chapter, the feasible pole configuration in SRMs is first discussed and divided into several categories based on their different phase excitation sequences as presented in Section 7.2. This chapter aims at developing the pattern of radial force density harmonics for SRMs with the phase excitation sequence both in counter clockwise (CCW) and clockwise (CW) directions. The characteristics of the electromagnetic force density, the relationship between the electromagnetic force density and the vibration, are discussed in Section 7.3. The rotational direction of the radial force waveform is related to the rotational direction of the rotor and the phase excitation sequence. This is determined by the SRM topology. The pattern for the radial force density harmonics is obtained by summarizing several different SRMs, including the 6/4, 24/16, and 6/14 IR SRMs, and 12/16 and 18/24 ER SRM. The test results of an 8/6 IR SRM and a 12/16 ER SRM is used to validate the pattern of the radial force harmonics for stators of IR SRMs and rotors of ER SRMs.

7.2 Pole Configuration and Phase Excitation Sequence of SRMs

The pattern of the electromagnetic force density harmonics for different SRMs depends on the pole configuration. Feasible SRM configurations with an even number of stator poles and rotor poles are summarized in Table 7-1. The numbers in the cells show the number of phases for the given number of stator and rotor poles.

Table 7-1. The number of stator poles, number of rotor poles and number of phases in feasible SRM topologies [14].

		Number of stator poles, N_s						
Number of rotor poles, N_r		6	8	10	12	14	16	18
	2	3	4	5	6	7	8	9
	4	3	-	5	3	7	4	9
	6	-	4	5	-	7	8	3
	8	3	-	5	3	7	-	9
	10	3	4	-	6	7	8	9
	12	-	-	5	-	7	4	3
	14	3	4	5	6	-	8	9
	16	3	-	5	3	7	-	9
	18	-	4	5	-	7	8	-
	20	3	-	-	3	7	4	9
	22	3	4	5	6	7	8	9
	24	-	-	5	-	7	-	3

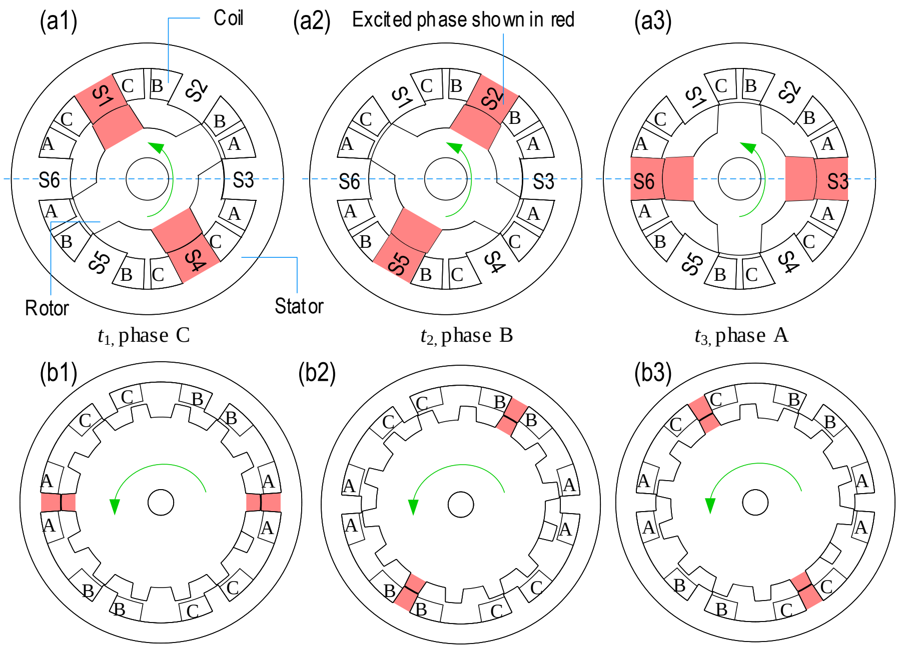

t_1, phase C

t_2, phase B

t_3, phase A

t_2, phase A

t_3, phase B

t_1, phase C

Fig. 7-1 Phase excitation sequences of different SRM configurations when rotor rotates in CCW direction, (a) three-phase 6/4 internal-rotor (IR) SRM, CW phase excitation (Ph#C-B-A), (CW), (b) three-phase 6/14 IR SRM, CCW phase excitation (Ph#A-B-C).

When the rotor rotational direction is fixed, the SRMs can be divided into different categories based on the direction of the phase excitation sequence.

Assuming that the rotor is rotating in the CCW direction and the phases are excited individually, there are two types of phase excitation sequence: CW and CCW. Fig. 7-1(a) shows a 6/4 IR SRM with CW phase excitation, and Fig. 7-1(b) shows a 6/14 IR SRM with CCW phase excitation. The rotational direction of the electromagnetic force density waveform (radial and tangential components) on the stator is the same as that of the phase excitation sequence. For example, if the phase excitation sequence is CW, the rotational direction of the electromagnetic force density waveform of the stator is also CW. The rotational direction of the electromagnetic force has an effect on the pattern of harmonics of the force density waveform, which will be discussed in Section 7.4. Before that, we need to analyze the characteristics of the electromagnetic force density waveform and its relationship with vibrations.

7.3 Characteristics of Electromagnetic Force Density

During the operation of an SRM, the electromagnetic force density waveform is generated in the air gap and acts on both the stator and the rotor. Fig. 7-2 shows the electromagnetic force applied on the stator and the rotor of a three-phase 24/16 IR SRM at 2000 rpm at t = 0.8 ms, which is simulated in JMAG. In Fig. 7-2, there are eight major groups of force vectors acting on the stator and the rotor, respectively. This is because in a three-phase 24/16 SRM there are eight stator poles per phase.

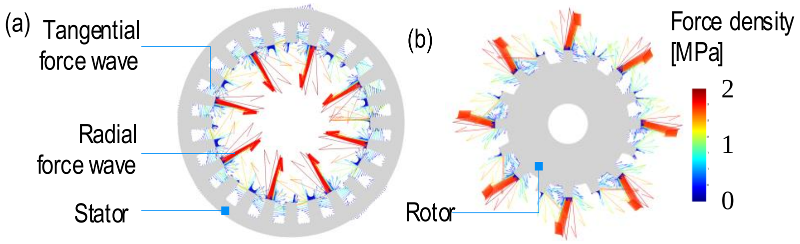

Fig. 7-2. Electromagnetic force density of a 24/16 IR SRM at 2000 rpm with a reference current of 240A, *t* = 0.8 ms, (a) the stator, (b) the rotor.

The electromagnetic forces of a 12/16 ER SRM designed for an E-bike traction application are shown in Fig. 7-3. As discussed in Chapter 5, the radial vibration of the rotor and the connected endcaps is the main reason for the acoustic noise in the external-rotor SRMs. Since there are four stator poles per phase in a three-phase 12/16 SRM, four major force surges are acting on the rotor and the stator in Fig. 7-3.

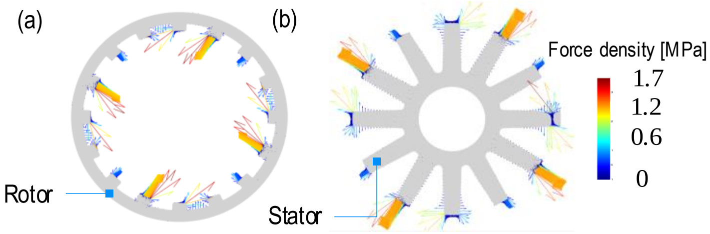

Fig. 7-3. Nodal force of an ER 12/16 SRM at 400 rpm and with a reference phase current of 75 A, t = 2.5 ms, (a) rotor, (b) stator.

Fig. 7-2 and Fig. 7-3 show that the electromagnetic forces on the stator or the rotor is a function of circumferential positions. The electromagnetic force density, including the radial and the tangential components, also changes with time when different phases are excited sequentially. The following discussion will be using the radial force density waveform of a 6/4 SRM stator in an electrical cycle (see Fig. 7-4) as an example to illustrate the time-varying property. When the phases of the winding are excited sequentially (Ph#C-B-A) and in the CW direction, the radial force density is applied on the stator poles in the CW direction. Since the radial and tangential force densities are components of the electromagnetic force density, the tangential force density waveform is also in the same rotational direction as that of the radial force density waveform.

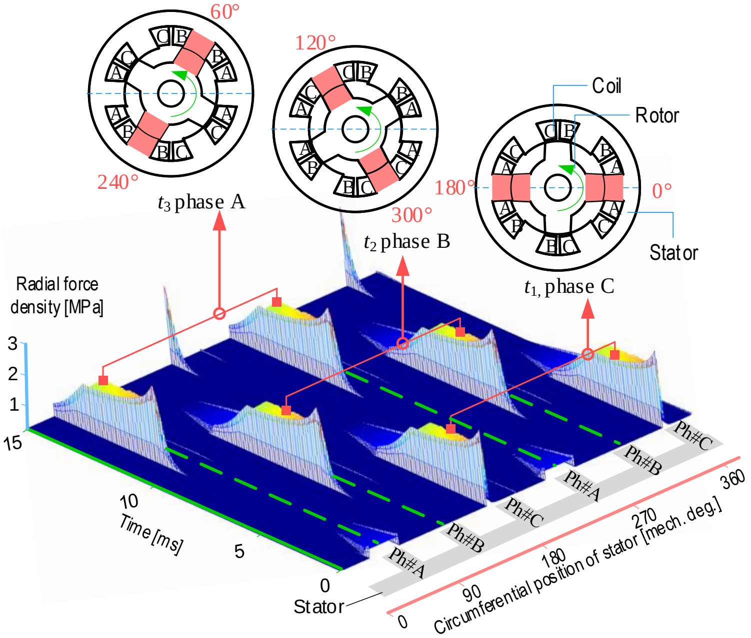

Fig. 7-4 Time- and circumferential position-varying radial force density waveform of the stator in a 6/4 IR SRM, at 1000 rpm with a reference phase current of 20 A.

7.4 Radial Force Density Harmonics

This section will discuss the harmonics in the radial force density of several SRMs, including 6/4, 24/16, 6/14 IR SRMs, and 18/24, 12/16 ER SRMs. Based on these analyses, the pattern for the harmonics in the radial force density of SRMs will be obtained.

7.4.1 Rotational Direction of Radial Force Density Waveform

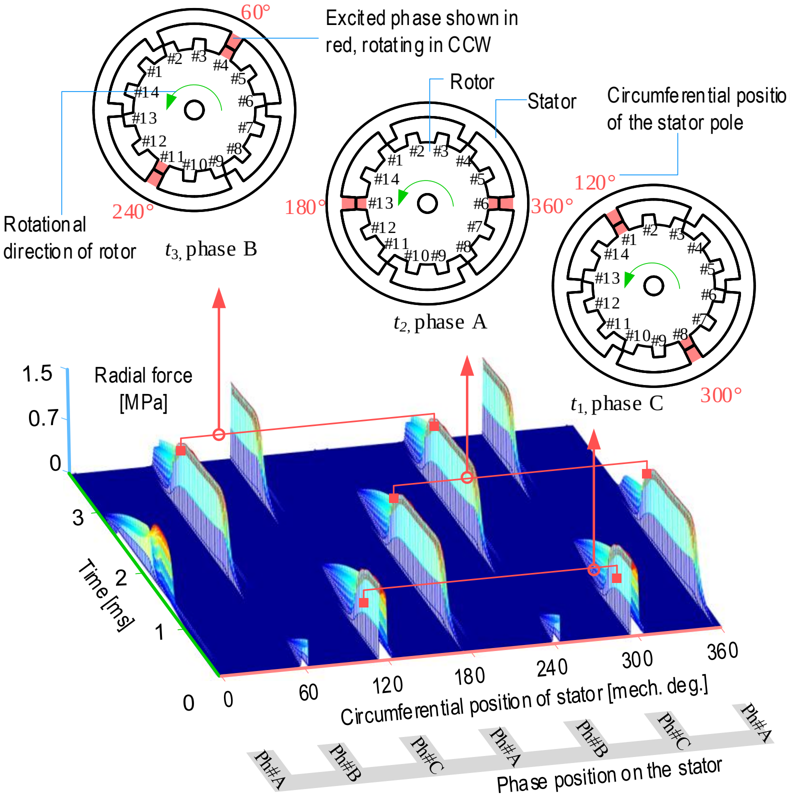

Fig. 7-5. Radial force density waveform in an IR 6/14 SRM stator at 1200 rpm with a reference phase current of 7.5 A.

The rotational direction of the radial force density will be discussed first because it affects the pattern of the harmonics of the radial force density. Taking the 6/14 IR SRM as an example, Fig. 7-5 shows the radial force density on the stator as a function of time and circumferential position as the rotor rotates in the CCW direction. At t_1, Ph#C is excited and two force spikes appear at circumferential positions of 120 [mech. deg.] and 300 [mech. deg]. At t_2, Ph#A is excited and the two spikes of the radial force appear at 180 [mech. deg.] and 360 [mech. deg]. Similarly, at t_3, Ph#B is excited and there are two spikes of the radial force appearing at 60 [mech. deg.] and 240 [mech. deg.]. Therefore, the radial force density on the stator is rotating in the same direction as the phase excitation sequence; the CCW direction. This is valid to all the other IR SRMs: the radial force density on the stator is always rotating in the same direction as the phase excitation sequence. This is also true for the tangential force density of IR SRM rotors.

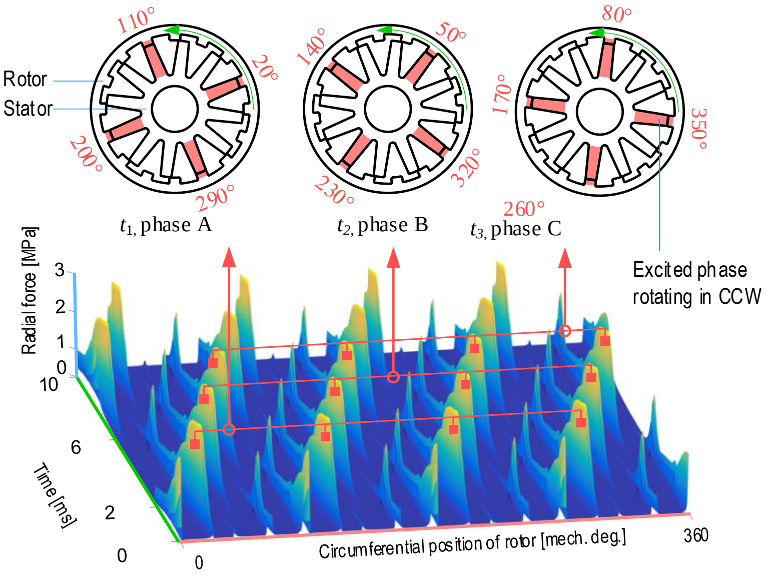

Fig. 7-6. The radial force density waveform of the rotor in a 12/16 ER SRM at 400 rpm and with a reference phase current of 75 A.

The rotational direction of the radial force density of the ER SRM rotor will be discussed in this section by using the radial force density of the 12/16 SRM rotor as an example, which is shown in Fig. 7-6. At t_1, Ph#A is excited and four force spikes appear at 20, 110, 200, 290 [mech. deg]. At t_2, Ph#B is excited and the four spikes of the radial force appear at 50, 140, 230, 320 [mech. deg]. Similarly, at t_3, Ph#C is excited and there are four spikes of the radial force appearing at 80, 170, 260, 350 [mech. deg]. Therefore, when the phase excitation sequence is in the CCW direction, the rotational direction of the radial force on the rotor is in the CCW direction, which is the same as that of the rotor rotational direction.

Table 7-2. Relationship between directions of radial force waveform, winding phase excitation sequence, and rotor rotational direction of several SRMs.

SRM	6/4 IR	24/16 IR	8/6 IR	6/14 IR	18/24 ER	12/16 ER
Number of Phases	3	3	4	3	3	3
Motor part for analysis	Stator	Stator	Stator	Stator	Rotor	Rotor
Rotor rotational direction	CCW	CCW	CCW	CCW	CCW	CCW
Phase excitation sequence	C-B-A	C-B-A	D-C-B-A	A-B-C	A-B-C	A-B-C
Direction of the phase excitation sequence	CW	CW	CW	CCW	CCW	CCW
The rotational direction of radial force waveform in the stator	CW	CW	CW	CCW	CCW	CCW
Rotational direction of radial force waveform in the rotor	CW	CW	CW	CCW	CCW	CCW

More comparison of the rotational directions of the radial force density on the stators or rotors in several SRMs can be seen in Table 7-2. The radial force density on the ER SRM stators is also in the CCW direction, which is the same as that of the phase excitation sequence. However, as discussed in Section 7.3, the radial force density on the ER SRM stator has a relatively small effect on the total acoustic noise. Although the rotational direction of the radial force waveform on the 6/14 SRM rotor is also in the CCW direction, the radial force density is applying on the 6/14 IR SRM rotor in a different way compared with the other

SRM rotors or stators listed in Table 7-2. In the stators and the rotors of the 6/4, 24/16, and 8/6 IR SRMs, and 18/24 and 12/16 ER SRMs, the radial force density is applied on the stator and the rotor poles sequentially without skipping any poles. This also applies to the stator of the 6/14 SRM. For the rotor of the 6/14 IR SRM, the radial force density is applied on the rotor poles in the CCW direction, but not in a sequential way. As shown in Fig. 7-5, when Ph#C is excited at t_1, the radial force density is applied on rotor pole #1 and #8. When Ph#A is excited at t_2, the radial force density is applied on rotor pole #13 and #6. When Ph#B is excited at t_3, the radial force density is applied on rotor pole #11 and #4. This chapter focuses on obtaining the pattern of the radial force density harmonics for SRM topologies, which are applied on the poles sequentially without skipping any poles. Therefore, the expressions derived in the next section to determine the harmonics would not apply to the rotor of 6/14 IR SRM.

7.4.2 Stators of the Internal-Rotor SRMs

In the 6/4 and 24/16 IR SRMs, where the number of stator poles is larger than the number of rotor poles, the excitation sequence is Ph#C-B-A, which is in the CW direction. This causes the rotors of the 6/4 and 24/16 IR SRMs to rotate in the CCW direction. Due to the fact that the phase excitation sequence is CW, the rotational directions of the radial force density in 6/4 and 24/16 IR SRMs stators are in CW. This CW direction of the radial force waveform can also be observed in the waveforms in Fig. 7-4 and Fig. 7-7(a). When Ph#C is excited at $t = t_1$, the circumferential position of the stator is larger than that when Ph#B is excited at $t = t_2$. The similar case is true when Ph#A is excited at $t = t_3$.

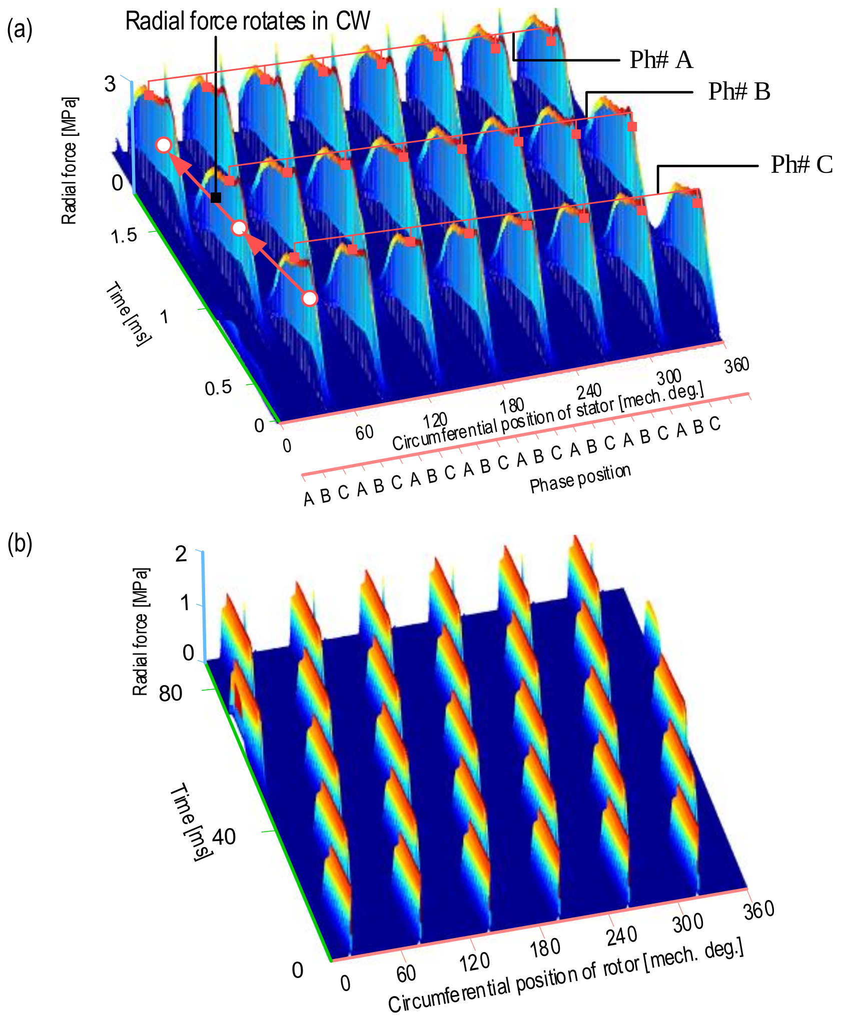

Fig. 7-7 (a) Radial force density waveform of the stator in an internal-rotor 24/16 SRM at 2000 rpm with a phase reference current of 240 A, (b) radial force density waveform of the rotor in an external-rotor 18/24 SRM at 50 rpm and with a reference phase current of 7A.

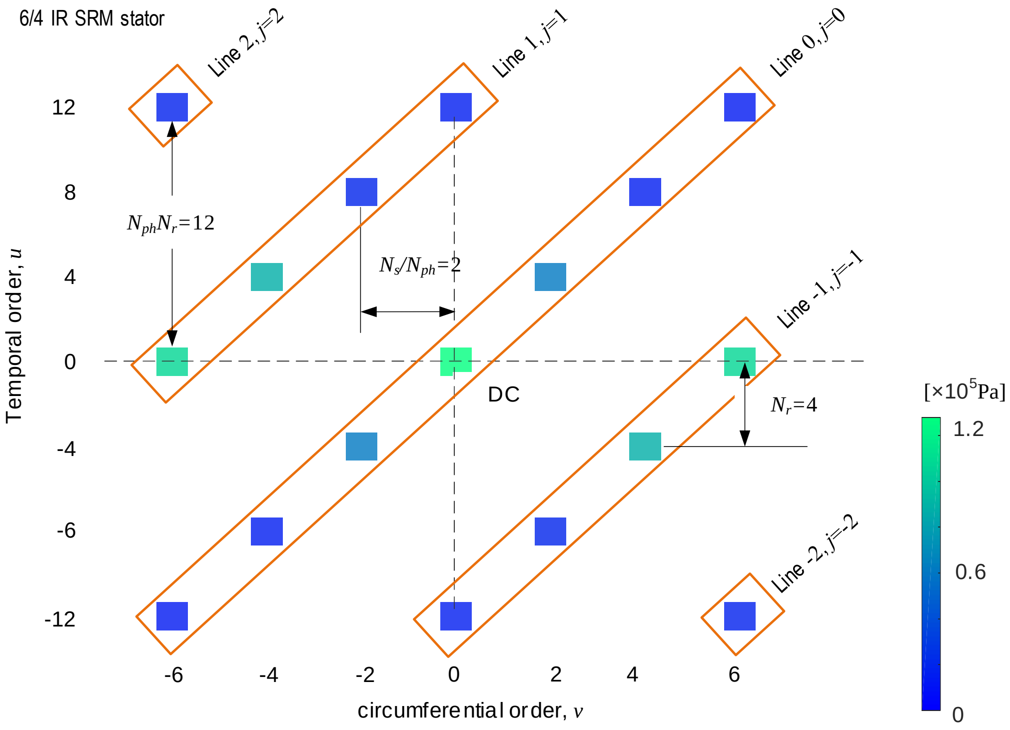

Fig. 7-8. Radial force density harmonics, a 6/4 IR SRM stator at 1000 rpm with a reference phase current of 20 A when the rotor rotates in CCW direction.

The radial force density harmonics of the 6/4 and 24/16 IR SRM stators are shown in Fig. 7-8 and Fig. 7-9, respectively. The harmonics of the radial force density appear in the diagonal direction. The diagonal direction is moving from the bottom left corner to the upper right corner both for 6/4 and 24/16 SRMs. Each diagonal line is labeled with the different value of *j*. For the same *u*-*v* range, the harmonics of the 6/4 IR SRM stator would be denser as compared to 24/16 IR SRM stator, because 6/4 SRM has two magnetic poles whereas 24/16 SRM has eight. The temporal and circumferential orders of each harmonic component in the 6/4 and 24/16 IR SRM stators can be described by (7.1) and (7.2), respectively.

$$\text{For 6/4 IR SRM: } \begin{cases} u = N_{ph} \times N_r + N_r \times k = 12 \times j + 4 \times k \\ v = \dfrac{N_s}{N_{ph}} \times k = 2 \times k \end{cases} \tag{7.1}$$

$$\text{For 24/16 IR SRM: } \begin{cases} u = 48 \times j + 16 \times k \\ v = 8 \times k \end{cases} \tag{7.2}$$

where N_{ph} is the number of phases, N_{r} is the number of rotor poles, N_{s} is the number of stator poles, j and k can be any integer.

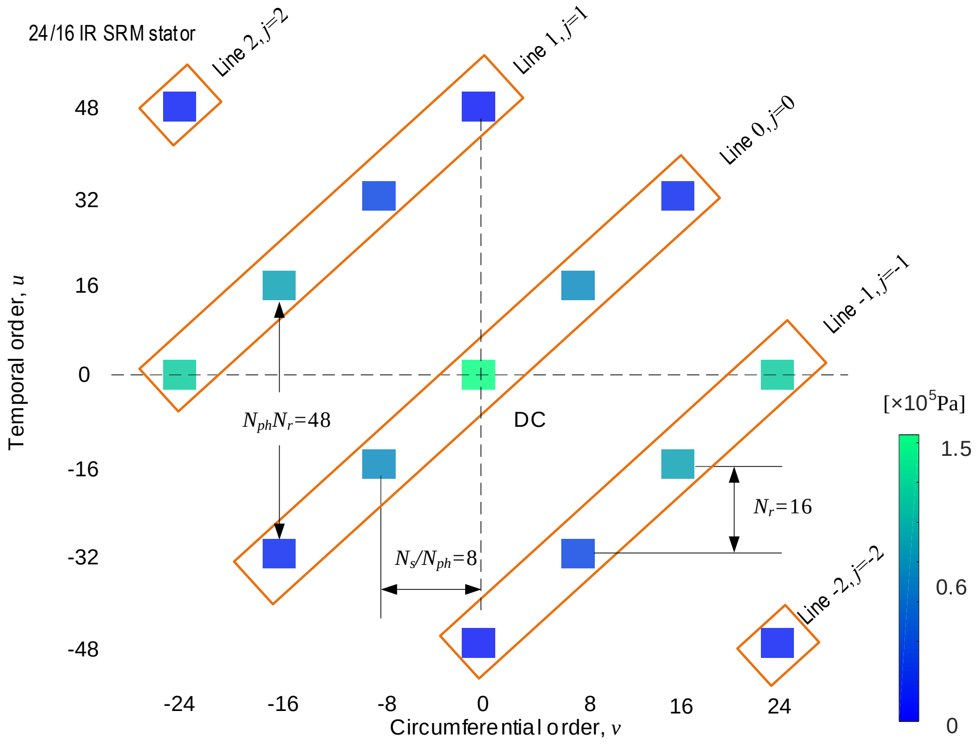

Fig. 7-9. Radial force density harmonics, a 24/16 IR SRM stator at 2000 rpm and with a reference phase current of 240 A when the rotor rotates in CCW direction.

The geometry of the 6/14 SRM and the radial force density on the stator can be seen in Fig. 7-5. Compared with the 6/4 and 24/16 IR SRMs, the number of the stator poles in the 6/14 IR SRM is smaller than the rotor poles. The rotor of the 6/14 SRM also rotates in the CCW. As shown in Fig. 7-5, the phase excitation sequence of the 6/14 SRM is Ph#A-B-C, which is rotating in CCW. The harmonics of the radial force density on the stator of the 6/14 SRM is shown in Fig. 7-10. Unlike the 6/4 SRM and 24/16 SRM, each line in Fig. 7-10 has a negative gradient. Then, the temporal and circumferential orders of the harmonics can be expressed as:

$$\begin{cases} u = 42\times j - 14\times k \\ v = 2\times k \end{cases} \tag{7.3}$$

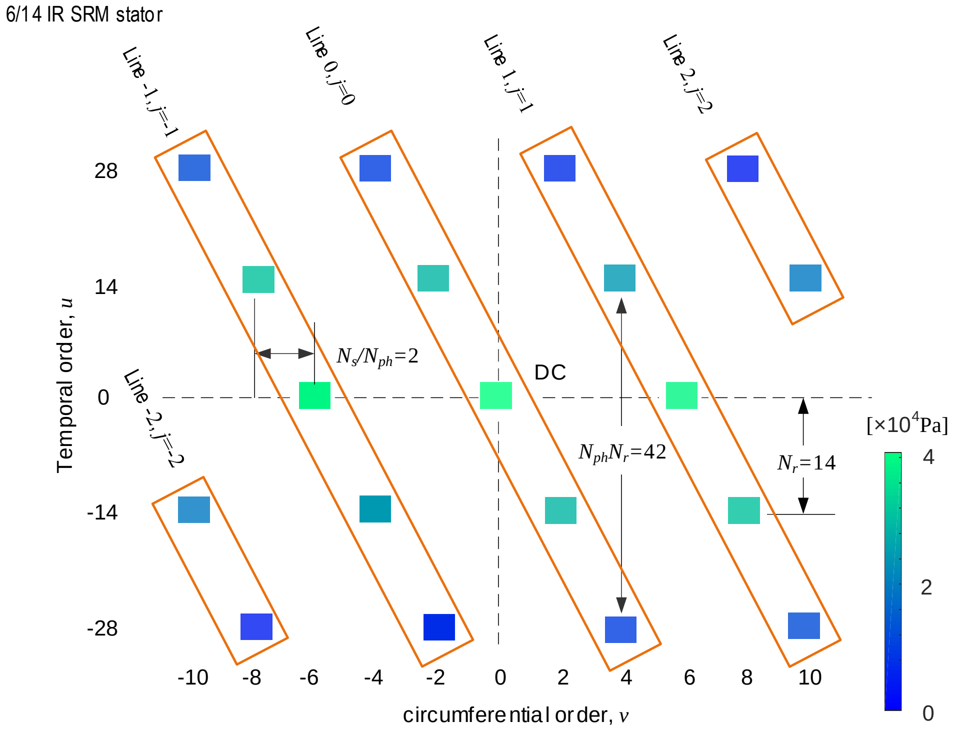

Fig. 7-10. Radial force density harmonics, a 6/14 IR SRM stator at 1200 rpm with a reference phase current of 7.5 A when the rotor rotates in CCW direction.

7.4.3 Rotors of the External-Rotor SRMs

In this section, the 12/16 and the 18/24 ER SRM will be used to illustrate the characteristics in the radial force density in the rotor of the external-rotor SRMs. The geometry of the 12/16 ER SRM and the radial force density on the rotor is shown in Fig. 7-6. The rotor is rotating in the CCW direction, which also makes the direction of radial force density on the rotor rotate in CCW.

Fig. 7-11 shows the harmonics of the radial force in the rotor of the 12/16 ER SRM. The harmonics have a negative gradient. The pattern for the harmonics can be described as in (7.4).

$$\begin{cases} u = 48\times j - 12\times k \\ v = 4\times k \end{cases} \tag{7.4}$$

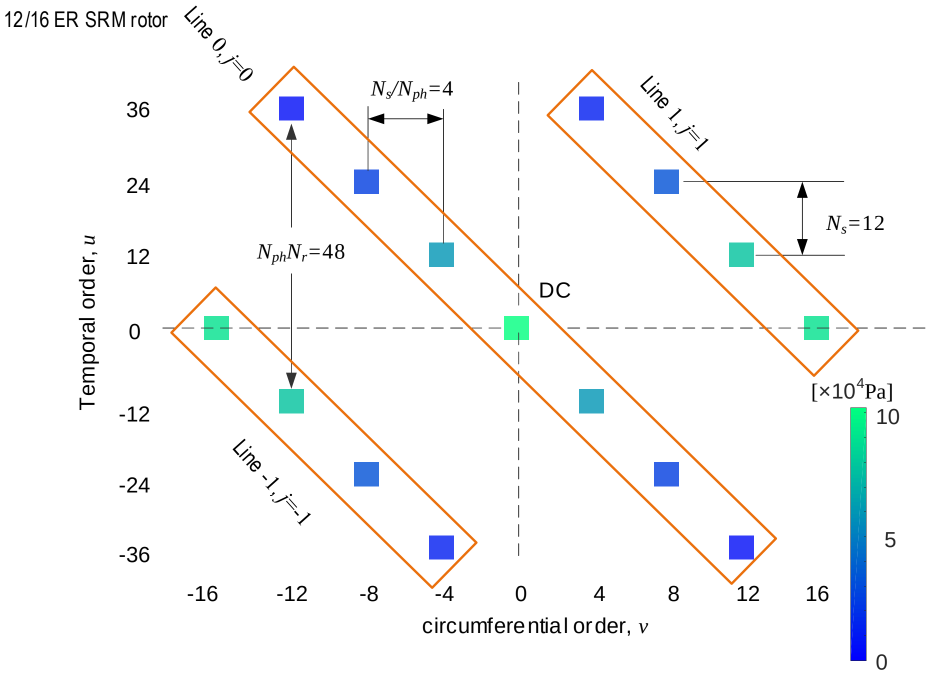

Fig. 7-11. Radial force density harmonics, rotor of an 12/16 ER SRM at 400 rpm and with a reference phase current of 75 A.

Another example of the external-rotor SRM, the 18/24 SRM, is also studied in this section. The design details of the external-rotor 18/24 SRM is presented in [16]. The radial force density applied to the external rotor can be seen in Fig. 7-7(b). Similarly, the rotor is still rotating in the CCW direction and the radial force density on the rotor also rotates in the CCW direction. Each line of the harmonics in Fig. 7-12 has a negative gradient, which is similar to that in the radial force density of the 12/16 ER SRM rotor. Hence, the harmonics can be described by :

$$\begin{cases} u = 72\times j - 18\times k \\ v = 6\times k \end{cases} \tag{7.5}$$

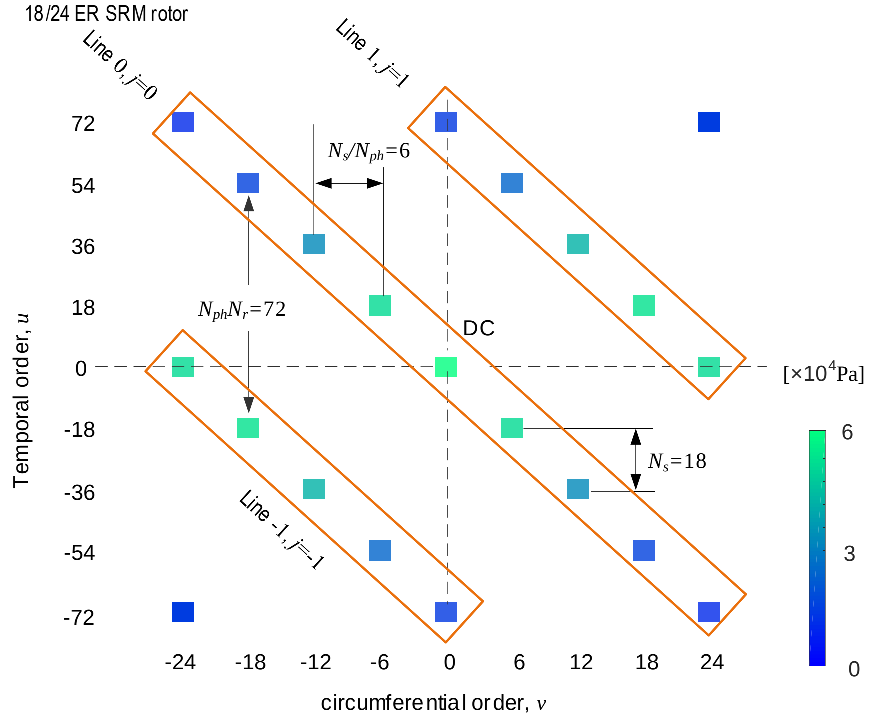

Fig. 7-12. Radial force density harmonics, rotor of an 18/24 ER SRM at 50 rpm with a reference phase current of 7A.

It should be noted that limited number of temporal orders have been shown in the radial force density harmonics in Fig. 7-8 to Fig. 7-12. The higher temporal orders would still cause acoustic noise in SRMs, which should not be ignored. The effect of higher temporal orders will be shown in the experimental results in Section 7.5.

7.4.4 The Pattern for Radial Force Harmonics

Based on the analyses of the radial force density harmonics of the 6/4, 24/16, 6/14 IR SRM stators, and the 12/16, 18/24 ER SRM rotors, it can be seen that the locations (temporal and circumferential orders) of the radial force harmonics in the *u*-*v* plane depends on the SRM pole configurations. The temporal order, *u*, and circumferential order, *v*, of the radial force harmonics can be described as:

$$\begin{cases} u = N_{ph} \times N_r \times j + \alpha \times \beta \times N \times k \\ v = \dfrac{N_s}{N_{ph}} \times k \end{cases} \tag{7.6}$$

where $N_{ph} \times N_r$ is the number of strokes in one mechanical revolution, the coefficients, α, β and N, depend on the pole configuration and the rotational direction of the rotor:

$$\begin{aligned} &\begin{cases} \alpha = 1, \text{ if the rotor rotates at CCW} \\ \alpha = -1, \text{ if the rotor rotates at CW} \end{cases} \\ &\begin{cases} \beta = 1, \text{ if } N_s > N_r \\ \beta = -1, \text{ if } N_r > N_s \end{cases} \\ &\begin{cases} N = N_r \text{ for IR stator} \\ N = N_s \text{ for ER rotor} \end{cases} \end{aligned} \tag{7.7}$$

It should be noted that in (7.6), the circumferential orders of the radial force harmonics are only related to the number of magnetic poles and, hence, the number of stator poles, N_s, and the number of phases, N_{ph}. This is because when one phase is excited, the number of radial force surges applied on the rotor and the stator will always be N_s/N_{ph}. It should be noted that (7.6) is applicable for SRM pole configurations, in which the phases are excited individually and the electromagnetic forces are applied on the poles sequentially without skipping any poles.

The rotational direction of the radial force density waveform is determined by the multiple of $\alpha \times \beta$, and it depends on the rotor rotational direction and the SRM pole configuration. The temporal orders are related to the number of strokes, $N_{ph} \times N_{r,}$ the number of rotor poles, N_r, for IR SRM stators, the number of stator poles, N_s, for ER SRM rotors. This is due to the periodicity of the radial force density spikes in the time and the circumferential positions [19]. The same radial force spikes with time differences are applied on each stator or rotor pole periodically. The period of the periodic and repeating radial force density spikes are related to N_{ph} and N_r , for IR SRM stators [12], [19], and N_{ph}, N_r, and N_s, for ER SRM rotors.

7.5 Experimental Results

7.5.1 8/6 Internal-Rotor SRM

In this section, the test results of the acoustic noise in a four-phase 8/6 SRM will be used to validate the pattern for the harmonics in the radial force density of IR SRM stators. By using (7.6), the harmonics of the radial force density on the stator of the 8/6 IR SRM, when the phase excitation direction is in the CW direction, and the rotor rotation is in CCW direction can be obtained as:

$$\begin{cases} u = 24 \times j + 6 \times k \\ v = 2 \times k \end{cases} \tag{7.8}$$

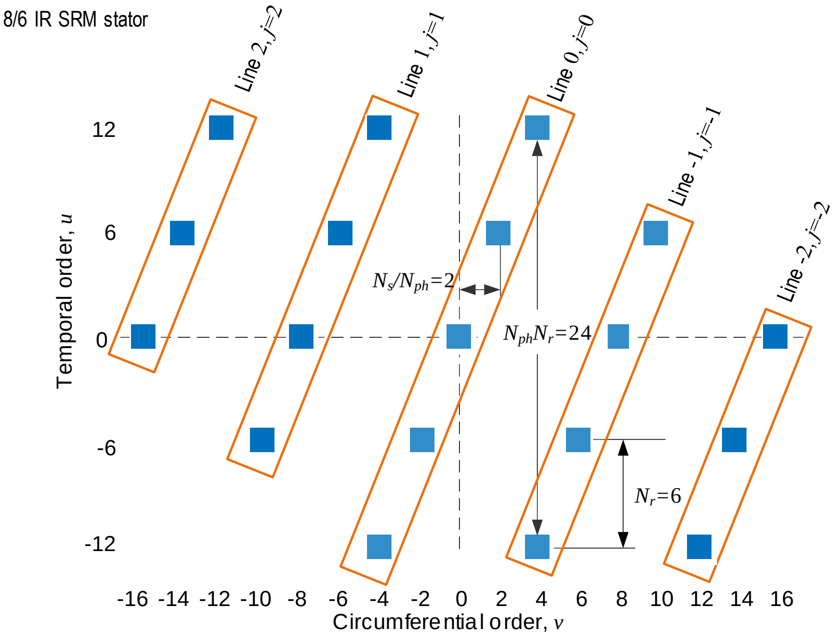

Fig. 7-13. Radial force density harmonics, stator of an 8/6 IR SRM obtained by equation (12) when the rotor spins in the CCW direction.

The harmonics of the 8/6 SRM are shown in Fig. 7-13. Table 7-3 shows the absolute values of the temporal and circumferential orders of the harmonics obtained by (7.8). The experimental setup is shown in Fig. 7-14. The natural frequencies of vibration mode two and zero are 1896 Hz and 7059 Hz, respectively, which are obtained by hammer test [17].

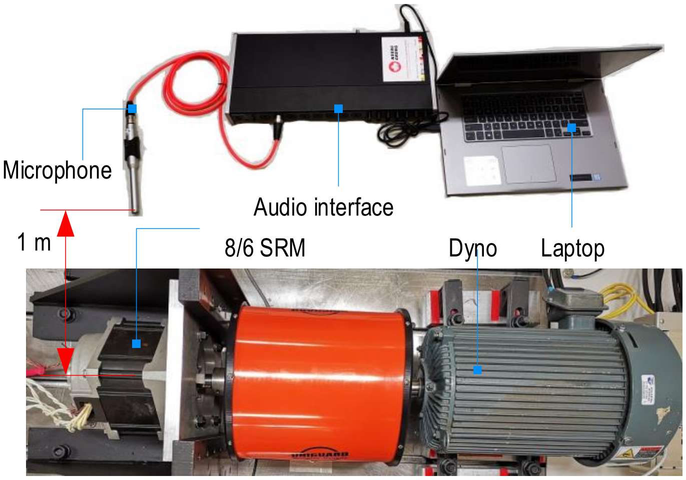

Fig. 7-14. Setup for the acoustic noise measurement of 8/6 IR SRM.

Table 7-3 Temporal and circumferential orders, ($|u|$, $|v|$) of the harmonics in the radial force density of 8/6 IR SRM stator and the 12/16 ER SRM rotor.

($\|u\|$,$\|v\|$)		
Part	Temporal order, $\|u\|$	Circumferential order, $\|v\|$
8/6 stator	24, 48, 72, 96, 120, 144, 168, …, $\|24 \times j\|$	0
	6, 18, 30, 42, 54, 66, 78, 90, 102, 114, 126, 138, 150, 162, 174, 186, 198, 210, 222, 234, 246, 258, 270, 282, …, $\|24 \times j + 6\|$	2
	12, 36, 60, 84, 108, 132, 156, 182, 204, 228, $\|24 \times j + 12\|$	4
	6, 18, 30, 42, 54, 66, 78, 90, 102, 114, 126, $\|24 \times j + 18\|$	6
12/16 rotor	48, 96, 144, 192, 240, 288, 336, 384, 432, …, $\|48 \times j\|$	0
	12, 36, 60, 84, 108, 132, 156, 180, …, $\|48 \times j - 12\|$	4
	24, 72, 120, 168, 216, 264, 312, …, $\|48 \times j - 24\|$	8

*: j can be any integer.

The tested sound pressure level (SPL) of the 8/6 SRM at 5 Nm is illustrated in Fig. 7-15(a) at 512 rpm and in Fig. 7-15(b) at 2048 rpm. The temporal order of each peak in the SPL diagram can be calculated by the frequency of the peak divided by the mechanical frequency of the motor. The mechanical frequency of the motor operating at 512 and 2048 rpm are 8.53 Hz and 34.28 Hz, respectively. The excitation of vibration mode two is the main cause of the acoustic noise for this SRM because its natural frequency is 1896 Hz. It can be seen that the temporal and the circumferential orders of each peak match the results in Table 7-3, which is obtained from (7.6).

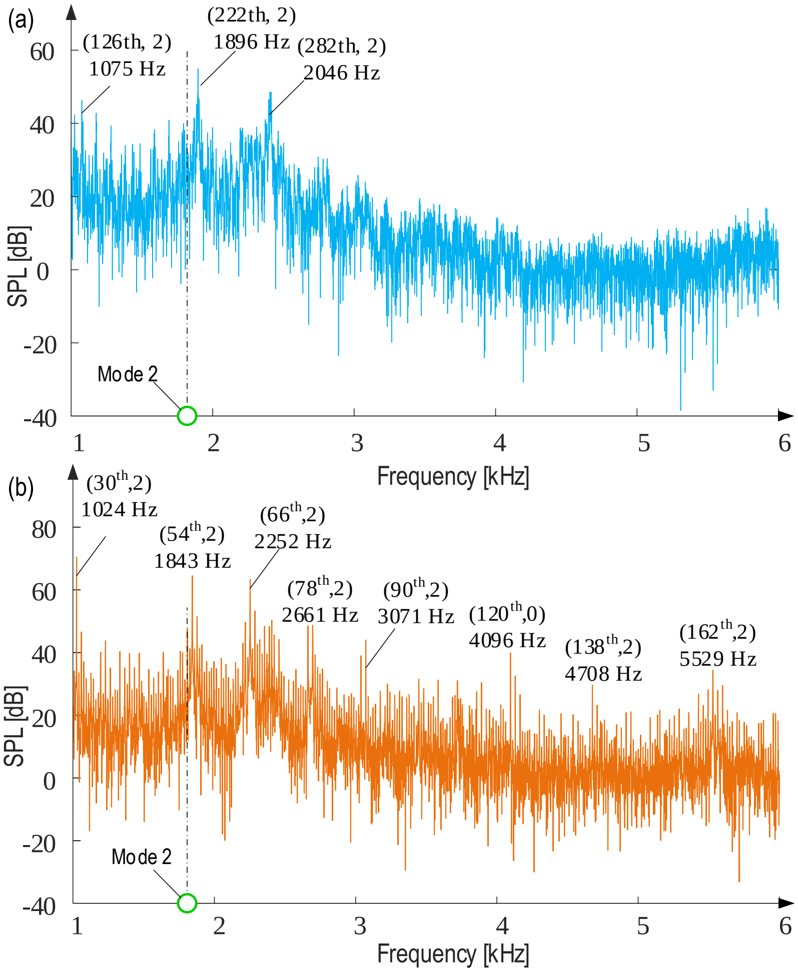

Fig. 7-15. Experimental results of the SPL in the 8/6 SRM, (a) at 512 rpm, 5 Nm, (b) at 2048 rpm, 5 Nm.

7.5.2 12/16 External-Rotor SRM

In this section, the experimental acoustic noise results of a 12/16 ER SRM prototype are used to validate the pattern for the radial force harmonics in ER SRM rotors. The detailed design of this 12/16 ER SRM is provided in [18]. The test setup for the acoustic noise is shown in Fig. 7-16. The radial force harmonics in the rotor can be calculated from (7.4) and summarized in Table 7-3. The test results of the SPL when the motor is operating at 150 rpm and 350 rpm are shown in Fig. 7-17.

(a) Top view

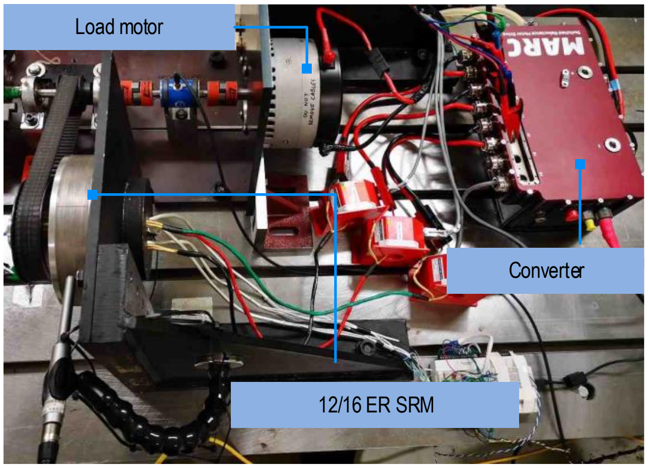

(b) Top view

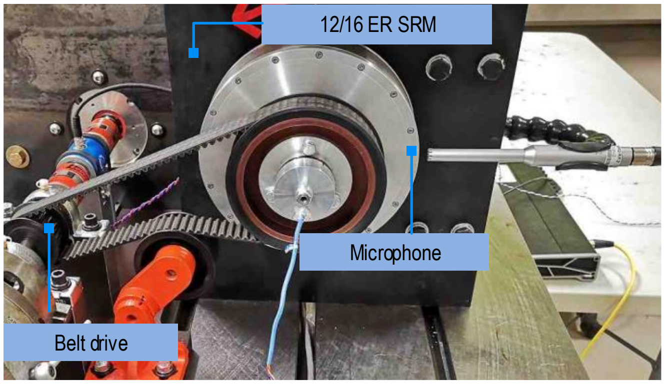

Fig. 7-16. Setup for the acoustic noise measurement of 12/16 ER SRM, (a) top view, (b) front view.

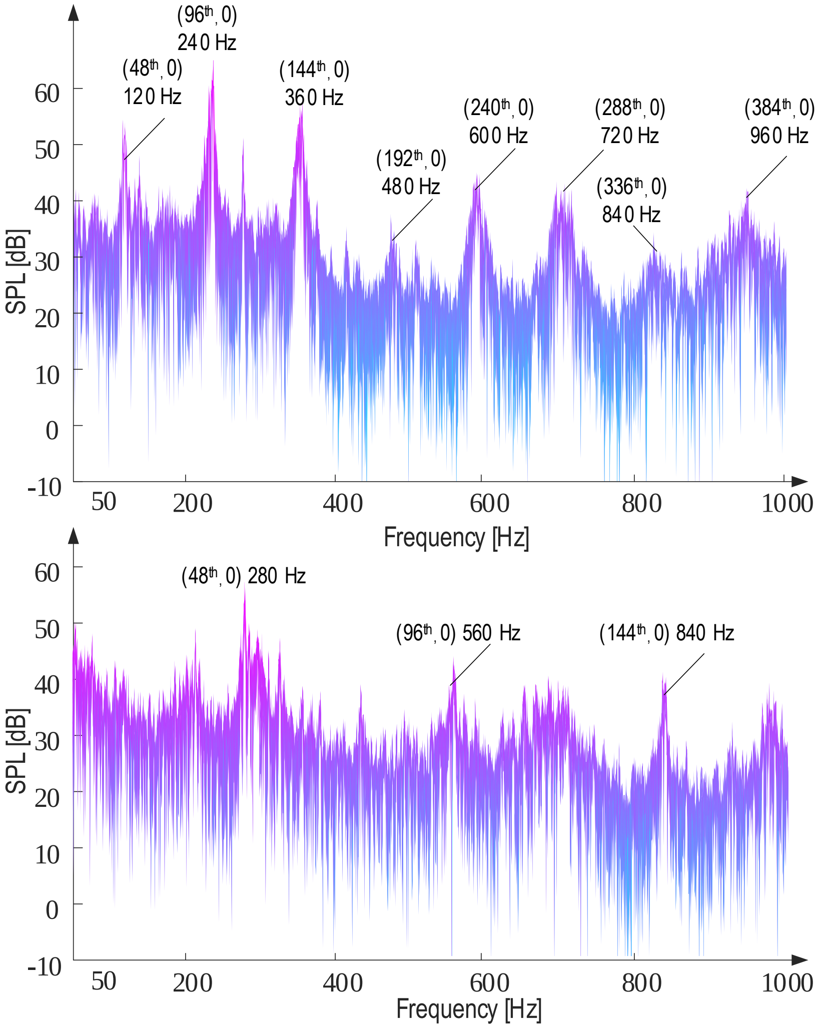

Fig. 7-17 The tested SPL in the 12/16 ER SRM prototype with a reference current of 75 A, (a) at 150 rpm, (b) at 350 rpm.

The mechanical frequency of the motor operating at 150 and 350 rpm are 2.5 Hz and 5.83 Hz, respectively. In Fig. 7-17(a) and (b), the frequency and temporal order of each SPL peak are shown. Comparing with Table 7-3, the radial force harmonics on the rotor with circumferential order, zero, are the primary cause of the acoustic noise in this ER SRM prototype. The acoustic noise results of this external-rotor SRM experimentally validate the pattern of the radial force harmonics for external-rotor SRM rotors, as shown in (7.6).

7.6 Conclusions

This chapter presents a comprehensive study in the radial force density harmonics in the internal-rotor SRM stators and the external-rotor SRM rotors. The pattern of the radial force density is analyzed and presented in an analytical equation to quickly obtain the temporal and circumferential orders of the radial force harmonics in external-rotor and internal-rotor SRMs. This pattern of the radial force density is applicable to IR SRM stators and ER SRM rotors with the phase excitation sequence in the CCW or CW direction and the radial force density is applied on the poles sequentially. The tested acoustic noise in a four-phase 8/6 IR SRM and a three-phase 12/16 ER SRM are used to validate the pattern for the radial force density harmonics proposed in the chapter.

References

[1] B. Bilgin and A. Emadi, “Electric motors in electrified transportation: A step toward achieving a sustainable and highly efficient transportation system,” *IEEE Power Electron. Mag.*, vol. 1, no. 2, pp. 10–17, Jun. 2014.

[2] B. Bilgin and A. Emadi, “Electric motor industry and switched reluctance machines," *Switched Reluctance Motor Drives: Fundamentals to Applications*, Boca Raton, FL, USA: CRC Press, ISBN: 9781138304598,

Nov. 2018.

[3] E. Bostanci, M. Moallem, A. Parsapour, and B. Fahimi, “Opportunities and challenges of switched reluctance motor drives for electric propulsion: a comparative study,” *IEEE Trans. Transport. Electrifc.*, vol. 3, no. 1, pp. 58-75, Mar. 2017.

[4] K. Kasper, “Analysis and control of the acoustic behavior of switched reluctance drives,” Ph.D. dissertation, RWTH Aachen Univ., Aachen, Germany, 2011.

[5] J. O. Fiedler, K. A. Kasper, and R. W. De Doncker, “Calculation of the acoustic noise spectrum of SRM using modal superposition,” *IEEE Trans. Ind. Electron.*, vol. 57, no. 9, pp. 2939-2945, Sept. 2010.

[6] F. L. M. dos Santos, J. Anthonis, F. Naclerio, J. J. C. Gyselinck, H. Van der Auweraer, and L. C. S. Góes, “Multiphysics NVH modeling: simulation of a switched reluctance motor for an electric vehicle,” *IEEE Trans. Ind. Electron.*, vol. 61, no. 1, pp. 469-476, Jan. 2014.

[7] M. Bösing, “Acoustic modeling of electrical drives*”,* Ph.D. dissertation, RWTH Aachen Univ., Aachen, Germany, Dec. 2013.

[8] C. Lin and B. Fahimi, “Prediction of acoustic noise in switched reluctance motor drives, ” *IEEE Trans. Energy Convers.*, vol. 29, no. 1, pp. 250–258, Mar. 2014

[9] C. Gan, J. Wu, and Y. Hu, “A review on machine topologies and control techniques for low-noise switched reluctance motors in electric vehicle

applications," *IEEE Access*, vol. 6, pp. 31430-31443, 2018.

[10] I. Jang, S. Ham, W. Kim, C. Jin, S. Cho, K. Lee, and J. Lee, "Method for analyzing vibrations due to electromagnetic force in electric motors," *IEEE Trans. Magn.*, vol. 50, no. 2, pp. 297-300, Mar. 2014.

[11] F. Lin, S. Zuo, and S. Wu, "Modeling and analysis of acoustic noise in external rotor in-wheel motor considering doppler effect," *IEEE Trans. Ind. Electron.*, vol. 65, no. 6, pp. 4524-4533, Jun. 2018.

[12] J. Dong, J. W. Jiang, B. Howey, H. Li, B. Bilgin, A. Dorneles Callegaro, and A. Emadi, "Hybrid acoustic noise analysis approach of conventional and mutually coupled switched reluctance motors," *IEEE Trans. Energy Convers.*, vol. 32, no. 3, pp. 1042-1051, Sept. 2017.

[13] E. Bostanci, M. Moallem, A. Parsapour, and B. Fahimi, "Opportunities and challenges of switched reluctance motor drives for electric propulsion: a comparative study," *IEEE Trans. Transport. Electrifc.*, vol. 3, no. 1, pp. 58-75, Mar. 2017.

[14] B. Bilgin, "Derivation of pole configuration in Switched reluctance machines," *Switched Reluctance Motor Drives*, Boca Raton, FL, USA: CRC Press, Nov. 2018.

[15] J. W. Jiang, J. Liang, J. Dong, B. Howey, and A. Callegaro, "Noise and vibration in switched reluctance machines," *Switched reluctance Motor Drives*, Boca Raton, FL, USA: CRC Press, Nov. 2018.

[16] S. M. Castano, R. Yang, C. Mak, B. Bilgin, and A. Emadi, "External-rotor

switched reluctance motor for direct-drive home appliances," in *44th Annual Conference of the IEEE Industrial Electronics Society*, Washington, DC, 2018, pp. 514-521.

[17] A. Callegaro, B. Bilgin, and A. Emadi, "Radial force shaping for acoustic noise reduction in switched reluctance machines," *IEEE Transactions on Power Electronics*, vol. 34, no. 10, pp. 9866-9878, Oct. 2019.

[18] B. Howey, "Non-coupled and mutually coupled switched reluctance machines for an E-bike traction application: pole configurations, design, and comparison," Ph.D. dissertation, McMaster Univ., Hamilton, ON, Canada, Aug. 2018.

[19] L. Vandevelde, J. J. Gyselinck, F. Bokose, and J. A. Melkebeek, "Vibrations of magnetic origin of switched reluctance motors," *COMPEL— Int. J. Comput. Math. Elect. Electron. Eng.*, vol. 22, no. 4, pp. 1009– 1020, Dec. 2003.

Chapter 8: Enhanced Modeling Techniques for Fast Numerical Simulation of Acoustic Noise in Switched Reluctance Machines

8.1 Introduction

A fast and accurate numerical modeling approach for the simulation of acoustic noise is always preferred when designing switched reluctance machines [1]-[2]. Although the conventional numerical method can provide more accurate results compared with the analytical method [3]-[5], it requires higher computation cost, due to several factors. First of all, even though many vibration modes have small effects on the vibration and acoustic noise, they are still considered in the conventional numerical approach. Secondly, the acoustic noise at all the frequency points is simulated numerically. Thirdly, the meshing of the near field is not frequency-dependent. Hence, the meshed near filed is often too thick and the element size is oversized to ensure the simulation accuracy. These factors make the numerical method time-consuming without improving simulation accuracy. The computation cost can be reduced significantly if only the excitation of the dominant vibration modes caused by the dominant radial force density harmonics at the dominant frequency points is simulated and the meshing of the near field is adaptive to the frequency that is being analyzed.

In the previous chapters, the vibration and acoustic noise behavior (Chapter 2 to Chapter 5) in the internal-rotor and external-rotor SRMs, the characteristics of the axial vibration modes (Chapter 6), and the harmonics of the radial force density (Chapter 7) have been studied comprehensively. The analyses and main contributions in the previous chapters will be combined here to present an enhanced numerical modeling approach, which can quickly simulate the acoustic noise without sacrificing the accuracy. The method proposed in this chapter can be applied to internal-rotor and external-rotor SRMs, where the phase excitation sequence is in either the counter clockwise or clockwise direction, and the radial force density is applied on the poles sequentially without skipping any poles.

8.2 Simulation of Acoustic Noise in Time domain and Frequency Domain

The acoustic noise simulation by using the numerical method can be conducted in the time domain or in the frequency domain. However, the time-domain acoustic noise simulation often requires higher computation cost and, thus, longer simulation time. There are several reasons for the higher computation cost in the time-domain analysis. In the time-domain simulation, the time-varying sound pressure needs to be simulated and then decomposed using 1D FFT to obtain the sound pressure level (SPL) as a function of the frequency. However, only the stabilized sound pressure can be used to obtain the SPL. Fig. 8-1 shows an example of the sound pressure obtained by a time-domain acoustic noise simulation. It can be observed that it has unstable regions and it takes time for sound pressure to reach the stabilized regions, which can be used for FFT analysis. Unlike the time-domain simulation, SPL at a certain frequency can be obtained directly in the frequency-domain simulation.

Another factor that causes higher computation cost in the time-domain acoustic simulation is the inefficient meshing of the near field. The thickness and the element size in the meshing of the near field is often determined by the lowest frequency and the highest frequency of the radial force density harmonics, respectively. This means that a thick meshing of the near field with small meshing elements is required in the time-domain simulation. This chapter aims to propose a fast numerical modeling approach for the numerical simulation of the acoustic noise in the frequency domain.

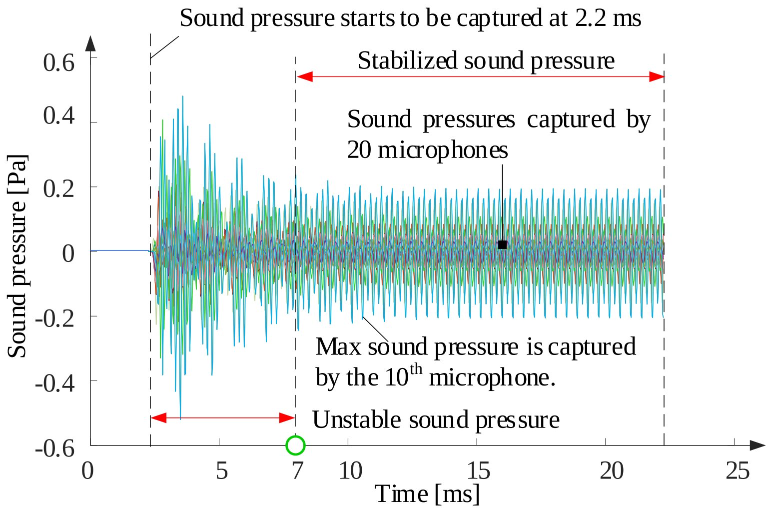

Fig. 8-1. Sound pressure obtained by the time-domain numerical simulation of acoustic noise [6].

8.3 Enhanced Numerical Modeling Techniques

8.3.1 Block Diagram of the Enhanced Numerical Approach

In an SRM design process, after the pole configuration is confirmed and the design is completed, the enhanced numerical modeling approach shown in Fig. 8-2, can be used to quickly simulate the acoustic noise without sacrificing the accuracy. The enhanced numerical modeling approach is based on the analyses in the previous chapters. A brief introduction of this enhanced numerical approach will be presented in this section.

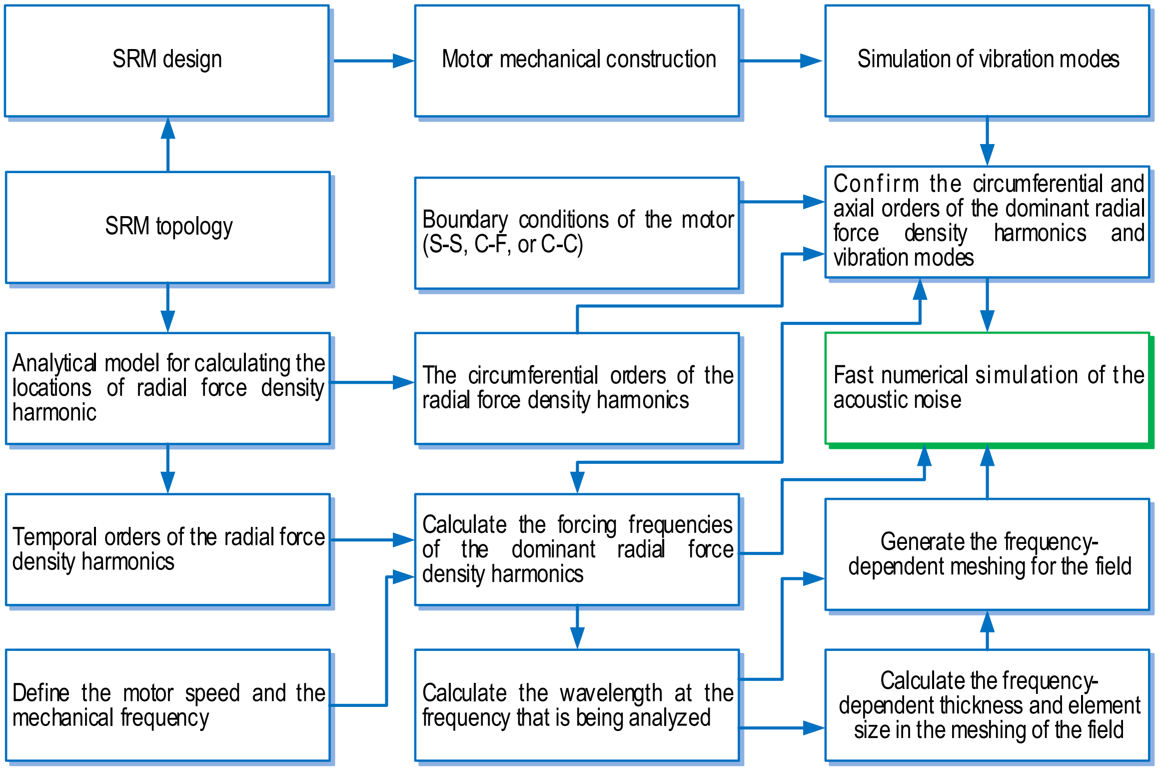

Fig. 8-2. Block diagram of the enhanced numerical modeling approach.

The analytical model presented in Chapter 7 can be used to quickly calculate the circumferential and temporal orders of the radial force density harmonics. The forcing frequencies of the radial force density harmonics are calculated by using their temporal orders and the motor mechanical frequency. Meanwhile, the numerical modal simulation can be conducted to quickly obtain the vibration modes of the motor structure. The temporal, circumferential, and axial orders of the dominant radial force density harmonics, as well as the circumferential and axial orders of the dominant vibration modes can be determined using the boundary conditions of the motor, the temporal and circumferential orders of the radial force density harmonics, and the natural frequencies of the vibration modes. Since the dominant harmonics in the SPL waveform are caused by the dominant radial force density harmonics, and thus the dominant frequency points that need to be analyzed in the acoustic noise simulation, are the same as the forcing frequencies of the dominant radial force density harmonics. The thickness and the element size in the meshing of the near field need to be adjusted based on the dominant frequency points that need to be analyzed in order to reduce the computation cost. In this chapter, an 8/6 internal-rotor SRM will be used to explain how these enhanced numerical modeling techniques can be applied to simulate the acoustic noise quickly without sacrificing the accuracy.

8.3.2 Temporal, Circumferential Orders, and Frequencies of the Radial Force Density Harmonics

In Chapter 7, the temporal order, *u*, and the circumferential order, *v* of the radial force density harmonics for external-rotor and internal-rotor SRMs have been summarized in the following analytical model:

$$\begin{cases} u = N_{ph} \times N_r \times j + \alpha \times \beta \times N \times k \\ v = \dfrac{N_s}{N_{ph}} \times k \end{cases} \tag{8.1}$$

where $N_{ph} \times N_r$ is the number of strokes in one mechanical revolution, the coefficients, *α, β* and *N*, depend on the pole configuration and the rotational direction of the rotor:

$$\begin{aligned} &\begin{cases} \alpha = 1, \text{ if the rotor rotates at CCW} \\ \alpha = -1, \text{ if the rotor rotates at CW} \end{cases} \\ &\begin{cases} \beta = 1, \text{ if } N_s \ > \ N_r \\ \beta = -1, \text{ if } N_r \ > \ N_s \end{cases} \\ &\begin{cases} N = N_r \text{ for IR stator} \\ N = N_s \text{ for ER rotor} \end{cases} \end{aligned} \tag{8.2}$$

It should be noted that (8.1) and (8.2) are not applicable to all the SRM topologies. As discussed in Chapter 7, these equations can be used for SRMs where the phases are excited individually in CCW or CW direction, and the radial force density is applied on the poles sequentially without skipping any poles. For other SRMs, applying 2D FFT on the radial force density would still be necessary to obtain the temporal and circumferential orders of the radial force density harmonics.

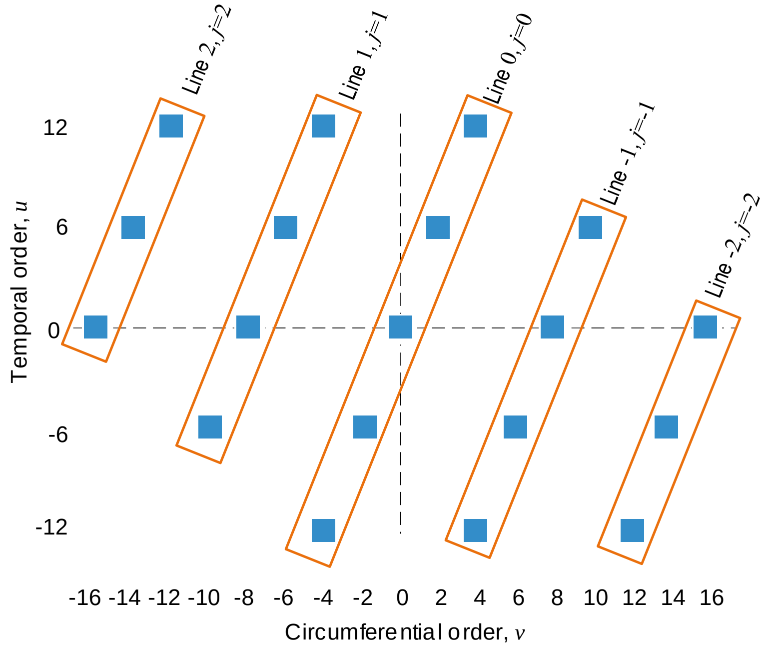

Fig. 8-3. Temporal and circumferential orders of the radial force density harmonics for the stator of an 8/6 internal-rotor SRM when the rotor rotates in the CCW direction.

Table 8-4 Temporal and circumferential orders, ($\lvert u\rvert$, $\lvert v\rvert$) of the radial force density harmonics of 8/6 IR SRM stator and the rotor rotates in the CCW direction.

($\lvert u\rvert$, $\lvert v\rvert$)		
Part	**Temporal order, $\lvert u\rvert$**	**circumferential order, $\lvert v\rvert$**
8/6 stator	24, 48, 72, 96, 120, 144, 168, …, $\lvert 24 \times j\rvert$	0
	6, 18, 30, 42, 54, 66, 78, 90, 102, 114, 126, 138, 150, 162, 174, 186, 198, 210, 222, 234, 246, 258, 270, 282…, $\lvert 24 \times j + 6\rvert$	2
	12, 36, 60, 84, 108, 132, 156, 182, 204, 228, …, $\lvert 24 \times j + 12\rvert$	4
	6, 18, 30, 42, 54, 66, 78, 90, 102, 114, 126, …, $\lvert 24 \times j + 18\rvert$	6

*: j can be any integer.

Fig. 8-3 shows the radial force density harmonics of the 8/6 SRM, where the temporal and circumferential orders are calculated by using (8.1) and (8.2). Table 8-4 and Table 8-5 show the circumferential orders, temporal orders, and the forcing frequencies of radial force density harmonics when the rotor rotates at 2048 rpm in the CCW direction. The circumferential and temporal orders of the dominant radial force density harmonics will be determined and confirmed in the next section when comparing the natural frequencies of the vibration modes with the forcing frequencies of the radial force density harmonics.

Table 8-5 Forcing frequencies of the radial force density harmonics of 8/6 IR SRM stator when the motor operates at 2048 rpm.

(f, $\|v\|$)		
Part	**Frequency, f [Hz]**	**circumferential order, $\|v\|$**
8/6 stator	819, 1638, 2457, 3276, 4096, 4915, 5734, 6553, 7372, 8192, …	0
	205, 614, 1024, 1434, 1843, 2253, 2662, 3072, 3482, 3892, 4301, 4710, 5120, 5530, 5939, 6349, 6758, 7168, 7578, 7987, 8806, 9216, 9625, …	2
	410, 1229, 2048, 2867, 3868, 4505, 5324, 6144, 6963, 7782, 8601, 9420, …	4
	205, 614, 1024, 1434, 1843, 2253, 2662, 3072, 3482, 3892, 4301, 4710, 5120, 5530, 5939, 6349, 6758, 7168, 7578, 7987, 8806, 9216, 9625, …	6

8.3.3 Dominant Vibration Modes

In order to accelerate the acoustic noise simulation, only the excitation of the dominant vibration modes needs to be considered in the enhanced numerical approach. The other vibration modes, which have minor effects on the acoustic noise, are not necessary to be included in the numerical simulation. The dominant circumferential and axial orders need to be determined to confirm the dominant vibration modes. When the circumferential order of a vibration mode is one of the circumferential orders of the radial force density harmonics, and the natural frequency of this vibration mode is close to the forcing frequencies of the radial force density harmonics, this circumferential order is referred as dominant. For example, the circumferential orders in the radial force density harmonics of the 8/6 IR SRM stator are 0, 2, 4, 6, 8,…, as shown in Fig. 8-3. Comparing the natural frequencies of the vibration modes (see Fig. 8-4) with the forcing frequencies of the radial force density harmonics (Table 8-5), the circumferential order *circ* = 2 can be confirmed as the dominant circumferential order because the natural frequencies of vibration modes (2, 1) and (2, 2) can be excited by most of the second circumferential order of the radial force density harmonics. For example, the natural frequencies of vibrations modes (2, 1) and (2, 2) are 1,896 Hz and 2,412 Hz, respectively, and they are close to the forcing frequencies 1843 Hz, 2253 Hz, and 2662 Hz for $|v| = 2$ at 2048 rpm. Therefore, it will be a proper approximation to consider only the vibration modes with circumferential order, 2 in the enhanced numerical approach for this 8/6 SRM.

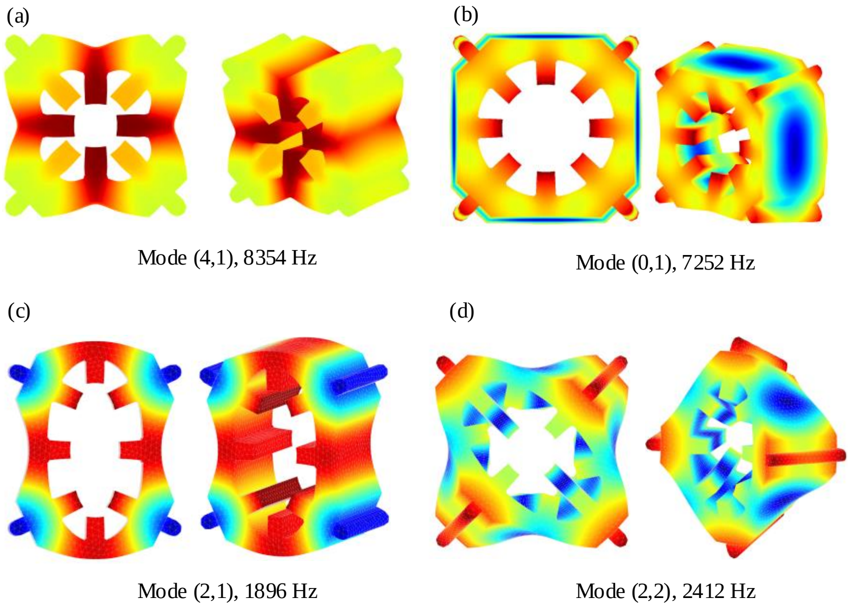

Fig. 8-4 Mode shapes and the natural frequencies in a 8/6 SRM, numerical simulation, (a) vibration mode (4, 1) at 8354 Hz, (b) vibration mode (0, 1) at 7252 Hz, (c) vibration mode (2, 1) at 1896 Hz, (d) vibration mode (2, 2) at 2412 Hz.

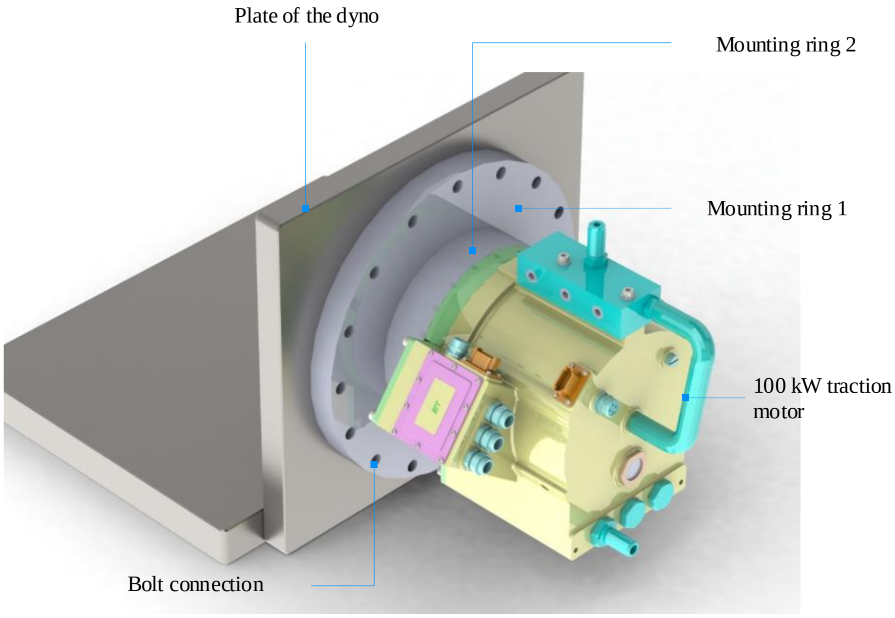

Fig. 8-5. The mounting of the traction motor on the dyno [6].

The axial orders of the vibration modes that are considered in the enhanced numerical approach also need to be confirmed. As discussed in Chapter 6, based on the boundary condition of the SRM, different axial orders of the vibration modes have different contributions to the acoustic noise. There are three common boundary conditions for SRMs, including supported-supported (S-S), clamped-clamped (C-C), and clamped-free (C-F). An example of the motor mounted on the dyno with C-F boundary condition is shown in Fig. 8-5. As discussed in Chapter 6, the axial modifying factor is introduced and obtained to describe the contribution of different axial orders of the vibration modes to the acoustic noise. The axial modifying factors for different boundary conditions of the motor from Chapter 6 are reminded in Fig. 8-6 and Table 8-6. It can be observed that the even axial orders of the vibration modes are not causing the acoustic noise when the motor is with S-S or C-C. Besides, when the axial order is larger than two, the natural frequencies of the vibration modes are often too high to be excited by the radial force density harmonics. Therefore, only the vibration modes with the first axial order are necessary to be considered in the enhanced numerical approach when the SRM is with S-S or C-C.

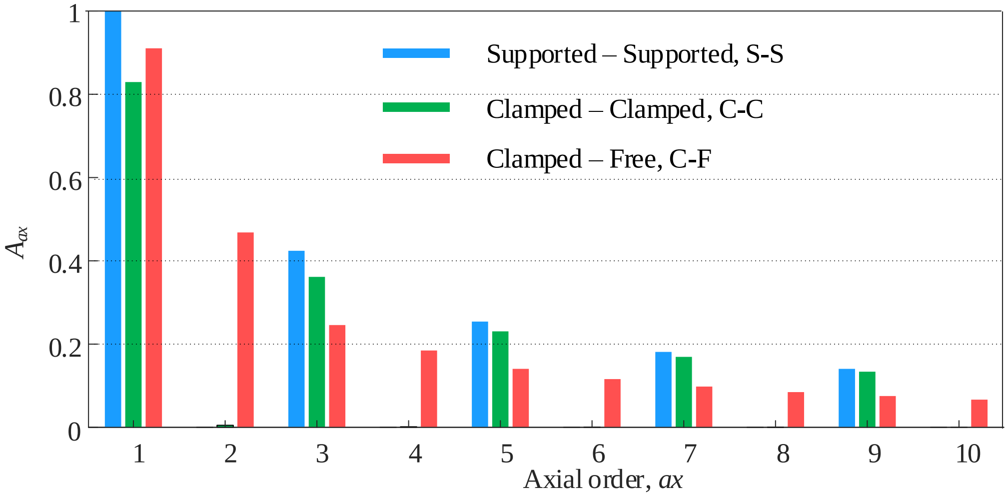

Fig. 8-6. Axial modifying factors for different boundary conditions, obtained from Chapter 6.

Table 8-6. Axial modifying factors for different boundary condition, obtained from Chapter 6.

		Axial order, *ax*								
		1	**2**	**3**	**4**	**5**	**6**	**7**	**8**	**9**
Boundary conditions	**S-S**	1	0	0.42	0	0.25	0	0.18	0	0.14
	C-C	0.83	0.01	0.36	0	0.23	0	0.17	0	0.13
	C-F	0.91	0.47	0.25	0.18	0.14	0.12	0.10	0.08	0.08

The axial modifying factors for the even axial orders of C-F are non-zero, which shows that the even numbers of the axial order of the vibration mode can cause acoustic noise. Therefore, the first and the second axial orders of the vibration modes are necessary to be considered in the acoustic noise simulation when the SRM is mounted with C-F.

8.3.4 Dominant Frequency Points to be Analyzed

Based on the analyses in the previous sections on the radial force density harmonics and the dominant circumferential orders of the vibration modes, the frequency points that need to be analyzed are the forcing frequencies of the dominant radial force density harmonics. For the 8/6 IR SRM, the dominant circumferential order of the vibration modes and the radial force density harmonics is confirmed to be two. Therefore, only the frequency points of the radial force density harmonics with the second circumferential order need to be analyzed in the enhanced numerical approach. These frequency points are shown in Table 8-7.

Table 8-7 Dominant frequency points to be analyzed in the acoustic noise simulation for the 8/6 IR SRM when the motor operates at 2048 rpm.

(f, $\|v\|$)		
Part	**Frequency, f [Hz]**	**circumferential order, $\|v\|$**
8/6 SRM stator	205, 614, 1024, 1434, 1843, 2253, 2662, 3072, 3482, 3892, 4301, 4710, 5120, 5530, 5939, 6349, 6758, 7168, 7578, 7987, 8806, 9216, 9625, …	2

8.3.5 Efficient Structural Meshing

In the structural meshing, the element size is related to the frequency of the vibration in the motor structure. The maximum allowable element size of the SRM structure can be calculated by [7]-[8]:

$$\varepsilon = \frac{1}{n} \times \lambda_B \tag{8.3}$$

where λ_B is the wavelength of the bending wave and n is the number of elements per wavelength in the meshed structure. The wavelength λ_B can be calculated as:

$$\lambda_B = \frac{c_B}{f} \tag{8.4}$$

where c_B is the speed of the bending sound wave, f is the maximum frequency in the acoustic noise simulation. The speed of bending wave, c_B, can be calculated by:

$$c_B = (1.8 \times c_L \times t \times f)^{0.5} \tag{8.5}$$

where c_L is the longitudinal sound wave, t is the thickness of the housing. The speed of the longitudinal wave, c_L, is calculated as:

$$c_L = \left\{ \frac{E}{\rho\left(1-\nu^2\right)} \right\}^{0.5} \tag{8.6}$$

where E, ρ and v are Young's modulus, density and Poisson's ratio of the motor material, respectively.

Fig. 8-7 shows an example of the maximum allowable element size in the meshed structure for the acoustic noise and vibration simulation when t = 55 mm, v = 0.3, ρ = 7600 Kg/m^3, E = 200 GPa, n = 10. It can be observed that the max allowable element size at 20 kHz is 16 mm. Therefore, the element size of the meshed structure for the NVH simulation can be relatively large.

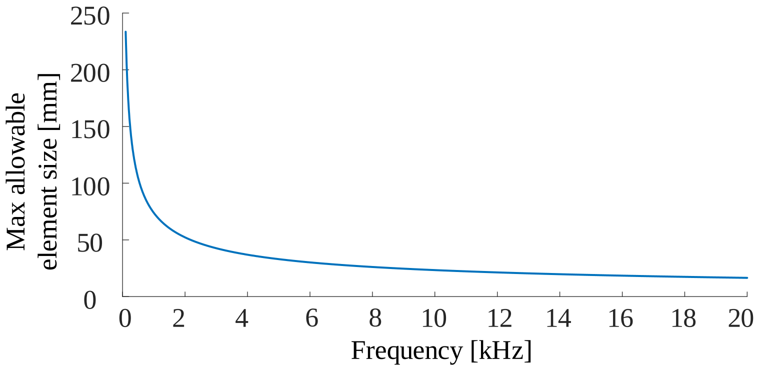

Fig. 8-7. Element size of the meshed structure.

8.3.6 Frequency-Dependent Meshing of the Acoustic Field

The thickness and the element size in the meshing of the near field affect the computation cost and the simulation accuracy. Fig. 8-8 shows the meshing of the motor structure and the near field. As a rule of thumb, a near field meshing thickness of one wavelength can provide an accurate simulation result with a small computation cost. The element size in the acoustic meshing can be calculated by:

$$\varepsilon = \frac{\lambda}{n} = \frac{c}{n \times f} \tag{8.7}$$

where c is the speed of the sound in air, λ is the wavelength, f is the frequency to be analyzed, and n is the number of elements per wavelength.

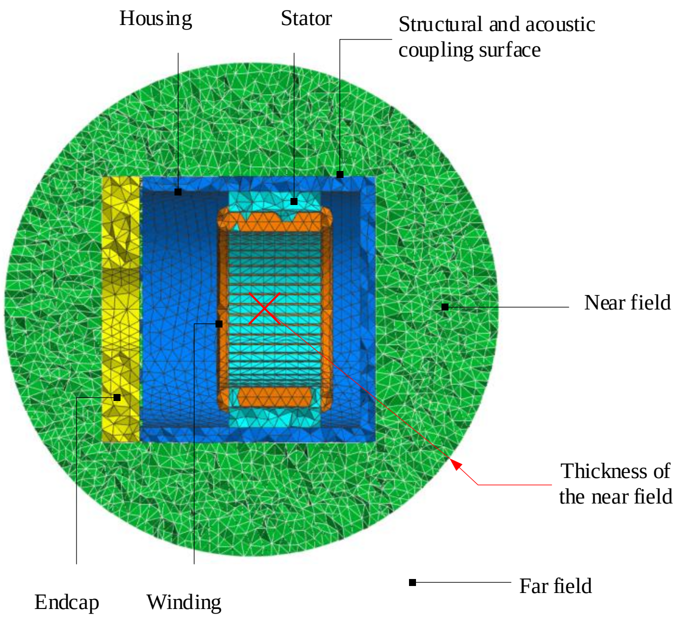

Fig. 8-8. The meshing of the motor structure and near field for the acoustic noise simulation in ACTRAN [1].

The selection of the number of elements per wavelength, *n*, is related to the Nyquist rate and the Nyquist sampling criterion. The acoustic noise radiated from the vibrating motor structure at a certain frequency can be regarded as a sinusoidal wave traveling in the near field [4]. During the numerical simulation of the acoustic noise, this sinusoidal wave needs to be approximated and simulated in the meshed near field. Based on the Nyquist sampling criterion, the sampling frequency needs to be twice the frequency of the sinusoidal wave so that it can be approximated and sampled without introducing significant errors. Fig. 8-9 will be used to illustrate how the selection of *n* can affect the accuracy in the approximation of the sinusoidal wave.

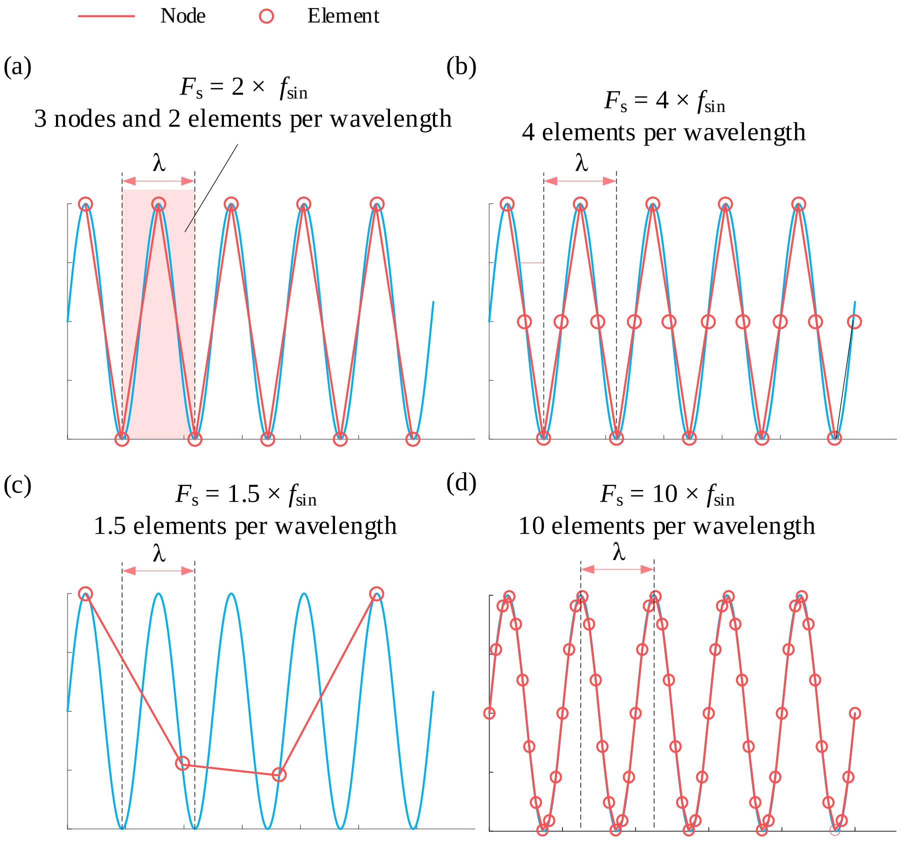

Fig. 8-9. Approximating a sinusoidal wave by different number of elements per wavelength, (a) $f_s = 2 \times f_{sin}$, 2 elements per wavelength, (b) $f_s = 4 \times f_{sin}$, 4 elements per wavelength, (c) $f_s = 1.5 \times f_{sin}$,1.5 elements per wavelength, (d) $f_s = 10 \times f_{sin}$, 10 elements per wavelength

In Fig. 8-9, the sampling frequency, F_s, is twice the frequency of the sinusoidal wave, f_{sin}. If the nodes in Fig. 8-9(a) represents the nodes in the meshing of the near field, then three nodes and two elements per wavelength are used to approximate the sinusoidal wave. Similarly, in Fig. 8-9(b), the sampling frequency is four times as much as f_{sin}, and five nodes and 4 elements per wavelength are used for the approximation of the sinusoidal wave. In these two cases, it can be observed that the shape and the magnitude of the sinusoidal wave can be approximated by the nodes and the meshed elements with minor errors. However, in Fig. 8-9(c), the sampling frequency is only 1.5 times as much as the frequency of the sinusoidal wave, and only 1.5 elements per wavelength are used for the approximation. The magnitude of the sinusoidal wave cannot be approximated in this case. Therefore, in order to approximate the acoustic noise waveform by using the meshing of the near field without introducing significant errors, the number of elements per wavelength in the meshed near field should be at least 2. For improved accuracy, *n* can be more than 10, which is illustrated in Fig. 8-9(d). As a conclusion, the thickness and the element size of the meshed near filed need to be adjusted based on the frequency that is being analyzed in order to reduce the computation cost and improve the simulation accuracy.

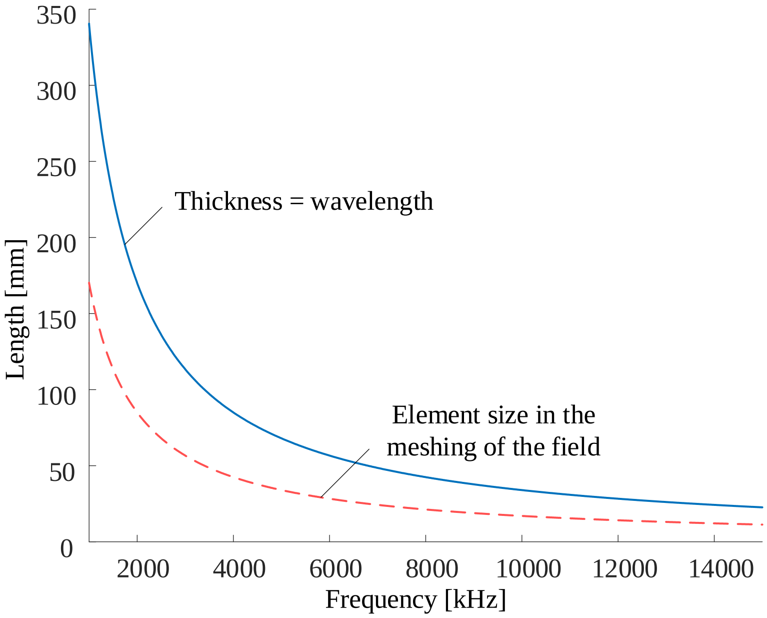

Fig. 8-10. Frequency-dependent wavelength of the acoustic noise, and thickness and element size in the meshing of the near field, $n = 10$.

Fig. 8-10 shows how the thickness of the near field and the element size in the meshing of the near field change with the frequency [9]. It should be noted that the red line in Fig. 8-10 is different from the line shown in Fig. 8-7, where the relationship between the element size of the structural meshing and the frequency is presented. It can be observed that thicker near field with coarse meshing is required in the low-frequency region to ensure the simulation accuracy at low frequencies. In the high-frequency region, thin near field with fine meshing is required. Fig. 8-11 compares the meshings of the motor structure and the near filed of the 8/6 SRM at 1024 Hz and 9625 Hz. It should be noted that the meshing of the motor structure is unchanged while the meshing of the near filed is updated for the frequency that is being analyzed.

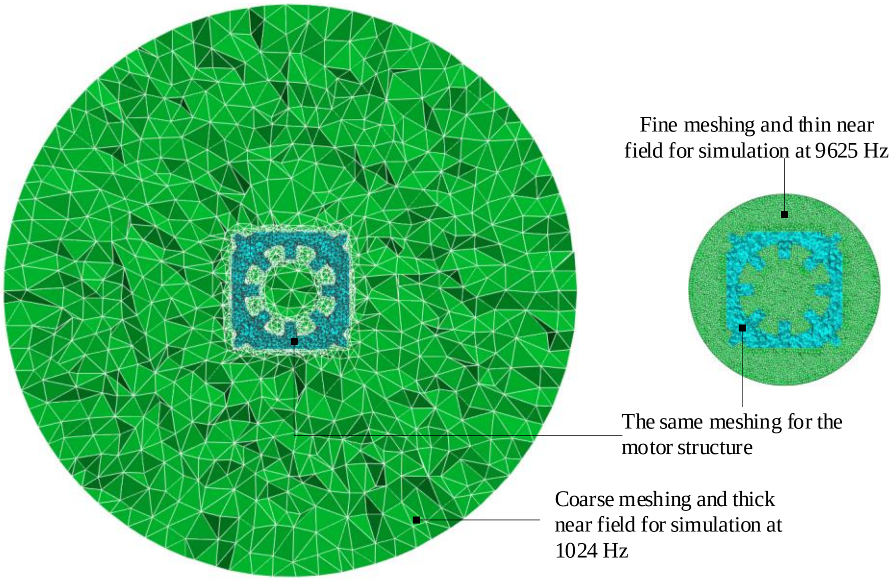

Fig. 8-11. Frequency-dependent thickness and element size in the meshing of the near field for the acoustic noise modeling of the 8/6 SRM in ACTRAN.

8.4. Results and Discussions

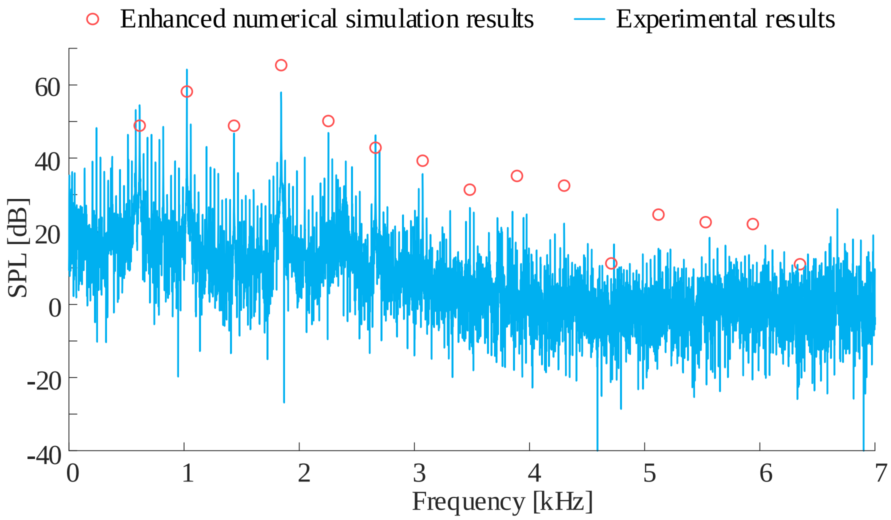

Fig. 8-12. Comparison of the experimental results and the results of the enhanced numerical simulation, 8/6 SRM at 2048 rpm, 5 Nm.

By using the enhanced numerical modeling approach, the SPL of an 8/6 SRM at 2048 rpm and 5 Nm is presented in Fig. 8-12. The acoustic noise simulation is conducted in ACTRAN and takes 17 minutes to finish the simulation of the SPL at 16 dominant frequency points. The numerical acoustic noise simulation is conducted on the PC with i7-7600 CPU and 32 GB RAM. In comparison, it takes 8 hours and 12 minutes to finish the time-domain simulation. The details of the time-domain simulation results have been presented in Chapter 6. Therefore, the enhanced numerical modeling approach presented in this chapter has advantages in the computation cost and simulation speed compared with the conventional numerical modeling approach. It is also shown in Fig. 8-12 that there is a good match between the experimental results and the SPL simulated by the enhanced numerical method.

8.5 Conclusions

Several enhanced modeling techniques are presented in this chapter to reduce the computation cost in the acoustic noise simulation for SRMs without sacrificing accuracy. After the analytical calculation of the temporal and circumferential orders of the radial force density harmonics, and the numerical simulation of the vibration modes, the dominant temporal, circumferential, and axial orders of the radial force density harmonics, and the dominant vibration modes can be confirmed. The dominant temporal orders of the radial force density harmonics and the motor speed can be used to calculate the dominant frequency points that need to be analyzed in the numerical acoustic noise simulation. Based on the analyses, the meshing of the motor structure can be coarse and does not need to be changed with the frequency. However, the thickness and the element size in the meshing of the near field need to be adjusted based on the frequency that is being analyzed. The SPL of an 8/6 internal-rotor SRM at 2048 rpm and 5 Nm is used to validate the accuracy and the computation cost of the proposed method, which can also be helpful to quickly simulate the acoustic noise numerically in other SRMs.

References

[1] X. Guo, R. Zhong, M. Zhang, D. Ding, and W. Sun, “Fast computation of radial vibration in switched reluctance motors,” *IEEE Transactions on Industrial Electronics*, vol. 65, no. 6, pp. 4588-4598, June 2018.

[2] C. Lin and B. Fahimi, “Prediction of acoustic noise in switched reluctance motor drives,” *IEEE Transactions on Energy Conversion*, vol. 29, no. 1, pp. 250-258, March 2014.

[3] J. Dong, J. Jiang, B. Howey, H. Li, B. Bilgin, A. Callegaro, A. Emadi., “Hybrid acoustic noise analysis approach of conventional and mutually coupled switched reluctance motors,” *IEEE Transactions on Energy Conversion*, vol. 32, no. 3, pp. 1042–1051, Feb. 2017.

[4] F. Santos, J. Anthonis, F. Naclerio, J. Gyselinck, H. Auweraer, and L. Goes, “Multiphysics NVH modeling: simulation of a switched reluctance motor for an electric vehicle,” *IEEE Transactions on Industrial Electronics*, vol. 61, no. 1, pp. 469–476, Jan. 2014.

[5] M. Bösing, Acoustic Modelling of Electrical Drives, Ph.D. Dissertation, RWTH Aachen University, Dec.2013.

[6] J. Liang, Y. Li, C. Mak, J. Jiang, B. Bilgin, D. Al-Ani, and A. Emadi, “A comprehensive analysis of the acoustic noise in an interior permanent magnet traction motor,” *in Proc. IEEE Energy Conversion Congress and Exposition (ECCE),* Sept. 2019, pp. 1-7, accepted and to be published.

[7] J. Liang, J. W. Jiang, A. Dorneles Callegaro, B. Bilgin, J. Dong, D. Reeves, and A. Emadi, “Prediction of noise and vibration of a 24/16 traction SRM”, *IET Electrical Systems in Transportation*, accepted and to be published.

[8] J. W. Jiang, J. Liang, J. Dong, B. Howey, and A. Callegaro, “Chapter 13: Noise and vibration in switched reluctance machines,” *Switched Reluctance Motor Drives: Fundamentals to Applications*, Boca Raton, FL, USA: CRC Press, ISBN: 9781138304598, Nov. 2018.

[9] T. Rossing, *Handbook of Acoustics,* New York, NY, USA: Springer, ISBN: 9781493907557, 2014.

Chapter 9: Conclusions and Future Work

9.1 Conclusions

Compared with the other electric machines, the acoustic noise in SRMs can be more significant. This is due to the numerous harmonic components in its electromagnetic force density, which depend on the topology, the design, and the control of the SRM. However, not all electromagnetic force density harmonics cause vibration and acoustic noise in SRMs. A numerical modeling approach presented in Chapter 4 can be used to simulate the acoustic noise, and analyze the dominant vibration modes as well as the dominant radial force density harmonics in internal-rotor SRMs. For external-rotor SRMs, the acoustic noise can be caused by the radial vibration of the rotor back iron and the tangential vibration of the stator poles. This is because the rotor back iron in ER SRMs is often designed with a small thickness to reduce the inertia, and the stator can sometimes be designed with a long pole height to improve the average torque. Methodologies for analyzing the rotor radial force density harmonics and stator tangential force density harmonics, and the characteristics of the vibration and acoustic noise in external-rotor SRMs are presented in Chapter 5. It is also concluded in Chapter 5 that the acoustic noise caused by the rotor radial vibration still dominates in the total acoustic noise in a 12/16 external-rotor SRM designed for a direct-drive e-bike application.

In Chapter 4, the relationship between the circumferential orders of the vibration modes and the radial force density harmonics in internal-rotor SRMs, has been studied. Besides, the effect of the high-axial-order vibration modes on the acoustic noise of IR SRMs is presented in Chapter 6. A novel analytical method is introduced which can simulate the acoustic noise in the three-dimensional (3D) domain. Results show that the effect of the axial orders of the vibration modes on the acoustic noise depends on the boundary conditions of the SRM.

The patterns of the radial force density harmonics in IR SRM stators and ER SRM rotors are studied in Chapter 7 and summarized in an analytical expression, which can be used to quickly calculate the temporal and circumferential orders of SRMs without running electromagnetic FEA simulations. This analytical expression is applicable only to internal-rotor and external-rotor SRMs, where the phase excitation sequence is in either the counter clockwise or clockwise direction, and the radial force density is applied on the poles sequentially without skipping any poles. Based on the analyses in the previous chapters, an enhanced numerical modeling approach is presented in Chapter 8 to quickly simulate the acoustic noise in SRMs without sacrificing the accuracy.

The modeling, analyses and the simulation results presented in this thesis are experimentally validated by the hammer test results of a 60 kW three-phase 24/16 internal-rotor traction SRM, the acoustic noise test results of a three-phase 12/16 external-rotor SRM, and the hammer test and acoustic noise test results of a four-phase 8/6 internal-rotor SRM.

9.2 Future Work Suggested

The following research topics can be further investigated and studied:

(1) Future study can be conducted to study the pattern of radial force density harmonics for the other SRM topologies with different phase excitation and radial force density characteristics. The analytical expressions for calculating the circumferential and temporal orders can be enhanced and developed to cover more SRM topologies.

(2) The enhanced numerical method for the fast simulation of acoustic noise can be incorporated in the geometric optimization of SRMs and the acoustic noise reduction by using circumferential slits.

(3) The sampling effect of the radial force density harmonics with high circumferential orders on the vibration and acoustic noise in SRMs needs to be further studied.

(4) The effect of manufacturing tolerances on the magnitudes of the radial force density harmonics and the acoustic noise needs to be studied.

9.3 Publications

During my Ph.D. study, I contributed to the following publications:

Published Book Chapters:

[1] Y. Yang, J. Jiang, and **J. Liang**, “Chapter 8: Mechanical construction of switched reluctance machines”, *Switched Reluctance Motor Drives: Fundamentals to Applications*, Boca Raton, FL, USA: CRC Press, ISBN: 9781138304598, Nov. 2018.

[2] J. Jiang and **J. Liang**, “Chapter 12: Fundamentals of waves and vibrations”, *Switched Reluctance Motor Drives: Fundamentals to Applications*, Boca Raton, FL, USA: CRC Press, ISBN: 9781138304598, Nov. 2018.

[3] J. Jiang, **J. Liang**, J. Dong, B. Howey, and A. D. Callegaro, “Chapter 13: Noise and vibration in switched reluctance machines”, *Switched Reluctance Motor Drives: Fundamentals to Applications*, Boca Raton, FL, USA: CRC Press, ISBN: 9781138304598, Nov. 2018.

[4] Y. Yang, **J. Liang**, J. Jiang, and E. Rowan, “Chapter 14: Thermal management of switched reluctance machines”, *Switched Reluctance Motor Drives: Fundamentals to Applications*, Boca Raton, FL, USA: CRC Press, ISBN: 9781138304598, Nov. 2018.

Accepted / Published Journal Papers:

[1] **J. Liang**, J. W. Jiang, B. Bilgin, and A. Emadi, “Shaft design for electric traction motors,” *IEEE Transactions on Transportation Electrification*, vol. 4, no. 3., pp. 720-731, Sept. 2018.

[2] **J. Liang**, J. W. Jiang, B. Bilgin, A. D. Callegaro, J. Dong, D. Reeves, and A. Emadi, “Prediction of noise and vibration of a 24/16 traction SRM”, *IET Electrical Systems in Transportation*, Early Access.

[3] A. D. Callegaro, **J. Liang**, J. Jiang, B. Bilgin, and A. Emadi, “Radial force density analysis of switched reluctance machines: the source of acoustic noise,” *IEEE Transactions on Transportation Electrification*, vol. 5, no. 1, pp. 93-106, March 2019.

[4] B. Bilgin, **J. Liang**, M. Terzic, J. Dong, E. Trickett, R. Rodriguez, and A. Emadi, “Modeling and analysis of electric motors: state-of-the-art review,” *IEEE Transactions on Transportation Electrification*, vol. 5, no. 3, pp. 602-617, Sept. 2019.

Accepted/published Conference Papers:

[1] **J. Liang**, Y. Li, C. Mak, B. Bilgin, D. Al-Ani, and A. Emadi, “A comprehensive analysis of the acoustic noise in an interior permanent magnet traction motor”, in *Proc. IEEE Energy Conversion Congress and Exposition (ECCE),* Sept. 2019, pp. 1-7.

[2] **J. Liang**, J. W. Jiang, Y. Yang, D. Al-Ani, B. Bilgin, A. Sathyan, and A. Emadi, “Torque ripple reduction for interior permanent magnet synchronous machines under load excitation by optimizing rotor skew

angles," in *Proc. IEEE International Conference on Mechatronics Technology (ICMT 2019)*, Salerno, Italy, Oct. 2019. (The paper also won the Best Paper Award of ICMT 2019 conference)

[3] S. M. Castano, E. Sayed, J. W. Jiang, **J. Liang**, B. Bilgin, A. Sathyan, H. Dadkhah, M. H. Bakr, and A. Emadi, "Design of a spoke-type ferrite magnet generator for a hybrid electric vehicle application," in *Proc. IEEE Transportation Electrification Conference and Expo (ITEC 2019)*, Detroit, MI, USA, Jun. 2019, pp. 1-6.

Papers: submitted / to be submitted:

[1] **J. Liang**, B. Bilgin, B. Howey, and A. Emadi, "Enhanced acoustic noise modeling and analysis in external-rotor switched reluctance machines: source of acoustic noise," contents come from Chapter 5, to be submitted.

[2] **J. Liang**, A. D. Callegaro, B. Bilgin, and A. Emadi, "A novel three-dimensional analytical approach for acoustic noise modeling in switched reluctance machines," contents come from Chapter 6, submitted to *IEEE Transactions on Industrial Electronics*, Review in progress.

[3] **J. Liang**, A. D. Callegaro, B. Howey, B. Bilgin, J. Dong, J. W. Jiang, J. Lin, and A. Emadi, "Pattern of radial force density harmonics for external-rotor and internal-rotor switched reluctance machines," contents come from Chapter 7, submitted to *IEEE Transactions on Energy Conversion*, Review in progress.

[4] B. Bilgin, B. Howey, A. D. Callegaro, **J. Liang**, M. Kordic, J. Taylor, and A. Emadi, “Making the case for switched reluctance motors for propulsion applications,” to be resubmitted to *IEEE Transactions on Vehicular Technology*.

[5] E. Sayed, S. M. Castano, J. W. Jiang, **J. Liang**, B. Bilgin, A. Sathyan, H. Dadkhah, M. H. Bakr, and A. Emadi, “Comparative analysis between different ferrite magnet generator designs for a hybrid electric vehicle,” submitted to FCA US LLC for review and to be submitted to an IEEE journal.

[6] Y. Li, **J. Liang**, B. Howey, B. Bilgin, D. Al-Ani, and A. Emadi, “Dynamic modeling of an interior permanent magnet machine with space-vector-modulation-based voltage source inverter,” submitted to *SAE World Congress Experience (WCX) 2020*, Review in Progress.

[7] E. Sayed, R. Yang, **J. Liang**, M. H. Bakr, B. Bilgin, and A. Emadi, “Design of unskewed interior permanent magnet traction motor with asymmetric flux barriers and shifted magnets for Nissan leaf electric vehicle,” *Electric Power Components and Systems,* Second Review in Progress.

[8] N. Emery, S. Dasara, **J. Liang**, D. Al-Ani, A. Emadi, and B. Bilgin, “Study on the effect of dynamic eccentricity on the acoustic noise of an interior permanent magnet traction motor,” The digest has been submitted to *Proc. IEEE Transportation Electrification Conference and Expo.2020.*